INTERFACIAL RECOGNITION AND ADSORPTION PROCESSES

Thesis submitted for the degree of
Doctor of Philosophy
at the University of Leicester

by

Andrew John Walter BSc (Leicester)
Department of Chemistry
University of Leicester

November 2005

ProQuest LLC
789 East Eisenhower Parkway
P.O. Box 1346
Ann Arbor, MI 48106-1346

I would like to extend my thanks to everyone who has supported me during my studies for my PhD. I would like to thank all members of the research groups that I have been lucky enough to study in, but in particular I would like to thank Professors Rob Hillman and Andy Abbott for their kind support and words of wisdom throughout my time here. My sincere thanks to you both gentlemen for everything.

To Kayt

Interfacial Recognition And Adsorption Processes

Abstract

The design and function of receptors for molecular recognition is of vital importance for the construction of novel sensors. Initially the project has investigated the relationship between the shape of the active site of the receptor and its sensitivity and selectivity for analytes in solution. The techniques of electrochemistry, NMR and molecular modelling have been used to study materials interactions. An optimum receptor design was established for a range of analytes so that the surface of an electrode could be modified to create an analytical sensor.

Subsequently, the project has involved the investigation of small molecule adsorption, recognition and permeation at polymer plant wax constituent layers that model leaf cuticles. Correlations have been sought between the responses to these surfactants/adjuvants and the wax compositions. At low levels of interaction, the quartz crystal microbalance was used as a gravimetric sensor of these processes. At higher levels of interaction, when permeation of the film is sufficient to plasticise it, the rheological effects were used to explore solvent/small molecule permeation. In each case, qualitative data was used to diagnose film rigidity *vs.* viscoelasticity and quantitative data to determine film mass (thickness) or shear moduli, as appropriate. The experimental measurements have been supported by a computer model derived from the processes occurring at the interface and the resultant changes in film viscoelastic properties are discussed.

Contents

Chapter 1
Introduction and Background

1.1 Introduction And Background

Analytical applications of sensor devices can be found in many areas, including environmental monitoring[1-5], metallurgy[6-7], geology[8-9], pharmacy[10-11], medicinal chemistry[12-13] and biochemistry[14-16], and include the quantitative determination of anions[17-18], cations[19-21], gases[22-24] and a wide range of inorganic[25-27] and organic[28-31] compounds, often in trace amounts. Devices employing electrochemical methods have the great advantage of being usable in high coloured or opaque solutions, and can often give simultaneous recordings of several different species in solution. In addition, the apparatus is often inexpensive, allowing extensive field measurements to take place; even where equipment is less portable, the number of steps necessary to treat the sample before measurements is usually smaller than for spectrochemical techniques.

The different types of sensor that is currently available for the detection of a particular species can be broken down into the following categories:

- Electrochemical transducers - *split further into potentiometric and amperometric devices. If analyte binding to a receptor causes a change in the thermodynamics of the receptor's redox process then a potentiometric response is observed, if the analyte precludes or enhances electron transfer however, then a change in amperometric signal is observed.*
- FET-based sensors - *essentially a potentiometric sensor that has been miniaturized onto a chip (a field effect transistor).*
- Optical transducers - *covers a variety of techniques from absorption spectroscopy, fluorescence spectroscopy, luminescence spectroscopy, internal reflection spectroscopy, surface plasmon resonance and light scattering.*
- Piezoelectric devices - *those that generate an inverse relationship i.e. an applied voltage is use to measure the frequency of vibration in a vibrating*

crystal. The frequency of vibration is affected by the mass of a material adhered to the surface of the crystal.

- Surface acoustic wave devices – *similar to a piezoelectric device except that an applied frequency causes mechanical stress in the crystal, picked up by a second set of electrodes and thus related to an electrode voltage.*

The range of analytes able to be studied using one or more of the various techniques is almost limitless. They range from simple inorganic ions and molecules to complex organic biomolecules. It would be difficult to give an accurate overview of all the different types of sensor in the literature as they number well into the thousands. For the purpose of this study an overview of amperometric, potentiometric and gravimetric sensors is given in sections 1.2-1.4 to highlight some of the examples around in the literature today. One example given particular attention as a host molecule for the detection of simple metal ions is the crown ether; this is discussed in a little more detail in section 1.3. Although not exhaustive it does convey to the reader some idea of the more recent important developments in this area.

1.2 Amperometric *vs.* Potentiometric Sensors

Potentiometric sensors have become more important in recent years. This is perhaps no great surprise as they are the largest and most widely documented area of sensor technology. They are currently enjoying a renaissance as past examples are reviewed, refined and reintroduced into current circles of thinking. It is an area that links fundamental host-guest chemistry and membrane science to the direct application it targets. The leading researchers for many years in this field include the likes of Thomas[32], Buck[33-34] and Janata[35] with their contributions varying greatly across the range of chosen analytes to study, and the host receptors to employ in recognition experiments.

Perhaps the most surprising and innovative research direction in potentiometric sensors continues to be the dramatic improvement in the detection limit. It has been shown by scanning electrochemical microscopy, that concentration polarizations occur near ion-selective membranes measured under zero-current

conditions[36]. In optimised membranes, such transmembrane ion fluxes are thought to originate primarily from counter diffusion processes. Some ions are displaced from the sample side of the membrane by interfering ions, which leads to small concentration gradients across the membrane[37]. These processes have been described theoretically for the steady-state case in a compact form and have been used to accurately predict experimental detection limits of lead[38] and cadmium-selective electrodes[39] down to 10 parts per trillion. Ceresa *et al*[38] have found that ion-selective electrodes (ISE's) can be used to assess lead concentrations in actual environmental samples at levels sufficiently below the action limit, with the results compared quantitatively with concentrations obtained from ICPMS data.

It has been shown that ISE's with low detection limits can also be fabricated for alkali metals by adding an ion-exchange resin to the inner solution of the membrane[40]. Ordinarily, low detection limit ISE's required a water-soluble chelator in the inner solution, that limit the types of ions for which the detection limit could be improved. Ion-selective membranes that showed apparent super-Nernstian response slopes because of strong ion fluxes in the direction of the inner solution were shown to be useful[41]. Low detection limits have also been reported to be drastically lowered in the case of chalcogenide glass membranes for the low measurement of iron (III) in seawater[42]. However, that paper was disputed[43], and it remains to be seen whether solid membrane materials will achieve the desired performance.

Ion-selective electrodes based on sol-gel membranes have been developed with encapsulated valinomycin or bis (crown ether) derivatives[44]. The size of these membranes could be increased by using solid-state filter materials as membrane support. The study also showed that the sol-gel could be chemically functionalised with alkyloxysilylated bis(crown ether) derivatives as covalently immobilized ionophores. Liquid crystalline materials have been evaluated for the fabrication of ion-selective membranes. A liquid crystal ionophore for ammonium ions showed superior potentiometric properties with a non-ionophoric liquid crystal material as plasticizer, suggesting that a liquid crystalline phase is retained at room temperature[45]. Such materials have promise because of the way liquid crystals can be manipulated and switched, as also suggested by a different study incorporating ionophores into liquid crystalline materials[46].

The development of ion-selective electrodes with a solid inner contact instead of an aqueous electrolyte has been a topic of research for many years. Historically,

so-called coated wire electrodes with a simple metal-membrane interface without any well-designed potential stability were known to exhibit potential drifts. A mechanism for this apparent instability has now been proposed to come from changes in the electrolyte composition of a water layer between the metal and the membrane[47]. Indeed, potential-time profiles were in good agreement with theoretical calculations, and the potentials became stable if a hydrophobic monolayer was deposited onto the metal, which suppressed the water film. In a different study, the carbon dioxide interference of solid contact electrodes was reexamined[48]. The CO_2 interference was found to be largest with pH-sensitive membranes backside contacted with a pH-insensitive metal (Ag or AgCl) or with pH-insensitive membranes backside contacted with a pH sensitive metal such as Pt. The most commonly used stable solid contact materials are conducting polymeric materials, such as poly(pyrrole)[49] or poly(thiophene)[50], that act as ion-to-electron transfer transducers. An interesting low frequency current reversal chronopotentiometric experiment revealed that such layered membranes could be adequately simulated with a RC equivalent circuit by using the resistance of the ion-selective membrane and the capacitance of the redox polymer[51]. This research could have important implications, as such polymers can be easily fabricated on metal electrodes by simple electropolymerization. Consequently, some authors have a profound interest in studying the ion- and electron-conducting characteristics of the redox polymer itself[52], since the resulting sensors may exhibit redox-sensing characteristics as well.

The electro-oxidation of D- and L- glucose was investigated using chiral platinum electrodes[53]. Both of the electrodes, $Pt\{643\}^R$ and its enantiomorph $Pt\{643\}^S$, were shown to be enantioselective. This behaviour was ascribed to the inherent (L or R) "handedness" of the kink sites present at the electrode surface since stepped surfaces, which are achiral, lack the prerequisite necessary for the observation of chirality and hence are unable to distinguish between enantiomers. Attard *et al*[54-55] have shown that chiral discrimination is an intrinsic property of kinked single-crystal surfaces. The adsorption of a chiral modifier onto the surface of an achiral substrate produces differences in the voltammetry only when the kinetics of the reaction are changed due to an enantiomeric response from one or both of the chiral analytes. By comparing and contrasting the cyclic voltammograms obtained, differentiation of the R and S enantiomers becomes readily discernable by eye.

Nitric oxide continues to enthral and excite electrochemists. A microelectrode for the *in-vivo* determination of NO was recently developed based on a modified Clark-type electrode design with a 10 μm tip diameter[56]. For ease of working, the reference electrode was placed coaxially around the working electrode tip, and a thin double membrane was used to eliminate interferences from ionic species. To improve selectivity and stability, a differential amperometry protocol was adopted. NO release rates of activated macrophages were subsequently determined. On the other hand the group of Meyerhoff showed that the NO releasing compounds embedded in the gas-permeable polymeric coatings of oxygen sensing catheters rendered the sensing much more thromboresistant[57]. While the sensor performance was shown to be unaltered by the presence of the NO releasing compound, a much superior analytical signal was demonstrated *in-vivo* followed by reduction of thrombus formation on the sensor surface. This rather elegant method of using the *in-vivo* characteristics of NO has the potential of finally solving the long-standing biocompatibility problem of *in-vivo* chemical sensing.

Staying with the idea of *in vivo* chemical sensing, the catalytic properties of iridium (IV) were studied and used to develop an improved insulin sensor based on glassy carbon electrodes plated with an iridium oxide surface film[58]. The catalytic activity was ascribed to a combination of electron and oxygen transfer within the film and detection limits were reported to be in the region of 20 nM in flow injection analyses. This is one example of how the selectivity of carbon paste electrodes can be chemically tuned by adding suitable biological or chemical catalysts to the paste material. Another example based on a similar design, involved the simultaneous detection of glucose and insulin[59].

Ferrocene-derivatized calix[4]-arene ligands were synthesized and characterised in view of lanthanide sensing[60]. The sensing principle relied on the anodic perturbation of the ferrocene-ferrocenium redox couple upon binding to the lanthanide metal ions. The studies remained fundamental; however, with no immobilization or actual sensor application reported. A similar principle was exploited by the introduction of redox active monolayers composed of calix[4]-arene-disulphide-diquinone units[61]. The calixarene was found to be highly selective for barium ions, with a 500 fold preference over calcium in separate solution experiments. The voltammetric behaviour of the modified electrode was found to be dependent on the barium concentration in the sample. The sensor is expected to be

sensitive to barium concentration changes only at low concentrations, where surface coverage of barium on the monolayer remains unsaturated.

Aromatic ureas were detected by modulation of the redox behaviour of phenanthrenequinone electropolymerised as a pyrrole derivative onto a metal electrode[62]. The selective detection of the urea compounds was explained by a strong hydrogen bond formation with the redox-dependent receptor. While significant loss of material was reported, the urea-dependent half-wave potential shift was found to be independent of electrode coverage. Polythiophene polymers incorporating cone and partial cone bridged calix [4] crown ethers were prepared on platinum electrodes and characterised for the sensing of alkali metals[63]. The films showed high sodium selectivity in acetonitrile solutions, demonstrating that the redox behaviour of the film could be altered by selective recognition of sodium ions by calixarene units. This particular fact is one that can be exploited, since it is well known that alkali metals do not undergo redox chemistry (*i.e.* $M^+ \not\rightleftarrows M^0$). In a related approach, metal (III) deuteroporphyrins with pyrrole groups were electropolymerised and found to electrocatalyze dioxygen and benzoic anhydrides[64]. Feasibility of using such systems as molecular recognition based sensors was demonstrated with cyanide ions that interacted with Fe(III) porphyrins and changed the redox behaviour of the film.

Anion sensing and recognition still remains a challenging task because of the limited availability of suitable molecular hosts for anions. An unusual mechanism for the indirect amperometric anion sensing with ITIES (interface of two immiscible electrolyte solutions) was reported by the use of a dual ionophore system[65]. The potassium-transfer wave for an organic phase containing both potassium and nitrate ionophores was found to increase with higher nitrate concentrations in the sample. While this phenomenon was explained with a lowered effective Gibb's energy of transfer for potassium by nitrate, it seems likely that spontaneous (zero current) co-extraction of the potassium nitrate salt rendered the interface less polarizable and thereby modulated the potassium uptake wave. The authors stated that such an effect should perhaps be considered an interference rather than an interesting new mechanism but future work will show what this concept holds.

An interesting electrochemical method for the sensitive detection of hydrazines was reported, by the use of supported bilayer lipid membranes incorporating DNA strands with a lipophilic tail[66]. The detection occurred *via* a transient current signal, or short spike, which was evidently caused by a disturbance

of the ion transport properties of the bilayer. The mechanism for the detection of the hydrazine was not completely understood, but while the DNA provided an increase in the detection limit by several orders of magnitude (to sub-ppb levels), it did not appear to selectively bind the hydrazine. Different hydrazines were found to give different spikes at different times and so it was this feature that allowed the researchers to accurately assess the concentrations of hydrazines in sample mixtures.

1.3 Crown Ethers

There are numerous examples in the literature of crown ethers involved in the direct sensing of analytes, notably metal cations. Normally combined with a redox active centre[67-69] they are able to detect a variety of metal cations by simply varying the size of the crown ether cavity. Most of the literature written about crown ethers concerns the detection or recognition of alkali and alkaline earth metal cations. The most notable work concerns Li^+, Na^+ and K^+ ions, although some attention is also given to Ag^+. This is presumably due to the much greater binding affinity of Ag^+ for the nitrogen atom in azacrown ethers compared to the other Group 1 metal cations.

Work by Gokel[70] explored the idea of using an indole sidearm of tryptophan as a π-donor for the study of alkali metal cation- π interactions. In complexes with Na^+ or K^+, the metal cation is bound equatorially by the crown macroring and the sidearm occupies the axial positions (in this case either the 3- or 5-position of a 15- or 18-membered azacrown derivative). The position of the sidearm attachment in these complexes controls whether benzo or pyrrolo subunits (of indole) serve as π-donor for the ring bound Na^+ or K^+ ion. Steric factors were found to influence contact between the ring bound cation and the benzo/pyrrolo subunit with calculations showing the benzene ring to be the preferential binding site over the pyrrolo subunit. This was ascribed to the more electron rich donor site although experiments did show that selective preferential binding to the pyrrolo subunit occurred when using a bis(indole) framework.

Heavy metal sensing devices continue to inspire widespread research as the need for detecting environmental pollutants remains extremely important. Two papers from different research groups citing the preferential binding of a heavy metal

ion over a variety of alkali, alkaline metal and transition metal ions have been reported. The group of Chen *et al*[71] chose a ketoaminocoumarin (7-diethylamino-3-(4-dimethylaminobenzoyl)coumarin) with a 15-membered azacrown derivative in acetonitrile using fluorescence spectroscopy to determine the binding of metal cations. They found typically the univalent ions did not cause significant changes in either adsorption or emission spectra whereas red-shift adsorptions were observed upon the addition of the divalent metal ions. The preferential selectivity of the ketoaminocoumarin for Pb^{2+} over the other divalent ions was a significant result. In some cases the binding constant was measured to be a factor of 100 times greater, a fact noted for its importance as Pb^{2+} targets and competes with Ca^{2+} and Zn^{2+} binding sites. Chang *et al*[72] had similar results for the binding of Hg^{2+} using a p-*tert*-butylcalix[4]arene-azacrown ether in a range of solvents. The anthracene subunit that was used was chosen in this case for its strong fluorescing abilities and relatively well characterized photophysical properties. The Hg^{2+} ion was found to preferentially bind to the host molecule over a variety of other ions, the results of fluorescence spectroscopy confirming trends in the previous cited work.

König *et al*[73] focused on the molecular recognition properties, and binding of inorganic and organic anions to complex metal binding sites with a view to examining the changes of anion properties upon binding. Knowing the high affinity of azacrown ligands for transition metals, experiments were conducted with Zn(II) complexes of 1,5,9-triazacyclodecane, heptacoordinated lanthanide complexes and a variety of anions (OH^-, p-toluenesulphonamide, HCO_3^- and halide ions) in water and DMSO. The affinity constants for the binding of the anions was calculated and, as expected, correlated well with pK_a values of the corresponding conjugated acids of the anions with more basic anions showing a higher binding affinity to the Lewis-acidic zinc binding site of the receptor.

1.4 Gravimetric Sensors

The most common transducer elements of a composite resonator, consisting of a mechanical transducer element, and typically, a chemically sensitive layer, are bulk acoustic wave (BAW), surface acoustic wave (SAW), flexural plate wave (FPW) and

acoustic plate mode (APM). The different classes of sensors mentioned above use piezoelectric substrates for the generation and detection of acoustic waves. Any displacements in the acoustic waves occur predominately at the crystal surface and so a device generating acoustic waves is highly sensitive to mass deposition. At first glance the advantages in sensitivity of these devices are not clearly apparent, the true selectivity is gained from the chemically modified layer interacting with a surrounding medium. The characteristics and advantages of each of the types of Thickness Shear Mode (TSM) resonators are summarised below in Table 1.1.

TSM Device	TSM Surface Employed	Typical Frequency (MHz)	Mechanical strength	Temperature stability	Discrete or Multiple unit
BAW	AT-quartz	6-10	Med	High	D
SAW	ST-quartz	90	High	High	D or M
APM	ST-quartz	100	Med	High	D
FPW	ZnO on silicon	4-5	Low	Medium	M

Table 1.1 A comparison of the properties of TSM devices.

It should be noted however, that the thermal stability of these devices decreases considerably when coated with a polymeric substrate for vapour sorption. The effect of liquid loading also affects the temperature stability but is not as significant. The high frequency of operation may lead to high gravimetric sensitivity in the SAW and APM devices in particular but at an expense. It has been found that viscosity sensors operating at a high frequency are affected by the materials that they have attached to them. In some cases, the types of material attached will lower or dampen the maximum viscosity that can be measured. This problem can be averted by using multiple discrete devices that can of course be connected together in arrays for better selectivity or higher accuracy in sensing experiments. These types of sensor are reviewed briefly in the following section and examples are given to highlight some of their common and more relevant uses.

1.4.1 Bulk Acoustic Wave Sensors

The most commonly used bulk acoustic wave sensors are Thickness Shear Mode (TSM) resonators. They differ from SAW devices as the bulk acoustic waves propagate away in a perpendicular direction to the plane of the surface. Most of the practical applications of TSM's are to be found employing quartz crystals where the oscillation frequency tracks the crystal resonance and indicates mass accumulation on the surface of the device. Unfortunately, these devices have the lowest mass sensitivity of the sensors examined here, with typical TSM resonators operating between 5 and 30 MHz. Manufacturing very thin devices that operate at higher frequencies can increase the mass sensitivity, although thinning the sensors beyond the normal nanogram range results in fragile devices that are difficult to manufacture and handle.

1.4.2 Surface Acoustic Wave Sensors

A SAW sensor is most often comprised of a piezoelectric crystal using an interdigital

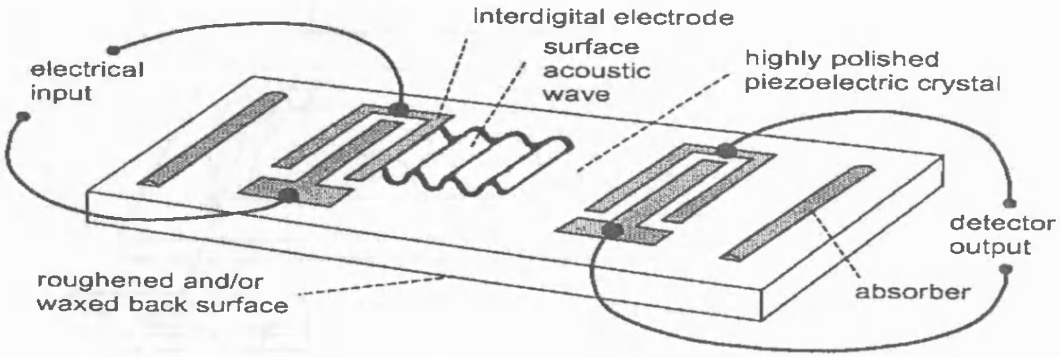

Figure 1.1 Diagrammatical representation of a Surface Acoustic Wave (SAW) sensor[74].

transducer (IDT). The application of a voltage between alternately connected electrodes causes a periodic electric field to be imposed on the crystal. When an alternating voltage is applied, a periodic strain field is generated in the crystal that

produces a standing acoustic wave. This standing wave gives rise to propagating waves that are launched in both directions away from the transducer, the wavefronts being parallel to the transducer fingers. In general, the sensitivity of the sensor is proportional to the amount of energy in the propagation path being perturbed. Bulk acoustic wave sensors typically disperse the energy from the surface through the bulk material to the other side. This distribution of energy minimizes the energy density on the surface, which is where the sensing takes place. SAW sensors, conversely, focus their energy on the surface, tending to make them more sensitive.

1.4.3 Flexural Plate Wave Sensors

Flexural acoustic plate wave sensors[75-76] are generally considered to be the closest relative to SAW sensors. They differ only in the type of acoustic wave that is employed within the device. In the case of FPW's, the velocity of the acoustic wave is lower than the sound velocity in the liquid. As a result they are able to operate extremely effectively when they come into contact with a liquid environment.

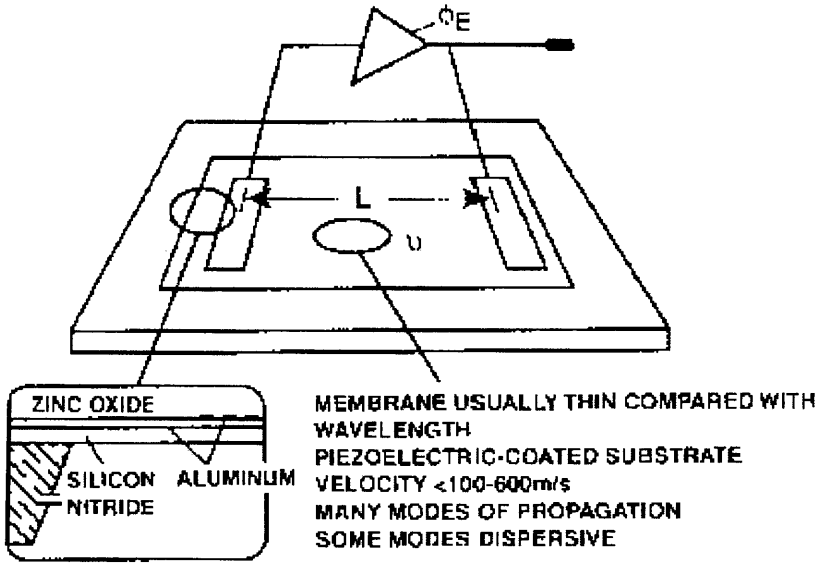

Figure 1.2 Diagrammatical representation of a Flexural Plate Wave (FPW) sensor[74].

As the 'plate' area of a FPW device is only a few μm thick, the mass per unit area of the thin plate can be increased significantly by mass loading produced by the

adsorption of chemical vapours on the plate. This causes the phase velocity to decrease and so the device is ideally suited for biosensing in liquids and in the determination of the viscosities of solvents[77].

1.4.4 Acoustic Plate Mode Sensors

Finally acoustic plate mode devices, or more correctly shear-horizontal acoustic plate mode devices (SH-APM), have been predominately developed for sensing in liquids. SH modes have particle displacement parallel to the surface of the device and normal to the direction of propagation. The absence of a surface-normal component of displacement allows each SH plate to propagate in contact with a liquid without coupling excessive amounts of acoustic energy into the liquid.

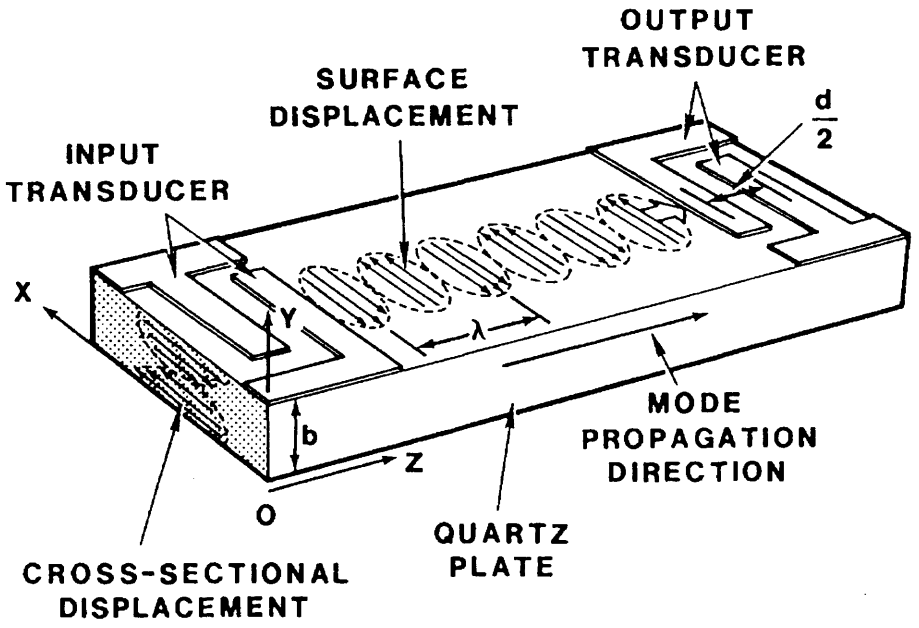

Figure 1.3 Diagrammatical representation of an Acoustic Plate Mode (APM) sensor[74].

By comparison, surface acoustic waves are propagated at a solid/liquid interface, the surface-normal displacement radiates compressional waves into the liquid and severely attenuates the wave. The high sensitivity of APM devices makes them ideal for the sensing of submonolayer deposition.

1.5 Performance Criteria

In developing a sensor for a given application, numerous considerations must be taken into account including reversibility, response time, stability and environmental effects; however the most important considerations are selectivity, sensitivity and the detection limit.

1.5.1 Selectivity

Selectivity refers to the ability of a sensor to discriminate between the target analyte of interest and possible interferences. For acoustic wave sensors, this characteristic is determined by the properties of the film coating. For example, a polar fluoropolyol (FPOL) film coating shows preferential selectivity for butanone over isooctane compared to a non-polar polyisobutylene (PIB) film coating[78]. Inherent selectivity for a single analyte is virtually impossible if the film coatings are simple polymer, organic or inorganic films. In many cases, however, adequate selectivity for a particular application can be achieved if the nature and number of potential interferences is known. Although this constraint applies to all monitoring systems it should not be seen as a limitation in sensor design.

There is a considerable volume of literature on the evaluation and merits of individual film coatings[79-80], although the comprehensive testing of selectivity for most target analytes has been limited. As water vapour is omnipresent and therefore not considered an interference, it seems strange that many sensors have not been evaluated for their response to relative humidity. This has only occurred in a few examples[81-82]. In the instances where the response to potential interfering compounds has been investigated, it was usually by exposing the sensor to the target analyte and interfering compounds individually. Rarely have sensors been exposed to more than one species[83]. It has been argued that in these cases, the separate responses accurately indicate the presence (or absence) of an interfering signal. Unfortunately the combined responses have not been extensively demonstrated; the problem being that at high vapour concentrations or when analyte and interferent have significant intermolecular interactions, responses may be non-additive[84].

1.5.2 Sensitivity

Sensitivity is often confused with the detection limit for a sensor. The detection limit is the smallest amount or concentration of a substance required to produce a sensor response that can, with some level of statistical confidence, be differentiated from zero.

Sensitivity is usually defined as the change in sensor output signal obtained for an incremental change in the concentration or mass of the analyte *i.e.* the slope of the response-*vs.*-concentration curve. Sensitivity for a typical acoustic wave sensor has the units of frequency change/concentration change *e.g.* Hz/(μg/L) or ppm/ppm (normalized frequency shift/concentration). For a given device employing a given acoustic mode, sensitivity to an analyte is determined by the amount of film coating (thickness and/or surface area) and the strength of the analyte-coating interaction. Given the limits on the amount of coating, coating-analyte interaction strength is of paramount importance in determining overall sensitivity and detection limits.

1.5.3 Detection Limit

The dynamic range over which a sensor is effective in determining the response to an analyte is bounded at the upper end by saturation effects, and at the lower end by the detection limit. Analyte concentrations below the detection limit give no detectable response (indistinguishable from noise), while concentrations at or above the saturated limit all yield the same result.

Like the sensitivity, the detection limit depends on the inherent sensitivity of the device itself as well as the kinetics and thermodynamics of the coating-analyte interaction. Unlike sensitivity, the detection limit is also noise dependent. Commonly detection limits are defined as signal-to-noise (S/N) ratios of two or three, corresponding roughly to situations where the signal exceeds the noise at statistical confidence levels of 95% and 99%, respectively[85]. The detection limit is expressed in units of concentration (*e.g.* μg/L or ppm).

For a given amount of coating, there is an upper limit to the concentration or mass of analyte that can be adsorbed/reacted before the capacity of the coating is reached, or the physical properties of the coating are irreversibly altered. Few real-

world thin film materials are perfectly elastic, the consequence of which is film thickness dependent attenuation of the acoustic wave. This is particularly true for polymers above their glass-transition and/or melting temperature. Any material that departs significantly from elastic behaviour has an upper limit of thickness beyond which operation of the acoustic wave device becomes impractical due to excessive attenuation. A prime example of this is the case of viscoelastic polymer films, where the adsorption of an analyte plasticizes the film, increasing acoustic wave attenuation by large amounts.

1.6 Techniques

The techniques used to collect data in this study are listed below with a short summary of the salient points to note. A more substantial overview of the theory behind each of the techniques and any experimental considerations to note are discussed further in the following chapter.

1.6.1 The Quartz Crystal Microbalance (QCM).

This particular technique is discussed in depth in the subsequent chapter. In short, mass deposited onto the surface of a piezoelectric crystal decreases its resonant frequency allowing the determination of deposited mass on the crystal surface to nanogram precision. This dynamic *in situ* technique is commonly used to study the electrochemical deposition of metals and polymers and their subsequent electrochemistry. The main disadvantage of this technique however is the inability to differentiate individual species from frequency shifts alone when dealing with a complex system. When dealing with a single species, a mass-frequency relationship can be used when the contacting mass is rigidly coupled to the resonator's surface.

1.6.2 Crystal Impedance

Upon deviation from the 'rigidity' constraint of a TSM resonator, a crystal impedance technique is employed for thin film characterisation. The technique involves the

detection of the entire crystal impedance spectrum in the region of crystal resonance. The magnitude and shape of the peak are influenced by a variety of film properties including the mass, density and shear modulus of the film being examined. Crystal impedance spectra are acquired by monitoring the current that results from the application of a sinusoidally oscillating potential over a range of frequencies. Crystal parameters can be extracted from the comparison of experimental data with the theoretical responses of electrical equivalent circuits. Crystal impedance electrical equivalent circuit models contain a number of elements (resistive, conductive and inductive) that are representative of the physical properties of surface perturbation. The relationship of these elements to each other is discussed in greater detail in the next chapter.

1.6.3 Cyclic Voltammetry

A simple potential waveform that is often used in electrochemical experiments is the linear waveform, *i.e.* the potential is continuously changed as a linear function of time. The rate of change of potential with time is referred to as the scan rate. The simplest technique that uses this waveform is linear sweep voltammetry. The potential range to be examined is scanned in one direction, starting at the initial potential and finishing at the final potential. A more commonly used variation of the technique is cyclic voltammetry, in which the direction of the potential is reversed at the end of the first scan. This has the advantage that the product of the electron transfer reaction that occurred in the forward scan can be probed again in the reverse scan. In addition, it is a powerful tool for the determination of formal redox potentials, detection of chemical reactions that precede or follow the electrochemical reaction and evaluation of electron transfer kinetics. The basic shape of the current response for a cyclic voltammetry experiment is described below. At the start of the experiment, the bulk solution contains only the reduced form of the redox couple (R) so that at potentials lower than the redox potential, *i.e.* the initial potential, there is no net conversion of R into the oxidized species (O). As the redox potential is approached, there is a net anodic current that increases exponentially with potential. As R is converted into O, concentration gradients are set up for both R and O, and diffusion occurs down these concentration gradients. At the anodic peak, the redox potential is sufficiently positive that any of the reduced species R that reaches the

electrode surface is instantaneously oxidised to O. The current therefore depends upon the rate of mass transfer to the electrode surface.

1.7 Objectives

The aims of the research presented in this thesis are two-fold. The first is to explore the possibility of using selected quaternary ammonium binaphthyl salts (QABS) as possible receptors for the recognition of a variety of analytes. The range of analytes includes simple metal cations and carboxylic acids. The interactions between the binaphthyl receptors and analytes will be determined by using a variety of techniques, notably cyclic voltammetry, to gain insight into the effect on the electrochemical response of the receptor/analyte system. Other techniques will be used to collect information on the binding site between receptor and analyte *i.e.* the geometry and nature of binding. Once established the effect of analyte size and receptor shape will be explored and it is hoped to introduce an element of chirality into the binaphthyl receptors to see if there is the possibility of being able to differentiate one chiral enantiomer from another.

Secondly, it is planned to interpret the data from a Quartz Crystal Microbalance (QCM) of a polymer wax film in a viscoelastic regime, and to extend the analysis to a system with an interacting surfactant medium. Thin rigid films can be studied *in situ* using the QCM, which is also referred to as a Thickness Shear Mode (TSM) resonator in some studies. The high resolution of the technique provides information about the changes in a film's composition and/or properties. Due to the piezoelectric properties of quartz, mechanical resonance can be electrically excited and detected. Crystal impedance experiments are able to exploit this property and enable a TSM resonator to be used a method for the characterisation of polymer films. Complex analysis of crystal impedance data provides the opportunity to extract qualitative information of the physical nature of the film being investigated. Of particular interest is a parameter called the shear modulus (G) and it is used to provide information on structural rigidity.

1.8 References

1) K.Kroger, A.Jung, S.Reder and G.Gauglitz, *Analytica Chimica Acta*, **469**, (2002), 37.
2) A.A.Ensafi and A.Kazemzadeh, *Microchemical Journal*, **72**, (2002), 193.
3) E.Comini, M.Ferroni, V.Guidi, G.Faglia, G.Martinelli and G.Sberveglieri, *Sensors and Actuators B*, **B84**, (2002), 26.
4) E.Dominguez and S.Alcock, *Biosensors and Bioelectronics*, **17**, (2002), 625.
5) B.D.Spangler, E.A.Wilkinson, J.T.Murphy and B.J.Tyler, *Analytica Chimica Acta*, **444**, (2001), 149.
6) D.R.Sparks, M.I.Chia and G.Q.Jiang, *Sensors and Actuators, A:Physical*, **A95**, (2001), 61.
7) D.L.Recalde-Ruiz, E.Andres-Garcia and M.E.Diaz-Garcia, *Analyst*(Cambridge), **125**, (2000), 2100.
8) J.J.Roberts, *Journal of Applied Physics*, **91**, (2002), 1687.
9) E.H.Hartz, A.Andresen, M.W.Martin and K.V.Hodges, *Journal of the Geological Society*, **157**, (2000), 795.
10) J.Voros, R.Graf, G.L.Kenausis, A.Bruinink, J.Mayer, M.Textor, E.Wintermantel and N.D.Spencer, *Biosensors and Bioelectronics*, **15**, (2000), 423.
11) G.K.Budnikov, *J.Analytical Chemistry*, **55**, (2000), 1014.
12) J.P.Whitelegge and J.le Coutre, *Am.J.Pharmacogenomics*, **1**, (2001), 29.
13) K.Stephenson, Y.Yamaguchi and J.A.Hoch, *J.Biological Chemistry*, **275**, (2000), 38900.
14) P.C.Ojimelukwe, *Journal of Food Biochemistry*, **25**, (2001), 411.
15) N.Chattopadhyay, *Int.J.Biochemistry and Cell Biology*, **32,** (2002), 789.
16) J.W.Steed, *Chemistry Review* (Deddington, UK), **6**, (1997), 2.
17) P.D.Beer, N.C.Fletcher, A.Grieve, J.W.Wheeler, C.P.Moore and T.Wear, *J.Chem.Soc.Perkin Trans. 2*, (1996), 1545.
18) F.P.Schmidtchen, *J.Am.Chem.Soc*, **108**, (1986), 8249.
19) V.W-W.Yam, Y-L.Pui, W-P.Li, K.K-W.Lo and K-K.Cheung, *J.Chem.Soc.Dalton Trans.*, (1998), 3615.
20) M.R.Ganjali, A.Rouhollahi, A.R.Mardan and M.Shamsipur, *J.Chem.Soc.Faraday Trans.*, **94**(14), (1998), 3615.

21) V.L.M.J.Aarts, C.J.van Staveren, P.D.J.Grootenhuis, J.van Eerden, L.Kruise, S.Harkema and D.N.Reinhoudt, *J.Am.Chem.Soc*, **108**, (1986), 5035.

22) J-S.Lee, J-H.Lee and S-H.Hong, *Sensors and Actuators, B:Chemical*, **B89**, (2003), 311.

23) X.Zhang, J.Lin, L.Cardoso, M.Broderick and V.Darley-Usmar, *Electroanalysis*, **14**, (2002), 697.

24) G.K.Kannan, A.T.Nimal, U.Mittal, R.D.S.Yadava and J.C.Kapoor, *Sensors and Actuators, B:Chemical*, **B101**, (2004), 328.

25) E.C.Riesgo, A.Credi, L.De Cola and R.P.Thummel, *Inorg.Chem.*, **37**, (1998), 2145.

26) P.D.Beer and M.Shade, *Chem.Commum.*, (1997), 2377.

27) T.Shioya and T.M.Swager, *Chem.Commum.*, (2002), 1364.

28) W-L.Xing and X-W.He, *The Analyst,* **122**, (1997), 587.

29) K.Hirose, K.Ogasahara, K.Nishioka, Y.Tobe and K.Naemura, *J.Chem.Soc.Perkin Trans. 2*, (2000), 1984.

30) M.Almaraz, C.Raposo, M.Martín, C.Caballero and J.R.Morán, *J.Am.Chem.Soc*, **120**, (1998), 3516.

31) J.Canceill, L.Lacombe and A.Collét, *J.Am.Chem.Soc*, **107**, (1985), 6993.

32) J.D.R.Thomas, Pure *Appl.Chem.*, **73**, (2001), 31

33) R.P.Buck and E.Lindner, *Anal.Chem.*, **73**, (2001), 88A.

34) E.Lindner and J.P.Buck, *Anal.Chem.*, **72**, (2000), 336A.

35) J.Janata, *Anal.Chem.*, **73**, (2001), 150A.

36) R.E.Gyurcsanyi, E.Pergel, R.Nagy, I.Kapui, B.T.T.Lan, K.Toth, I.Bitter and E.Lindner, *Anal.Chem.*, **73**, (2001), 2104.

37) E.Bakker and E.Pretsch, *Trends Anal.Chem.*, **20**, (2001), 11.

38) A.Ceresa, E.Bakker, B.Hattendorf, D.Günther and E.Pretsch, *Anal.Chem.*, **72**, (2001), 343.

39) A.C.Ion, E.Bakker and E.Pretsch, *Anal.Chim.Acta.*, **71**, (2001), 440.

40) W.Qin, T.Zwickl and E.Pretsch, *Anal.Chem.*, **72**, (2000), 3236.

41) T.Vigassy, W.E.Morf, M.Badertscher, A.Ceresa, N.F.de Rooij and E.Pretsch, *Sens. Actuators B*, **B76**, (2001), 477.

42) R.de Marco and D.J.Mackay, *Mar.Chem*, **68**, (2000), 283.

43) C.M.G.van den Berg, *Mar.Chem*, **71**, (2000), 331.

44) K.Kimura, S.Yajima, K.Okamoto and M.Yokoyama, *J.Mater.Chem.*, **10**, (2000), 1819.

45) J.Shah, J.W.Brown, E.M.Buckley-Dhoot and A.J.Bandara, *J.Mater.Chem.*, **10**, (2000), 2627.

46) K.Kimura, Y.Kawai, S.Yajima and Y.Sakurai, *Chem.Commun.*, (2001), 1302.

47) M.Fibbioli, W.E.Morf, M.Badertscher, N.F.de Rooij and E. Pretsch, *Electroanalysis*, **12**, (2000), 1286.

48) J.H.Han, G.Cui, S.J.Kim, S.H.Han, G.S.Cha and H.Nam, *Analyst*, **126**, (2000), 2040.

49) D.P.Quan, C.X.Quang, L.T.Duan and P.H.Viet, *Environ.Monit.Assess.*, **70**, (2001), 153.

50) J.Bobacka, T.Lahtinen, J.Nordman, S.Haggstrom, K.Rissanen, A.Lewenstam and A.Ivaska, *Electroanalysis*, **13**, (2001), 723.

51) J.Bobacka, A.Lewenstam and A.Ivaska, *J.Electroanal.Chem.*, **509**, (2001), 27.

52) A.Michalska, U.Nadrzycka and K.Maksymiuk, *Electrochim.Acta.*, **46**, (2001), 4113.

53) A.Ahmadi, G.Attard, J.Feliu and A.Rodes, *Langmuir*, **15**, (1999), 2420.

54) G.Attard, A.Ahmadi, J.Feliu, A.Rodes, E.Herrero, S.Blais and G.Jerkiewicz, *J.Phys.Chem.B*, **103**, (1999), 1381.

55) G.Attard, *J.Phys.Chem.B*, **105**, (2001), 3158.

56) Y.Kitamura, T.Uzawa, K.Oka, Y.Komai, H.Ogawa, N.Takizawa, H.Kobayashi and K.Tanishita, *Anal.Chem.*, **72**, (2000), 2957.

57) M.H.Schoenfisch, K.A.Mowery, M.V.Rader, N.Baliga, J.H.Wahr and M.E.Meyerhoff, *Anal.Chem.*, **72**, (2000), 1119.

58) M.Pikulski and W.Gorski, *Anal.Chem.*, **72**, (2000), 2696.

59) J.Wang and X.Zhang, *Anal.Chem.*, **73**, (2001), 844.

60) G.D.Brindley, O.D.Fox and P.D Beer, *Dalton*, (2000), 4354.

61) T.D.Chung, J.Park, J.Kim, H.Lim, M-J.Choi, J.R.Kim, S-K.Chang and H.Kim, *Anal.Chem*, **73**, (2000), 3975.

62) Y.Ge and D.K.Smith, *Anal.Chem.*, **72**, (2001), 1860.

63) M.Gianetto, G.Mori, A.Notti, S.Pappalardo and M.F.Parisi, *J.Chem.Eur.*, **7**, (2001), 3354.

64) S.Cosnier, C.Gondran, R.Wessel, F.P.Montforts and M.Wedel, *J.Electroanal.Chem.*, **488**, (2000), 83.

65) Q.Qian, G.S.Wilson, K.Bowman-Jones and H.H.Girault, *Anal.Chem.*, **73**, (2001), 497.

66) C.G.Siontorou, D.Pnikolelis and U.J.Krull, *Anal.Chem.*, **72**, (2000), 180.

67) A.J.Pearson, J-J Hwang and M.E.Ignatov, *Tetrahedron Letters*, **42**, (2001), 3537.

68) D.A.Gustowski, V.J.Gatto, A.Kaifer, L.Echegoyen, R.E.Godt and G.W.Gokel, *Chem. Commun.*, (1984), 923.

69) A.Kaifer, D.A.Gustowski, L.Echegoyen, V.J.Gatto, R.A Schultz, T.P Cleary, C.R Morgan, D.M.Goli, A.M.Rios and G.W.Gokel, *J.Am.Chem.Soc*, **107**, (1985), 1958.

70) J.Hu, L.J.Barbour and G.W.Gokel, *J.Am.Chem.Soc*, **124**, (2002), 10940.

71) C-T.Chen and W-P.Huang, *J.Am.Chem.Soc*, **124**, (2002), 6246.

72) N.R.Cha, M.Y.Kim, Y.H.Kim, J-I.Choe and S-K.Chang, *J.Chem.Soc.Perkin Trans.*, **2**, (2002), 1193.

73) R.Reichenbach-Klinke and B.König, *J.Chem.Soc.Dalton Trans.*, (2002), 121.

74) Thesis of Mark Brown, University of Leicester (1997).

75) E.T.Zellers, R.M.White and S.W.Wenzel, *Sensors And Actuators*, **14**, (1988), 35.

76) S.J.Martin and G.C.Frye, *Appl.Phys.Lett.*, **57**, (1990), 1867.

77) T.K.Eto, B.J.Costello, S.W.Wenzel, R.M.White and B.Rubiusky, *J.Biomech.Eng.*, **115**, (1993), 329.

78) S.L.Rose-Pehrsson, J.W.Grate, D.S.Ballantine and P.C.Jurs, *Anal.Chem.*, **60**, (1988), 2801.

79) A.F.Holloway, A.Nabok, M.Thompson, A.K.Ray and T.Wilkop, *Sensors And Actuators*, **B14**, (2004), 355.

80) H.Helle, P.Vuoriranta, H.Välimäki, J.Lekkala and V.Aaltonen, *Sensors And Actuators*, **B65**, (2000), 296.

81) E.T.Zellers and M.Han, *Anal.Chem.*, **68**, (1996), 2409.

82) F.Benmakroha and J.F.Alders, *Anal.Chim.Acta,* **317**, (1995), 281.

83) G.Zhang and E.T.Zellers, *Anal.Chem.*, **65**, (1993), 1340.

84) E.T.Zellers and G.Zhang, *Anal.Chem.*, **64**, (1992), 1277.

85) F.A.Graybill, *An Introduction To Linear Statistical Models*, McGraw Hill: New York, (1961), 125.

Chapter 2
Theory

2.1 Introduction

This chapter describes the theory behind the technique of the quartz crystal microbalance. It explains how raw experimentally determined crystal impedance spectra can be converted into meaningful shear modulus data. A brief section on the technique of cyclic voltammetry is included as well, since this was the method used to collect limiting current data for the electrochemical sensor work.

A thin rigid layer on a TSM resonator can be interpreted by the Sauerbrey equation to give information on the mass changes occurring at the electrode surface *via* associated shifts in frequency. The technique is widely used[1-5] but does have its limitations due to assumptions that are made for the approximation in converting frequency shift into a change in mass[6]. It can also be seen that from the frequency changes alone[7], it is difficult to distinguish between changes in the mass deposited on the resonator surface or viscosity changes from a contacting liquid. Another technique for obtaining the relevant TSM resonator data is the crystal impedance method and is described fully in section 2.2. With this technique, the viscoelastic properties of overlayers can be obtained quite readily. The focus is on the quantitative analysis of crystal impedance data by looking at the electrical characteristics of the spectra obtained, these give information on the physical parameters of not only rigid layers but also viscoelastic layers (polymers, liquids etc).

A relatively new method of analysis has been developed for the extraction of the physical parameters (viscosity, density and shear modulus) for chemically and physically different systems on a quartz crystal microbalance[8]. For a long time it had been assumed that there was no viscoelastic loss within the film and that the Sauerbrey approximation was valid[9-10]. Once it became evident that the viscoelastic properties made a considerable contribution to the final response of the resonator, the crystal impedance technique became more widely used. Equivalent circuit analysis[11-16] has allowed the interpretation of data in terms of electrical components[17-21] that indirectly give information on the viscoelastic properties of films.

2.1.1 The Piezoelectric Effect

The piezoelectric effect, was first demonstrated in 1880 by Pierre and Jacques Curie[22]. They applied a stress to the surfaces of various crystals and observed that an electrical potential was produced between these surfaces, the electrical potential generated being proportional to the applied stress. The phenomena is only seen in materials with ionic crystalline structures that do not possess a centre of symmetry, the most notable being quartz. The distortion of a crystal lattice by an applied stress rearranges the electric dipoles within the crystal structure and gives rise to the net dipole moment responsible for detecting the voltage change. The opposite effect is also true. Termed the 'converse piezoelectric effect', an applied potential causes deformation of a crystal lattice resulting in a mechanical strain upon the surface of the crystal.

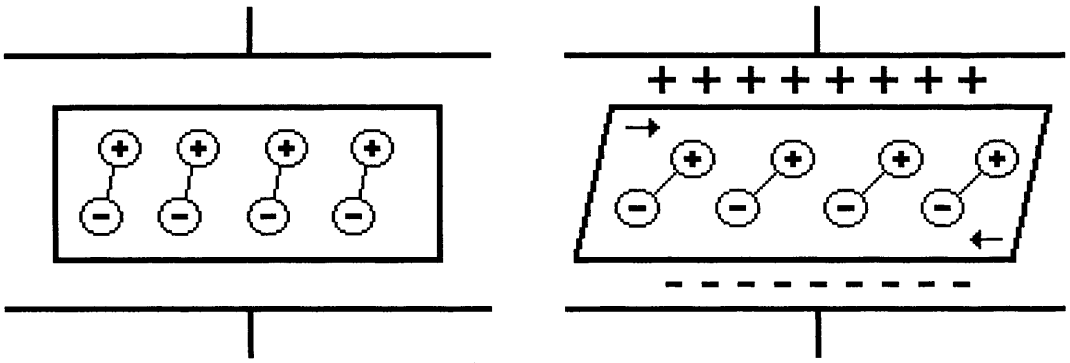

Figure 2.1 Representation of shear motion induced by the converse piezoelectric effect.

The principles behind the converse piezoelectric effect are widely used today in quartz thickness shear mode resonators. An applied voltage with sinusoidally alternating polarity causes an alternating deformation in the crystal, with opposite potential polarities giving rise to crystal deformations equal in magnitude but opposite in direction.

The most commonly used material in thickness shear mode resonators is quartz. Quartz displays excellent mechanical and thermal stabilities making it ideal for use in frequency control and highly stable oscillator devices[23]. The natural state of quartz however, exhibits many piezoelectric vibrations in different directions

identifiable by their fundamental motions. By suppressing various modes of vibration it is possible to select a desirable one from within the crystal. This is achieved by using quartz wafers cut at particular crystallographic orientations. Those cut at 35° 15' and 49° 00' with respect to the crystallographic axes yield quartz vibrating in the thickness shear mode and are known as AT-cut and BT-cut quartz respectively. AT-cut quartz is more commonly used, as it possesses a resonant frequency less susceptible to temperature changes around room temperature.

2.1.2 The Sauerbrey Equation

Thickness shear mode oscillators have a natural vibrational frequency known as the resonant or fundamental frequency, analogous to a mass on a spring or vibrating string. Lord Rayleigh demonstrated in 1945 that the resonant frequency of a vibrating body is inversely proportional to its mass[24]. In 1959 Sauerbrey first identified the frequency-mass relationship for an AT-cut quartz crystal[25]. Sauerbrey postulated that a sufficiently small change in mass at the surface of the crystal could be treated as a change in mass of the crystal itself[26]. The resonant frequency, f_0, of an AT-cut quartz resonator with a mass M_q and a thickness h_q attached to it is given by:

$$f_0 = \frac{V_q}{\lambda_q} = \frac{V_q}{2h_q} \tag{2.1}$$

Where λ_q is the wavelength (equal to $2h_q$) and V_q is the speed of the wave in the quartz. Therefore it follows that a change in the thickness of the quartz will affect its resonant frequency:

$$\frac{\Delta f_0}{f_0} = -\frac{\Delta h_q}{h_q} \tag{2.2}$$

With a relative increase in the crystal thickness causing a decrease in the resonant frequency. This can also be explained in terms of the mass of the crystal.

$$\frac{\Delta f_0}{f_0} = -\frac{\Delta M_q}{M_q} \tag{2.3}$$

Combining equations 2.2 and 2.3 yields:

$$\Delta f_0 = \left(\frac{2f_0^2}{\rho_q V_q}\right)\frac{\Delta M_q}{A} \tag{2.4}$$

Where A is the piezoelectrically active area (cm^2), ρ_q is the density of the quartz (2.648 g cm^{-3}) and V_q is the acoustic velocity of quartz ($3.34x10^5$ cm s^{-1}). Substituting in to equation 2.4 above, we now get:

$$\Delta f_0 = -2.26x10^{-6} f_0^2 \frac{\Delta M_q}{A} \tag{2.5}$$

Sauerbrey assumed that small, rigid, uniformly distributed masses deposited on the surface of the resonator could be treated as an extension of the mass change of the oscillator itself. Equation 2.5, the Sauerbrey equation, can now be written in a more generalised form:

$$\Delta f = -2.26x10^{-6} f_0^2 \frac{\Delta M}{A} \tag{2.6}$$

This equation forms the basis of some acoustic wave sensors, with a change in resonant frequency corresponding to a change in the mass of the material in contact with the resonator surface. This could be due to the electrochemical deposition of a metal from a solution of ions or from the damping of the resonator surface being in contact with a liquid. Several assumptions are made when dealing with the Sauerbrey equation; these are discussed in the following section along with associated problems.

2.1.2.1 Non-Rigidity and Film Thickness

The main limitation of the Sauerbrey equation is that films must be acoustically thin and rigidly adhered to the surface of the TSM resonator if associated changes in mass are to be correctly identified from a shift in frequency response. Analysis of the Sauerbrey equation has been shown to be valid for up to 2% difference in the frequency between the perturbed and unperturbed quartz crystal[27]. For greater loadings on the TSM resonator the energy loss due to viscous drag in the overlayer becomes sufficient enough so that the response is no longer due to the mass changes of the film, but is dependent on the viscoelastic characteristics of the film as represented by the shear modulus. Therefore the overlayer should not experience any shear deformation during resonance for the equation to be valid. The failure of the Sauerbrey equation was first reported when the analysis of a viscoelastic film proved inconclusive[28]. The results were later interpreted by using the knowledge that a combination of shear modulus and density were needed to correctly analyse the films.

2.1.2.2 Uniformity

The overlayer on the TSM resonator needs to be of uniform thickness and composition if results are to be interpreted correctly. A sensitivity gradient is set up over the piezoelectrically active area of the quartz such that there will be a maximum in the amplitude of oscillation[29-30] over the centre of the electrodes. This corresponds to a region of high sensitivity compared to the outer edges where almost no oscillation occurs. The Sauerbrey equation does not take this fact into account and as a result increases the importance in needing to have uniform thickness across the TSM resonator.

2.1.2.3 Stress Effects

The frequency response of a TSM quartz resonator was shown to depend on the elastic energy stored in the quartz crystal itself[31]. The elastic energy was shown to be affected by the mechanical stress applied to the surface of the quartz TSM resonator. The main sources of the stress on the crystal are the electrodes themselves and their fixings onto the crystal. The stress associated with the addition of an overlayer is

minimal in comparison. For example, when analysing metal films, the stress is only a significant effect from the first few monolayers on the surface. Frequency shifts due to mass changes tend to dominate with subsequent overlayers, and so stress effects from films with thicknesses greater than 1μm can largely be ignored.

2.1.2.4 Non-Slip Boundary Condition

It is assumed that the displacement for an overlayer is the same as for the quartz at the quartz-overlayer interface. If, however, the interfacial forces acting between the resonator surface and the overlayer are insufficient, then interfacial slip will occur and a discontinuity in the displacement at the interface is seen. The issue of interfacial slip has been studied[32-35] and it was shown that surface treatments could affect the TSM resonator response with the hydrophobicity of the treated surface being the critical parameter during liquid loading. An alternative explanation was offered[36] that suggested that it was actually the roughness of the quartz surface that affected the resonator response, with the critical parameter being the contact angle of the liquid on the surface of the quartz. Using polished crystals can eliminate this problem, as interfacial slip does not occur.

2.1.2.5 Temperature

It is imperative to know the temperature at which frequency measurements are taken with a TSM resonator, as temperature affects many of the assumptions that are made when using the Sauerbrey equation. The response of the quartz itself is also affected by temperature changes. Temperature also significantly affects properties such as liquid density or viscosity and overlayer rheology which all have an effect on resonator response.

2.2 Equivalent Circuit Representations

TSM devices use a piezoelectric substrate material in which the electrical field generated between the two electrodes couples to the mechanical displacement. This

allows the excitation and detection of mechanical resonances, and therefore mass changes can be calculated from the associated shifts in frequency. In practice, changes in the resonant frequency are measured electrically and the characteristics of the resonator can be described by an equivalent circuit model. An equivalent circuit model[37] describes the impedance (the ratio of applied voltage to current) or admittance (the reciprocal of impedance) over a wide range of frequencies near resonance. There are two types of equivalent circuit models, the distributed or transmission line model and the more commonly used lumped element model (which will be used in this thesis to characterise the electrical parameters obtained from the TSM under investigation).

2.2.1 Distributed line Model

The distributed line model uses a transmission line to represent the propagation of acoustic energy across the device thickness[38-40]. The variables, T (stress) and v (particle velocity) are connected via a transformer to an electrical port. The equivalent circuit model has two acoustic ports and one electrical port.

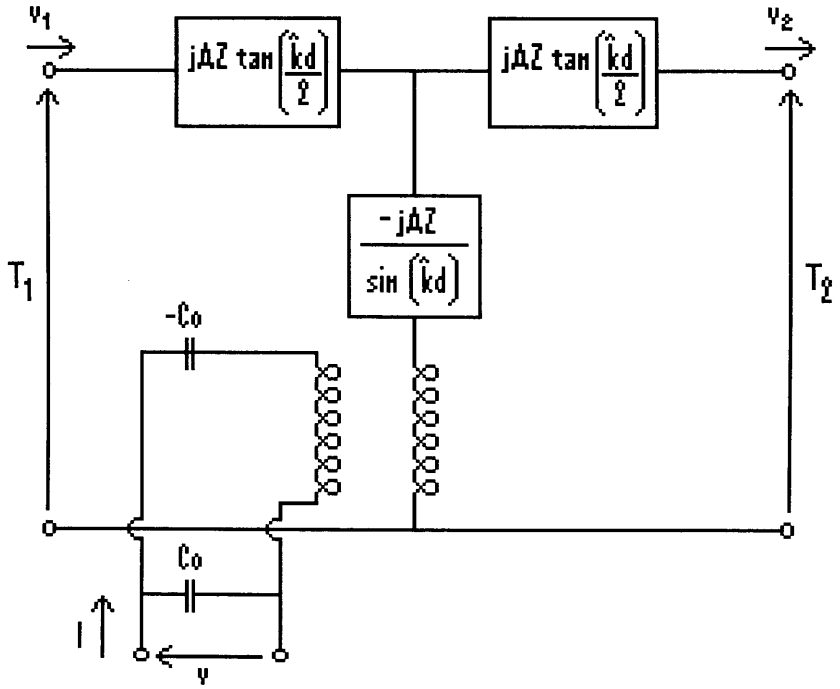

Figure 2.2 Diagram of a Distributed Line Model.

The distribution line model relates the electrical impedance, Z_e, to the surface mechanical impedance, Z_s, and the characteristic shear wave impedance of the quartz, Z_q, by the following equation:

$$Z_e = \frac{N\pi}{4K^2\omega_s C_0}\left(\frac{Z_s}{Z_q}\right)\left[1-\frac{j\dfrac{Z_s}{Z_q}}{2\tan\left(\dfrac{\pi\omega}{2\omega_s}\right)}\right] \tag{2.7}$$

By terminating the acoustic ports in the mechanical impedance representing the surface 'loading condition', the electrical response is obtained from the model of the device.

2.2.2 Butterworth Van Dyke (BVD) Model

The distribution line model can be simplified greatly to the lumped element model also known as the Butterworth Van Dyke (BVD) model[41-42].

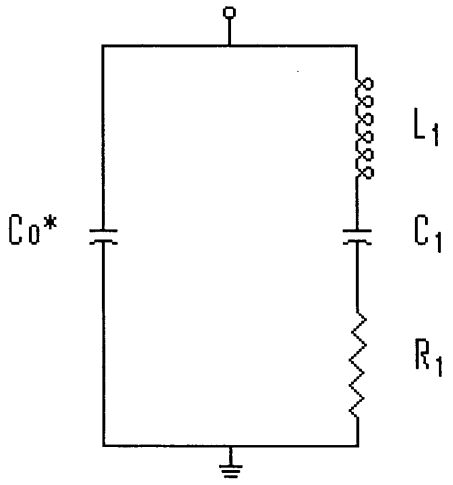

Figure 2.3 The Butterworth Van Dyke Model.

The components in series are defined as follows; C_1 is a capacitor and corresponds to the energy stored during oscillation. The inductor, L_1, affects the electrical response in a similar manner to the displaced mass of an oscillating crystal. Non-elastic deformations occur when the quartz is oscillating; the resistor, R_1, represents heat lost

in this way. The three components together are referred to as the "motional arm" of the circuit, with the other capacitor C_0^*, attached in parallel defined as:

$$C_0^* = C_0 + C_P \tag{2.8}$$

Where C_0 is the static capacitance arising from the metal electrodes attached to the surface of the quartz, and C_P being the parasitic capacitance arising from the geometry of the metal electrodes and the fixture. The static capacitance dominates the electrical behaviour away from resonance, while the motional contribution dominates near resonance. All of the elements so far can be described by equations 2.9(a-d):

$$C_0 = \frac{\varepsilon_{22} A}{h_q} \tag{2.9a}$$

$$C_1 = \frac{8K^2 C_0}{(N\pi)^2} \tag{2.9b}$$

$$L_1 = \frac{1}{\omega_s^2 C_1} \tag{2.9c}$$

$$R_1 = \frac{\eta_q}{\mu_q C_1} \tag{2.9d}$$

Where ε_{22} is the dielectric permittivity, A is the area of the electrode, h_q is the thickness of the quartz, K^2 is the quartz electromechanical coupling coefficient, N is the harmonic number, $\omega_s = 2\pi f_s$, where f_s is the series resonant frequency for the unperturbed quartz resonator, η_q is the quartz effective viscosity and μ_q is the quartz shear stiffness. The total TSM resonator admittance can now be expressed as:

$$Y(\omega) = j\omega C_0^* + \frac{1}{Z_m} \tag{2.10}$$

Where the motional impedance for the unperturbed resonator is:

$$Z_m^0 = R_1 + j\omega L_1 + \frac{1}{j\omega C_1} \tag{2.11}$$

With $j = \sqrt{-1}$.

For resonance to occur, the complex impedance of the quartz crystal oscillator at the resonant frequency must be resistive only *i.e.* the total reactance must be equal to zero. There are two frequencies at which this can happen[43].

1) The series resonant frequency, f_s, where the impedance of the "motional arm" is equal to zero.

$$j\omega_s L_1 + \frac{1}{j\omega_s C_1} = 0 \tag{2.12}$$

Solving for ω_s and noting that $\omega_s = 2\pi f_s$ gives;

$$f_s = \frac{1}{2\pi (L_1 C_1)^{1/2}} \tag{2.13}$$

2) The parallel resonant frequency, f_p, which is defined as the frequency at which the total reactance (motional and static) is equal to zero.

$$f_p = \frac{1}{2\pi}\left[\frac{1}{L_1}\left(\frac{1}{C_1} + \frac{1}{C_o^*}\right)\right]^{1/2} \tag{2.14}$$

These two frequencies correspond to the maxima and minima exhibited below.

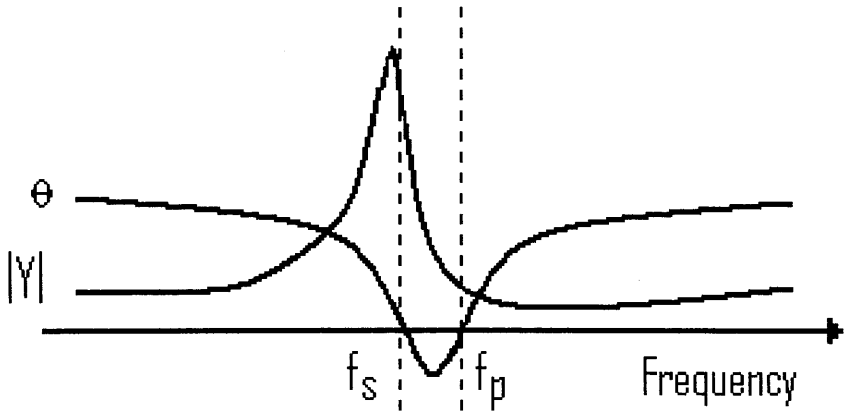

Figure 2.4 Diagram to show the frequencies at which resonance occurs.

The piezoelectric coupling between the mechanical displacement and electrical potential within the quartz can influence the electrical characteristics of the TSM resonator. A continuum model, the lumped element model, can relate the electrical properties of the circuit to the properties of the contacting mass or liquid layer. When the resonator has a surface perturbation, the motional impedance increases. In addition, the surface perturbation causes an increase in the motional impedance, Z_m. The complex electrical impedance describes this:

$$Z_e = \frac{N\pi}{4K^2\omega_s C_o}\left(\frac{Z_s}{Z_q}\right) \tag{2.15}$$

Z_q is the characteristic shear wave impedance of quartz and Z_s is the surface mechanical impedance of the quartz at the surface. This is defined as:

$$Z_s = \left.\frac{T_{XY}}{v_x}\right|_{y=0} \tag{2.16}$$

Where T_{xy} is the sinusoidally steady-state shear stress (force per unit area in the x-direction on a y-normal plane) imposed on the contacting medium by the resonator. v_x is the resulting x-directed surface shear particle velocity. Z_s is complex: the real part, $Re(Z_s)$, is the component of surface stress in phase with the surface particle velocity and represents mechanical power dissipation at the surface of the resonator; the

imaginary part, $Im(Z_s)$, corresponds to the stress component that is 90° out of phase with the particle velocity and represents the mechanical energy storage at the surface. This is represented graphically in Figure 2.5.

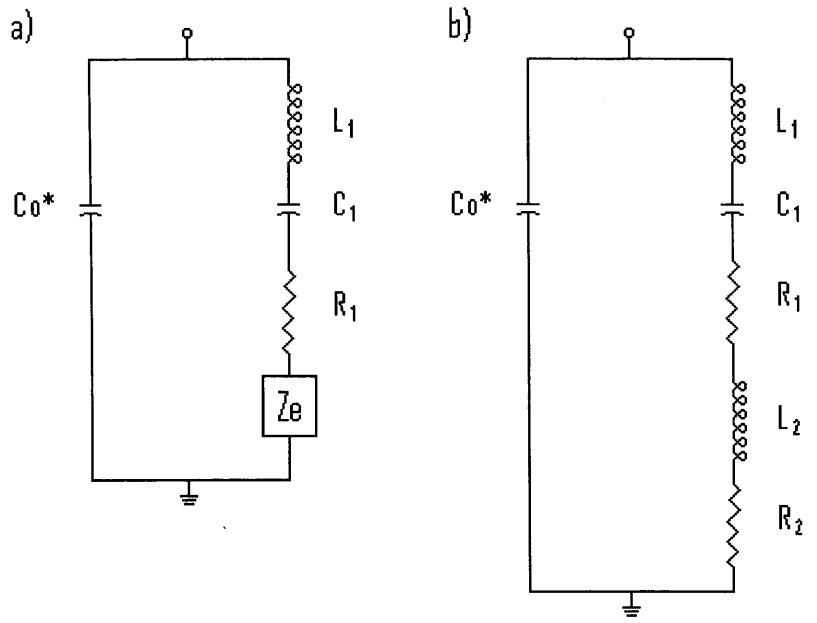

Figure 2.5 Butterworth Van Dyke Model with a) the electrical impedance and b) the same model rewritten with a real motional resistance, R_2 and motional inductance, L_2 included.

Now if Z_e is rewritten as $Z_e = R_2 + j\omega L_2$, this allows Z_e to be represented by a real motional resistance R_2 and inductance L_2 as indicated in Figure 2.5b. Elements R_2 and L_2 can be related to the components of the surface mechanical impedance.

$$R_2 = \frac{N\pi}{4K^2\omega_s C_o}\frac{\mathrm{Re}(Z_s)}{Z_q} \tag{2.17}$$

$$L_2 = \frac{N\pi}{4K^2\omega_s C_o}\frac{\mathrm{Im}(Z_s)}{Z_q} \tag{2.18}$$

The electrical impedance of the resonator with an attached mass or liquid loading can now be modified by combining equations 2.17 and 2.18 with equation 2.11:

$$Z_m = (R_1 + R_2) + j\omega(L_1 + L_2) + \frac{1}{j\omega C_1} \tag{2.19}$$

Since the series resonant frequency[44] is defined as the point where the motional inductance and capacitance resonate, the motional inductance, L_2, causes a shift in the series resonant frequency relative to the unperturbed case. This is given by:

$$\Delta f_s = \frac{-L_2 f_s}{2(L_1 + L_2)} \cong \frac{-L_2 f_s}{2L_1} \tag{2.20}$$

The theory described above can be applied to determine the equivalent circuit model parameters for a TSM resonator in contact with any of the following general classes of surface resonator; an ideal mass layer, a contacting semi-infinite Newtonian liquid or a viscoelastic film. With slight modifications the electrical parameters can be extracted for any type or combination of resonator surfaces as will be seen in the next section.

2.2.3 Comparison of the Models

Comparisons have been made of the parameters extracted from the distributed line and lumped element models when using TSM resonators with different surface perturbations. It has been found that the values obtained do not differ by more than 2% for most of the applications examined operating at the fundamental resonance. It can be seen that by comparing equations 2.7 and 2.15, that for small ratios of Z_s to Z_q, the equation for the distributed line model will reduce to that of the lumped element model. If the ratio of Z_s to Z_q does not exceed 0.1, then the lumped element model always predicts responses to within 1% of those for the distributed line model.

2.3 Physical Models

The general model for surface perturbations on a TSM resonator surface can be modified to take into account changes in the electrical properties of the crystal brought about by the addition of some overlayer on the crystal surface.

2.3.1 Ideal Mass Layer

It is assumed that an ideal mass layer has an infinitesimal thickness, yet contributes a finite areal mass density to the surface of the device. The equivalent circuit model for the mass loaded resonator can be determined from the surface mechanical impedance, Z_s, contributed from a surface perturbation.

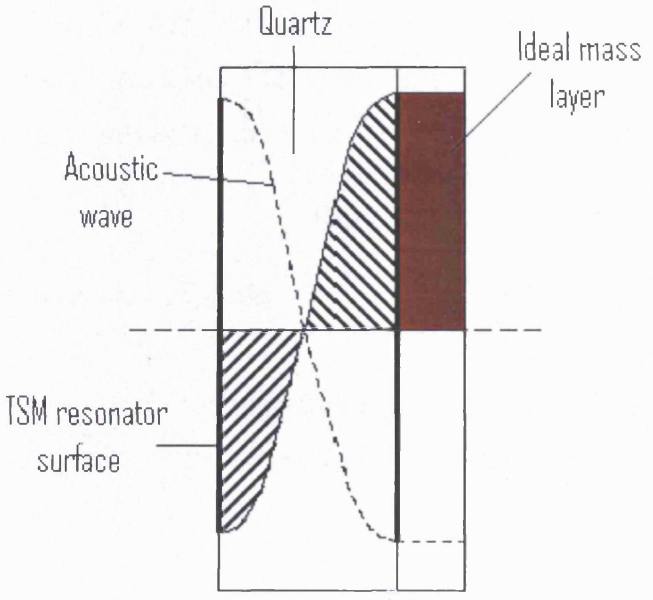

Figure 2.6 Cross-sectional view of a TSM resonator with the top surface in contact with an Ideal Mass Layer.

The surface stress required to sinusoidally accelerate a mass layer is given by:

$$T_{XY} = \rho_s \upsilon_X = j\omega\rho_s \upsilon_X \tag{2.21}$$

Where ρ_s is areal mass density ($\rho_s = \rho_h$ where ρ and h are the film density and thickness respectively) contributed to a mass layer and υ_x is the surface particle velocity. The surface mechanical impedance[45] associated with the mass layer is then:

$$Z_s = \left.\frac{T_{XY}}{\upsilon_x}\right|_{y=0} = j\omega\rho_s \tag{2.22}$$

Combining equation 2.22 above with 2.15 gives the motional impedance elements arising from an ideal mass layer.

$$L_2 = \frac{2\omega_s L_1 \rho_s}{N\pi\sqrt{\mu_q \rho_q}} = \frac{N\pi\rho_s}{4K^2\omega_s C_0\sqrt{\mu_q \rho_q}} \tag{2.23}$$

$$R_2 = 0 \tag{2.24}$$

These equations reflect the fact that the moving surface mass leads to an energy storage (L_2) but no power dissipation ($R_2 = 0$). The energy stored in the inductance arises from the kinetic energy of the mass layer moving synchronously with the resonator surface.

2.3.2 Semi-Infinite Newtonian Liquid

A TSM resonator can be used in conjunction with a liquid to measure the deposition of a species onto the surface of the resonator from the liquid phase, or the properties of the contacting liquid itself.

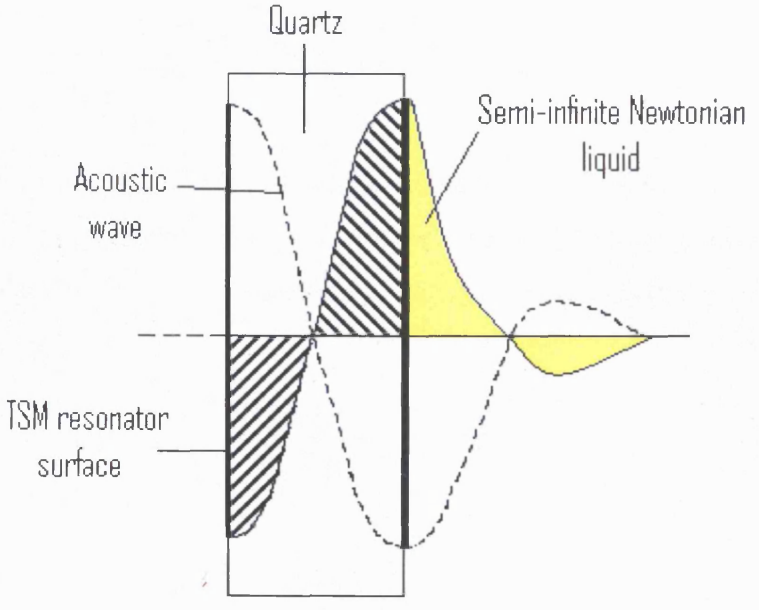

Figure 2.7 Cross-sectional view of a TSM resonator with the top surface in contact with a Semi-Infinite Newtonian Fluid.

A Newtonian fluid by definition is one in which the shear stress and the gradient in the fluid velocity are related by a constant, independent of frequency:

$$T_{XY} = -\eta \frac{\delta \upsilon_x}{\delta y} \tag{2.25}$$

Where η is the shear viscosity of the fluid. The velocity field, υ_x, generated in the contacting medium by the in-plane oscillation of the TSM resonator surface is determined using the Navier-Stokes equation[46] for one-dimensional plane-parallel flow:

$$\eta \frac{\delta^2 \upsilon_x}{\delta y^2} = \rho \upsilon_x \tag{2.26}$$

Where ρ and η are the liquid density and shear viscosity, respectively, and $\upsilon_x = \delta v_x/\delta t$. The solution to this equation with an oscillatory shear driving force at the solid/liquid boundary is:

$$\upsilon_x(y,t) = \upsilon_x e^{-y/\delta} \cos\left(\frac{y}{\delta} - \omega t\right) \tag{2.27}$$

Where y is the distance from the surface, υ_x is the surface particle velocity and δ is the decay length for the envelope of the liquid field velocity. This equation represents a critically damped shear wave radiated into the liquid by the oscillating TSM resonator surface. The decay length is:

$$\delta = \left(\frac{2\eta}{\omega\rho}\right)^{1/2} \tag{2.28}$$

The shear stress imposed by the surface on the liquid to generate the velocity field is:

$$T_{XY} = -\eta \left.\frac{\delta v_x}{\delta y}\right|_{y=o} = \eta \frac{\upsilon_x}{\delta}(1+j) \tag{2.29}$$

By combining equations 2.28 and 2.29 with 2.15, the surface mechanical impedance due to a semi-infinite Newtonian liquid can be determined to be:

$$Z_s = \left(\frac{\omega\rho\eta}{2}\right)^{1/2}(1+j) \tag{2.30}$$

The motional impedance elements arising from liquid loading can be found by using equations 2.31 and 2.32.

$$R_2 = \frac{\omega_s L_1}{N\pi}\left(\frac{2\omega_s\rho\eta}{\mu_q\rho_q}\right) = \frac{N\pi}{4K^2C_o}\left(\frac{\rho\eta}{2\omega_s\mu_q\rho_q}\right)^{1/2} \tag{2.31}$$

$$L_2 = \frac{L_1}{N\pi}\left(\frac{2\omega_s\rho\eta}{\mu_q\rho_q}\right) = \frac{N\pi}{4K^2C_o}\left(\frac{\rho\eta}{2\omega_s\mu_q\rho_q}\right)^{1/2} \tag{2.32}$$

Where $R_2 \equiv \omega_s L_2$ for liquid loading by a Newtonian fluid. Note the parameters R_2 and L_2 are derived for one-sided liquid contact; for the two-sided contact of an insulating fluid, R_2 and L_2 are doubled.

2.3.3 Viscoelastic Layer

The mechanical properties of viscoelastic materials must be described by a complex modulus, for example, the shear modulus is a combination of the storage and loss moduli represented by $G = G' + jG''$. Polymers or other soft materials can be described as viscoelastic materials and as they are widely used in sensor applications it is important to understand how they respond to perturbations on a TSM resonator. A film deposited onto a TSM resonator surface is subjected to an oscillatory driving force at the interface of the TSM resonator/applied film. Normally the film is attached to the TSM resonator surface sufficiently well so that the base of the film moves synchronously with the resonator surface. Sometimes however, the upper portions of the film may lag behind the driven surface.

The equivalent circuit model can be used to describe the near resonance electrical characteristics of the quartz resonator coated with a viscoelastic film. The surface film causes an increase in the motional impedance denoted by the complex element Z_e. This element is proportional to the ratio of the surface mechanical impedance Z_s contributed by the film to the characteristic shear wave impedance Z_q of the quartz. The oscillatory resonance may be considered as a source for shear waves that are radiated into the contacting film.

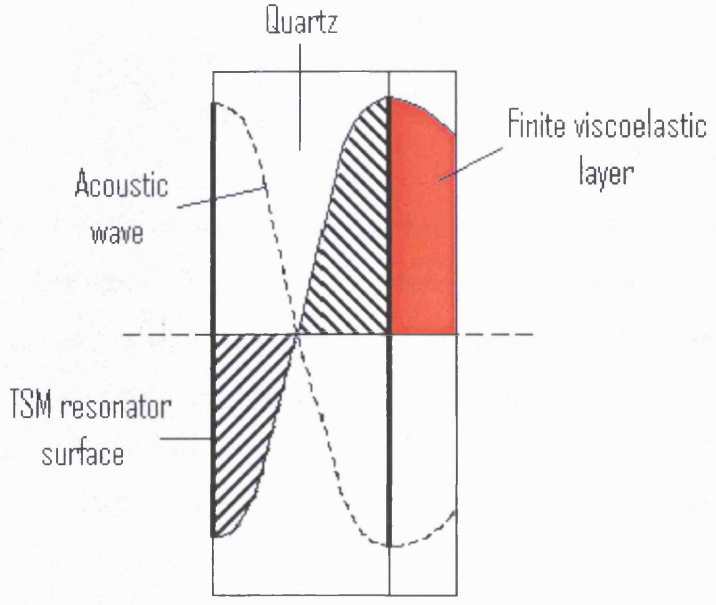

Figure 2.8 Cross-sectional view of a TSM resonator with the top surface in contact with a Finite Viscoelastic layer.

The upper film surface reflects those radiated shear waves downwards so that the surface mechanical impedance seen at the quartz surface is dependant on the phase shift and attenuation undergone by the wave in propagating across the film. When the film is rubbery significant phase shift across the film occurs. The stress-free upper film surface is analogous to a short-circuited electrical transmission line. The input impedance seen at the resonator/film interface is[47]:

$$Z_s = \left(G_f \rho_f\right)^{1/2} \tanh(\gamma h_f) \tag{2.33}$$

With $\gamma = j\omega(\rho_f/G_f)^{1/2}$: G_f and ρ_f are the complex film shear modulus and density respectively, h_f is the film thickness. This equation can be combined with equation 2.15 to find the change in motional impedance that arises from a viscoelastic film on a TSM resonator. For lossless films, $G'' = 0$ and Z_e is imaginary. Z_e then represents energy stored in the film, becoming infinite at film resonance. For lossy films, $G'' > 0$ and Z_e becomes complex with the real part (R_2) representing power dissipation in the film and the imaginary part (L_2) representing energy storage.

$$Z_e = \frac{N\pi}{4K^2\omega_s C_0}\left(\frac{G_f\rho_f}{\mu_q\rho_q}\right)^{1/2}\tanh(\gamma h_f) \tag{2.34}$$

The dependence of Z_e on γh_f makes it difficult to resolve Z_e to real elements R_2 and ωL_2 except in a few cases. A condition of film resonance occurs when the acoustic phase shift φ across the film reaches an odd multiple of $\pi/2$. This enhances the coupling of acoustic energy within the film. Consequently, dramatic changes in the motional impedance occur at film resonance (these arise from the complex Z_e contribution to the film). This can lead to changes in the resonant frequency, f_0, and damping, R_2, for the coated TSM resonator that can be extracted from Z_e.

2.3.4 Multi-Layer Physical Models

The previous sections have only described the perturbations on a resonator surface for a single component in a particular state. In reality, it is much more likely that a resonator will have several overlayers attached to it that will be comprised of different states, *e.g.* an ideal mass layer and a finite viscoelastic layer.

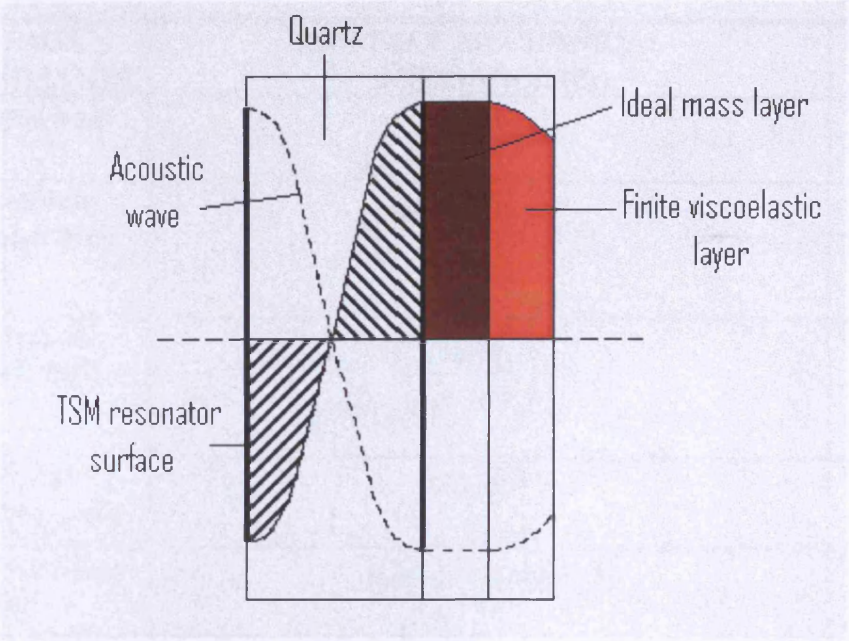

Figure 2.9 Cross-sectional view of a TSM resonator with the top surface in contact with an Ideal Mass Layer and a Finite Viscoelastic Layer.

In order to extract the surface mechanical impedance for this type of resonator surface, it is simply a case of combining the components of the individual overlayers together. The many combinations of resonator type are listed below in Table 2.1 and the reader is referred to these for reference when dealing with other examples not included in this thesis.

SURFACE PERTURBATION	SURFACE MECHANICAL IMPEDANCE (Z_S)	VARIABLES
Ideal mass layer	$j\omega\rho_s$	ρ_s
Semi-infinite Newtonian fluid	$\left(\frac{\omega\rho_l\eta_l}{2}\right)^{1/2}(1+j)$	ρ_l, η_l
Semi-infinite Maxwell fluid	$\left(\frac{j\omega\rho_l\eta_0}{1+j\omega\tau}\right)^{1/2}$	ρ_l, η_0, τ
Semi-infinite viscoelastic layer	$(G\rho_f)^{1/2}$	G', G'', ρ_f
Finite viscoelastic film	$(G\rho_f)^{1/2}\tanh(\gamma h_f)$	G', G'', ρ_f, h_f
Ideal mass layer + semi-infinite Newtonian fluid	$j\omega\rho_s + \left(\frac{\omega\rho_l\eta_l}{2}\right)^{1/2}(1+j)$	ρ_s, ρ_l, h_l
Ideal mass layer + semi-infinite Maxwell fluid	$j\omega\rho_s + \left(\frac{j\omega\rho_l\eta_0}{1+j\omega\tau}\right)^{1/2}$	ρ_s, ρ_l, η_0, τ
Ideal mass layer + semi-infinite viscoelastic layer	$j\omega\rho_s + (G\rho_f)^{1/2}$	ρ_s, G', G'', ρ_f
Ideal mass layer + finite viscoelastic layer	$j\omega\rho_s + (G\rho_f)^{1/2}\tanh(\gamma h_f)$	ρ_s, G', G'', ρ_f, h_f
Multiple viscoelastic layers	$Z_c^{(n)}\left[\frac{Z_c^{(n+1)}\cosh(\gamma^{(n)}h_f^{(n)}) + Z_c^{(n)}\sinh(\gamma^{(n)}h_f^{(n)})}{Z_c^{(n)}\cosh(\gamma^{(n)}h_f^{(n)}) + Z_c^{(n+1)}\sinh(\gamma^{(n)}h_f^{(n)})}\right]$	G', G'', ρ_f, h_f, ρ_l, η_l
Ideal mass layer + multiple viscoelastic layers	$j\omega\rho_s + Z_c^{(n)}\left[\frac{Z_c^{(n+1)}\cosh(\gamma^{(n)}h_f^{(n)}) + Z_c^{(n)}\sinh(\gamma^{(n)}h_f^{(n)})}{Z_c^{(n)}\cosh(\gamma^{(n)}h_f^{(n)}) + Z_c^{(n+1)}\sinh(\gamma^{(n)}h_f^{(n)})}\right]$	ρ_s, G', G'', ρ_f, h_f, ρ_l, η_l

Table 2.1 Table summarising the different types of models and variable parameters for characterisation of a surface modified TSM resonator.

In order to extract the surface mechanical impedance for this type of resonator surface, it is simply a case of combining the components of the individual overlayers together. The many combinations of resonator type are listed in Table 2.1 and the

reader is referred to these for reference when dealing with other examples not included in this thesis.

2.4 Polymer Viscoelasticity

In general, the properties of a polymer that are of interest can be categorised as diffusion/permeation properties or as mechanical (*i.e.* viscoelastic) properties. The measurement of diffusion/permeation properties is straightforward when the diffusion of a species into a polymer film produces a simple mass-loading effect. In addition to this, the presence of dispersed molecules in a polymer can have a plasticizing effect that can induce changes in the viscoelastic properties of the polymer.

2.4.1 Glass Transition Temperature

The viscoelastic properties of a polymer can be described in terms of how the polymer deforms in response to an applied stress. Elasticity refers to the ability of a material to return to its original shape after it has been stressed. Elastic behaviour implies a linear relationship between stress, T, and strain, S, ($T \propto S$). Viscous behaviour implies a linear relationship between shear stress and the rate of strain ($T \propto \delta S/\delta t$). Rigid materials tend to display elastic behaviour, whereas fluid materials display viscous behaviour. In many polymers, a combination of elastic and viscous responses arises, hence the term "viscoelastic" properties.

The two deformation modes of interest are elongation and shear deformation. Elongation refers to the change in length (in a given direction) of a polymer upon application of stress. Shear deformation refers to the deformation behaviour of the polymer under the application of a lateral force on one surface. The way in which a polymer behaves under the force of an applied stress depends upon many variables, including temperature, pressure, and the time (*i.e.* frequency) and nature (*i.e.* shear *vs.* elongation) of the stress.

The viscoelasticity of a polymer can be described by a complex modulus. The modulus is defined as the stress associated with a unit strain, and has units of force/unit area (dynes/cm^2). It can be thought of as the stiffness or rigidity of the

polymer, and is related to the inter- and intra-molecular forces at work within the polymer. In general polymer film/acoustic wave interactions are dominated by the shear component of displacement. The interchangeability between temperature and strain rate in determining the modulus was first probed by Williams, Landel and Ferry[48] and became the basis of the "time-temperature equivalence principle". When a polymer is deformed on a time scale, T_S, that does not allow significant thermal motion of polymer chains with respect to each other (*i.e.* the rotational motion of the polymer chains is limited), the polymer behaves as a rigid or "glassy" material. The glassy state is characterised by a large shear modulus, on the order of 10^{10} dynes/cm^2. As the temperature increases, thermal energy in the system becomes sufficient to overcome the molecular forces, allowing free rotation around the bonds of the polymer chain. This freedom is associated with a softening of the polymer, and the polymer is described as an elastomer. The modulus values of elastomers are on the order of 10^7 dynes/cm^2. The temperature at which the transition from the glassy to the elastomeric state occurs is often called the glass transition temperature T_G.

Another way to look at this is to consider that the polymer exhibits a characteristic relaxation time, τ. If the stress is applied for a long time period T_S that is much shorter than the relaxation time ($T_S << \tau$), polymer chains do not have time to move with respect to each other and the polymer behaves as an elastic solid characterised by a stiffness, μ. As the temperature increases, τ will decrease until $T_S >> \tau$, at which point thermal motion allows the chains to move with respect to each other and the polymer behaves as a viscous liquid characterised by a viscosity η. T_G can be defined as the temperature where $T_S \approx \tau$, at which point the polymer deforms both elastically and viscously, giving rise to viscoelastic behaviour.

It should be noted that the T_G for an amorphous, glassy polymer is not the same as the melting temperature T_M for a semi-crystalline polymer. Both glassy and semi-crystalline materials are characterised by high modulus values, yet the two transition temperatures are associated with distinctly different phenomena. The former (T_G) is a relaxation transition and exhibits a time (frequency) dependence. In addition, the T_G transition generally occurs over a significant temperature range, as the movement of chains over one another is an activated process. The latter (T_M) arises because of a chemical phase change and is independent of frequency. Melting

transitions typically occur in polymers having chains sufficiently linear to allow "packing" in a regular crystalline-like manner.

2.4.2 Time Temperature Equivalence Principle

An increase in the temperature of a polymer stimulates the molecular motion of the chains within the polymer and allows the system to reach equilibrium faster following a mechanical perturbation. This is often expressed by the following equation:

$$a_T = \frac{\tau(T)}{\tau_0(T_0)} \tag{2.35}$$

Where a_T is the characteristic ratio of relaxation time, τ, of a particular response at a temperature, T, to its value, τ_0, at a suitable reference temperature, T_0. For most polymers the shift factor, a_T, does not vary much with τ, so that any changes in temperature only shift the distribution of relaxation times, they do not significantly change them.

If the reference temperature is chosen as the glass transition temperature of the polymer, then general expressions for the dependence of a_T on temperature can be derived. The most widely used is the Williams Landel Ferry (WLF) equation[48].

$$\log a_T = \frac{-C_1(T-T_G)}{C_2+(T-T_G)} \tag{2.36}$$

The parameters C_1 and C_2 were once thought to be universal constants although it has since been shown that they vary from polymer to polymer. Constant C_1 is normally in the range 14 and 17 while constant C_2 is generally between 50 and 100. Equation 2.36 can be used over a wide range of temperatures from T_G to (T_G + 100) K.

Figure 2.10 shows how these characteristics vary with changes in perturbation frequency and relaxation time. The measured modulus value is dependent on both the temperature of the polymer sample and also the frequency with which it is perturbed. At high frequencies (or low temperatures), the time period for which the stress is

applied, T_S, is much shorter than the relaxation time ($T_S << \tau$). In this situation the polymer chains do not have sufficient time to move with respect to each other and the polymer behaves in an elastic manner. If the frequency is decreased (or the temperature raised) until $T_S >> \tau$, then the non-crosslinked polymer chains have the

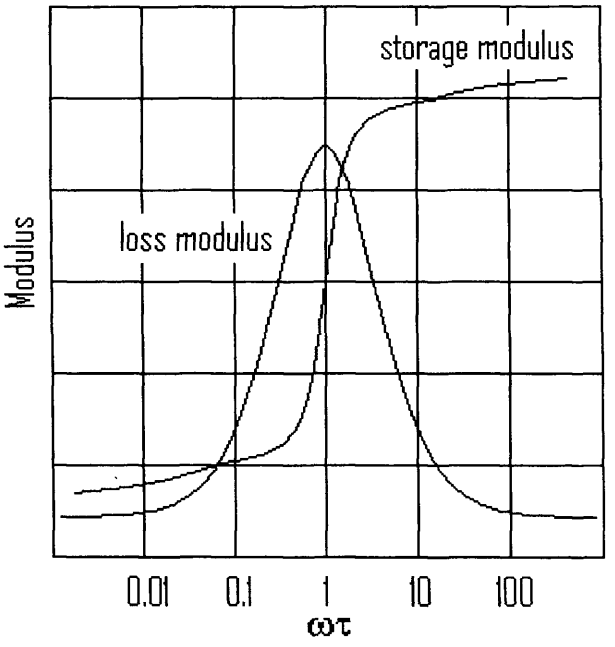

Figure 2.10 Variation of loss and storage moduli with the product of frequency and relaxation time

chance to move with respect to each other and the polymer behaves in a viscous manner. If $T_S = \tau$, then the polymer behaves viscoelastically as the polymer gets close to its glass transition temperature. The glass transition is a second order transition (as opposed to a first order transition such as the melting of ice into water), associated with polymer relaxation processes. Therefore, the temperature at which the glass transition is observed is frequency dependent and often occurs at temperatures several tens of degrees higher than the glass transition is normally observed.

2.4.3 Models Of Viscoelastic Behaviour

Viscoelastic behaviour is commonly modelled as a combination of ideal elastic and viscous elements. Ideal elasticity can be represented by a spring, such as one that

obeys Hooke's Law, with the stress being proportional to the strain as shown in Figure 2.11a.

$$T \propto S \tag{2.37}$$

It should be noted that elastic deformation is instantaneous and independent of time.

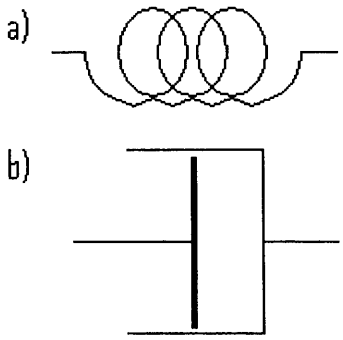

Figure 2.11a) A spring – the mechanical representation of an ideal elastic element and 2.11b) A dashpot - the mechanical representation of a viscous element.

The viscous element can be represented by a dashpot and is representative of a Newtonain liquid. A dashpot has constant viscosity that gives rise to a linear deformation with time while stress is applied. When the stress is removed, the deformation due to the dashpot is unrecoverable and the energy is lost as heat. The stress being proportional to the strain in this case is shown below.

$$T \propto \delta S / \delta T \tag{2.38}$$

The spring and dashpot elements can be connected in two ways: in series or in parallel. When they are connected in series they can be described by the Maxwell model. The Maxwell model responds to an applied stress both viscously and elastically. When the stress is applied, the spring elongates instantaneously and the dashpot yields, when the stress is removed the spring recovers naturally, but the dashpot does not.

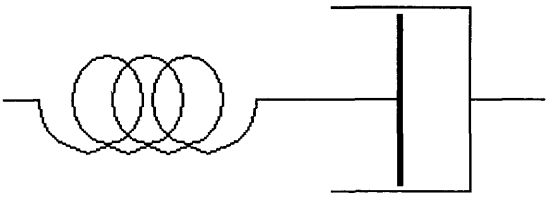

Figure 2.12 Diagram to show a Maxwell model.

A Voigt model arises when the spring and dashpot are connected in parallel. Voigt models exhibit retarded elastic or viscoelastic behaviour upon the application of an applied stress as the dashpot acts as a damping resistance to the establishment of equilibrium in the spring.

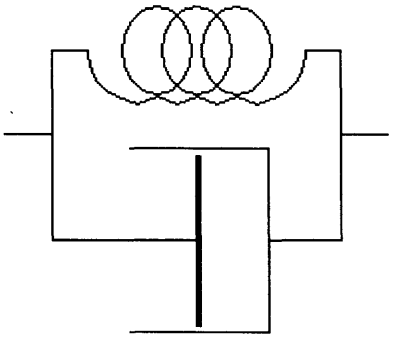

Figure 2.13 Diagram to show a Voigt model.

The Voigt model is more representative of the viscoelastic response of a polymer upon the application of an applied stress than the Maxwell model. However, it is sometimes more useful to describe the behaviour of a polymer as a combination of both types of model, with a distribution of relaxation times.

2.5 Electrochemistry

This section describes the principles behind the techniques of cyclic voltammetry[49-50] used to study a range of analytes in this work. Since cyclic voltammetry is a widely recognised technique in common use today, only a short description will be given. Other techniques have also been used throughout to help predict and characterise analyte binding, namely molecular modelling calculations and ^{1}H-NMR. These are

mentioned briefly in the Experimental chapter (sections 3.2.3.1 and 3.2.3.2) where they are summarised.

2.5.1 Mass Transport

There are three main types of mass transport to be considered in electrochemical systems. These are diffusion, migration and convection. Diffusion is the movement of a species down a concentration gradient and occurs whenever there is a chemical change at a surface. Migration is the movement of a charged species under the influence of a potential gradient. It is the mechanism by which charge passes through an electrolyte solution. The migration of solution species can be neglected however, if there is a large excess of inert electrolyte in solution. Convection is the movement of a species due to mechanical forces operating on it. These can be classed as natural (due to thermal motion) or forced (in the case of a rotating disc electrode experiment). When a rotating disc electrode is used, the flow may be laminar or turbulent depending on the force. If it is laminar then it can be modelled mathematically. The effects of natural convection can be ignored on the shorter timescale.

2.5.2 Fick's Laws of Diffusion

If we consider the general electrochemical reaction;

$$O + ne^- \rightarrow R \tag{2.39}$$

Then the simplest case to consider is linear diffusion to a planar surface or electrode. Fick's first Law of Diffusion states that the flux of reactant O through a plane parallel to the electrode surface is proportional to the concentration gradient, $\delta C_o/\delta x$

$$\text{Flux} = J_o(x,t) = \frac{-D_O \delta C_O(x,t)}{\delta x} \tag{2.40}$$

Where D_o is the diffusion coefficient and x is the distance from the electrode surface. Fick's second Law of Diffusion pertains to the rate of change in concentration of O

with time. The mass transport of species **A** to an electrode surface can be predicted by the following equation;

$$\frac{\delta[A]}{\delta t} = D_A \frac{\delta^2[A]}{\delta x^2} \tag{2.41}$$

Knowing how a species is able to diffuse to and from the surface of an electrode is useful in interpreting the reaction mechanisms of an electrochemical process. An important technique for identifying the products of an electrochemical reaction near the surface of an electrode is Linear Sweep Voltammetry.

2.5.3 Linear Sweep Voltammetry

The potential of the working electrode is swept from a value E_1 at which **A** cannot undergo reduction to a potential E_2, where the electron transfer is driven rapidly. The applied potential E is a function of the speed at which the potential is swept, v_s, and the time of the sweep, t.

$$E(t) = E_1 - v_s t \tag{2.42}$$

The form of the current/voltage behaviour can be understood as follows, on the initial assumption that the **A/B** couple has irreversible electrochemical kinetics. Initially, no current is passed since the applied potential is not large enough to induce electron transfer. But as the potential is swept to more reducing potentials it reaches a point that induces the reduction of **A** to **B** at the electrode surface and current starts to flow. As E is made more negative, the current rises approximately exponentially with potential. As even more negative values are reached the current reaches a maximum and begins to fall. The maximum current is known as the peak current, i_p. Once i_p is reached the magnitude of the current flowing is simply related to the rate at which fresh **A** can diffuse to the electrode surface. Thus the part of the linear sweep voltammogram at potentials more negative than that corresponding to i_p merely reflects the rate at which **A** can diffuse in solution whereas the part of the current/voltage curve that precedes this point is controlled by electrode kinetics.

For any given system, i_p is directly proportional to the concentration of **A** in solution and increases with voltage sweep. Specifically Fick's first Law of Diffusion says that i_p reflects the concentration gradient of **A** near the electrode, which is in turn controlled by the diffusion layer thickness. If the electrode potential is swept more rapidly, then less time is available for electrolysis and depletion of species **A** near the electrode surface is reduced resulting in a thinner diffusion layer and a steeper concentration gradient. The larger flux gives rise to an enhanced i_p.

2.5.4 Cyclic Voltammetry

Linear sweep voltammetry can be extended so that when the potential reaches the E_2 value, the direction of the sweep is reversed and the electrode potential scanned back to its original value. In this way the products of the forward sweep can be analysed during the reverse sweep.

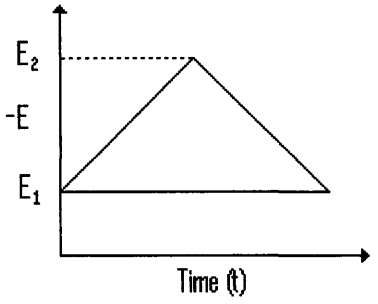

Figure 2.14 Diagram to show the triangular potential in a cyclic voltammetry experiment.

The slope of the voltammogram on the forward sweep is identical to that described for the case of linear sweep voltammetry and depends on the reversibility of the **A/B** redox couple. However on reaching the value E_2 the potential is then swept back, oxidizing species **B** formed at the electrode, driving the forward scan to species **A**. A current in the opposite sense is observed and is due to the oxidation of **B** to **A**. This current increases initially since a high concentration of **B** is present in the diffusion layer and the kinetics for the conversion of **B** to **A** become more favourable as the potential becomes more positive. Gradually species **B**, that is present in the diffusion layer is reconverted to species **A** and the current drops to zero.

The peak potential and the peak size again reflect the reversibility of the **A/B** redox couple. So, if n electrons are transferred in a reversible electrode process the separation becomes;

$$\left|E_p^{ox} - E_p^{red}\right| = 2.218\frac{RT}{nF} \tag{2.43}$$

Regardless of reversibility, the absolute magnitudes of the peak currents for the forward and reverse scans depend on the voltage sweep rate. The terms 'reversible' and 'irreversible' refer to limiting cases according to whether the electrode kinetics are fast or slow relative to the mass transport conditions of the electrode.

2.5.5 Microelectrodes

Linear and cyclic voltammetry typically use macroelectrodes for the analysis of reactants and products in electrochemical reactions. Standard electrode areas in macroelectrodes are typically in the order of 10 mm^2. Despite the obvious advantage of being able to see the products from an electrochemical reaction develop at the surface of the electrode, the disadvantages of their use are discussed in relation to microelectrodes.

Microelectrodes typically have dimensions of around 10 pm^2 or below. These tiny electrodes possess significant advantages over their macroscopic colleagues. For example, microelectrodes have been employed for analytical in-vivo electrochemical measurements.

The current measured at an electrode is a function of its area. Consequently the current measured with microelectrodes is often recorded in nano-amps or below. Microelectrodes, by virtue of the small currents passed through them, induce only a tiny amount of electrolysis. At first sight it may seem paradoxical that electrodes passing tiny current should possess high rates of mass transport. As this is quantified by fluxes of electroactive material that measure the amount of material passing in unit time through unit area. Thus although the currents are small, current density is high. The substantially increased rate of mass transport allows much faster chemical steps in an electrochemical reaction are accessible for study.

Microelectrodes have a much reduced electrode area which significantly reduces the transient current. It follows that microelectrode systems suffer less distortion from so called 'capacitative charging', or, alternatively, the rate at which potential is swept can be made much greater in microelectrode systems. With this in mind, the use of microelectrodes for the study of the binaphthyl receptors in this work has obvious advantages and they have been used throughout this work.

2.6 References

1) B.D.Vogt, E.K.Lin, W-L.Wu and C.W.White, *J.Phys.Chem.B*, **108**, (2004), 12685.
2) A.Bund and M.Schneider, *J.Electrochem.Soc.*, **149**, (2002), 331.
3) J.Kankare, *Langmuir*, **18**, (2002), 7092.
4) A.Baba, F.Kaneko and R.C.Advincula, *Colloids and Surfaces A*, **173**, (2000), 39.
5) G.L.Hayward and G.Z.Chu, *Anal.Chim.Acta.*, **288**, (1994), 179.
6) G.M^{c}Hale and M.I.Newton, *J.Appl.Phys.*, **95**, (2004), 373.
7) P.W.Walton, M.R.O'Flaherty, M.E.Butler and P.Compton, *Biosensors & Bioelectronics*, **8**, (1993), 401.
8) S.J.Martin, H.L.Bandey, R.W.Cernosek, A.R.Hillman and M.J.Brown, *Anal.Chem.*, **72**, (2000), 141.
9) J.Garcia-Jareno, C.Gabrielli and H.Perrot, *Electrochemistry Communications*, **2**, (2000), 195.
10) R.Borjas and D.A.Buttry, *Chemistry of Materials*, **3**, (1991), 872.
11) A.R.Hillman, D.C.Loveday and S.J.Bruckenstein, *J.Electroanal.Chem.*, **300**, (1991), 67.
12) S.Ikeda and N.Oyama, *Anal.Chem.*, **65**, (1993), 1910.
13) A.R.Hillman, D.C.Loveday, M.J.Swann, S.J.Bruckenstein and C.P.Wilde, *The Analyst*, **117**, (1992), 1251.
14) O.Bohnke, B.Vuillemin, C.Gabrelli, M.Keddam, H.Perrot, H.Takenouti and R.Torresi, *Electrochim.Acta.*, **40**, (1995), 2755.
15) T.W.Schneider and D.A.Buttry, *J.Am.Chem.Soc.*, **115**, (1993), 12391.

16) A.P.Clarke, J.G.Vos, H.L.Bandey and A.R.Hillman, *J.Phys.Chem.*, **99**, (1995), 15973.

17) V.E.Granstaff and S.J.Martin, *J.Appl.Phys.*, **75**, (1994), 1319.

18) H.Muramatsu, E.Tamiya and I.Karube, *Anal.Chem.*, **60**, (1988), 2142.

19) H.B.Su, S.Chong and M.Thompson, *Langmuir*, **12**, (1996), 2247.

20) M.A.Cowen, S.L.Gilbert, M.Gonslaves, A.R.Hillman and S.J.Bruckenstein, *J.Chem.Soc.Far.Trans.*, **92**, (1996), 1079.

21) T.Okajima, H.Sakurai, N.Oyama, K.Toduka and T.Ohsaka, *Electrochim.Acta*, **38**, (1993), 747.

22) P.Curie and J.Curie, *C.R.Acad.Sci*, **91**, (1880), 294.

23) H.Helle, H.Valimaki and J.Lekkala, *Sens.Actuat.B*, **81**, (2002), 133.

24) J.W.L.R.Strutt, *The Theory of Sound*, Dover, New York, (1945).

25) G.Z.Sauerbrey, *Z.Phys.*, **155**, (1959), 206.

26) C.E.Reed, K.K.Kanazawa and J.H.Kaufman, *J.Appl.Phys.*, **68**, (1990), 1993.

27) C.S.Lu and O.Lewis, *J.Appl.Phys.*, **43**, (1972), 4385.

28) J.G.Miller and D.L.Bolef, *J.Appl.Phys.*, **39**, (1968), 4589.

29) D.M.Ward and E.J.Delawski, *Anal.Chem.*, **63**, (1991), 886.

30) C.Gabrelli, M.Keddam and R.Torresi, *J.Electrochem.Soc.*, **138**, (1991), 2657.

31) K.E.Heusler, A.Grzegorzewski, L.Jackel and J.Pietrucha, *Ber.Bunsen-Ges.Phys.Chem.*, **92**, (1992), 1218.

32) M.Thompson, C.L.Arthur and G.K.Dhalwali, *Anal.Chem.*, **58**, (1986), 1206.

33) L.V.Rajakovic, B.A.Cavicvlasak, V.Ghaemmaghami, K.M.R.Kallury, A.L.Kipling and M.Thompson, *Anal.Chem.*, **63**, (1991), 615.

34) M.Thompson, G.K.Dahlwali, C.L.Arthur and G.S.Calabrese, *IEEE Trans.Ultrason.Ferroelec.Freq.Contr.*, **34**, (1987), 127.

35) A.L.Kipling and M.Thompson, *Anal.Chem.*, **62**, (1990), 1514.

36) S.J.Martin, G.C.Frye, A.J.Ricco and S.D.Senturia, *Anal.Chem.*, **65**, (1993), 2910.

37) G.Christopoulos, *The Transmission-Line Modelling Method*, TLM, (1995).

38) V.E.Granstaff and S.J.Martin, *J.Appl.Phys.*,**75**, (1994), 1319.

39) C.Filiatre, G.Bardeche and M.Valentin, *Sens.Actuat.*, **44**, (1994), 137.

40) M.Valentin and C.Filiatre, *J.De Physique Iii*, **4**, (1994), 1305.

41) M.Schmid, E.Benes, W.Burger and V.Kravchenko, *IEEE Trans.Ultrason.Ferroelec.Freq.Cont.*,**38**, (1991), 199.

42) M.S.Yang and M.Thompson, *Anal.Chim.Acta.*, **282**, (1993), 505.

43) C.Lu and L.Czanderna, *Methods and Phenomena*, Elsevier, Amsterdam, (1994).

44) R.W.Cernosek, S.J.Martin, A.R.Hillman and H.L.Bandey, *IEEE Trans.Ultrason.Ferro.Freq.Cont.*, **45**, (1998), 1399.

45) S.J.Martin, G.C.Frye, A.J.Ricco and S.D.Senturia, *Anal.Chem.*,**65**, (1993), 2910.

46) F.M.White, *Viscous Fluid Flow*, McGraw-Hill, New York, (1994).

47) S.J.Martin and G.C.Frye, *IEEE Ultrason.Symp.Proc.*, New York, (1991), 393.

48) M.L.Williams, R.F.Landel and J.D.Ferry, *J.Am.Chem.Soc.*, **77**, (1955), 3701.

49) D.Pletcher, *A First Course in Electrode Processes*, The Electrochemical Society, Alresford Press, (1991).

50) A.C.Fisher, *Electrode Dynamics*, Oxford University Press, (1996).

Chapter 3
Experimental

3.1 Introduction

This section describes the instrumentation and methodologies used to collect and analyse data from the experiments presented in this thesis.

3.2 Amperometric Sensor Experimental Section

This section describes the equipment and chemicals used to record and interpret the cyclic voltammograms of the quaternary ammonium binaphthyl receptors studied in this thesis.

3.2.1 Chemicals And Analytes

3.2.1.1 Binaphthyls

All binaphthyl compounds used in electrochemical experiments as receptors were of the following general form (Figure 3.1). The various R and R' groups are listed in Table 3.1.

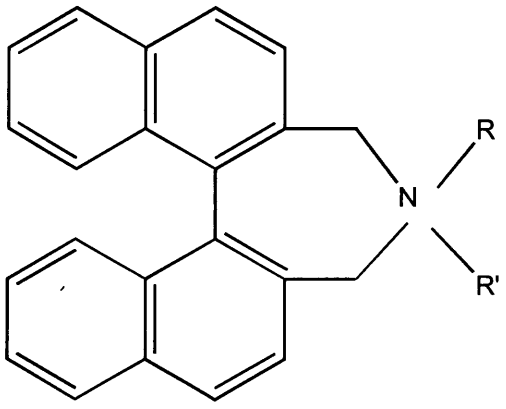

Figure 3.1 General form of receptors used in this work.

REFERENCE	R	R'
1	$-C_2H_4(OCH_2CH_2)_4$-R'	-
2	$-C_2H_4(OCH_2CH_2)_5$-R'	-
3	$-CH_3$	$-CH_3$
4	-^{i}pr	-^{i}pr
5	-cHex	-cHex
6	$-CH(CH_3)CH(C_6H_5)OH$	$-CH_3$
7	$-CH(CH_3)CH(C_6H_5)OH$	$-CH_3$
8	$-CH(CH_3)CH(C_6H_5)OH$	$-CH_3$
9	$-CH(CH_3)CH(C_6H_5)OH$	$-CH_3$
10	-^{i}pr	$-C_2H_4OH$
11	-Ph	$-C_2H_4OH$
12	$-CH_2Ph$	$-CH_3$
13	$-CH_2Ph$	$-C_2H_5$

Table 3.1 Receptors used in this work. The reader is referred to references 1-5 for their synthesis.

3.2.1.2 Some typical binaphthyls used

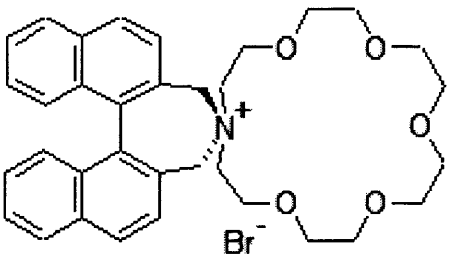

2

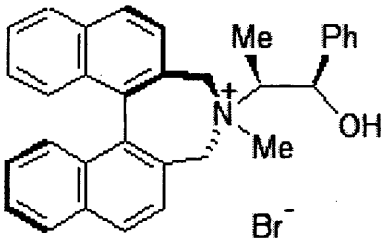

6

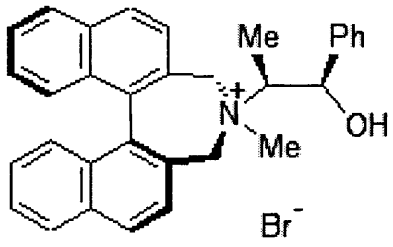

7

Figure 3.2 Typical binaphthyls used as receptors in this work.

The stereochemistry of receptors **6, 7, 8** and **9** is a little bit more complicated upon closer inspection of the binaphthyl receptors. As there are three chiral centres

involved in these molecules, they are defined in terms of the chiral centres from left to right as indicated in Figure 3.3.

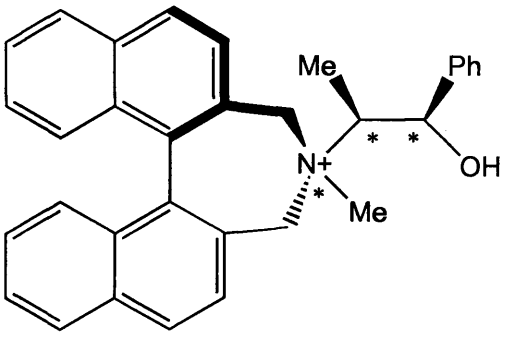

Figure 3.3 Stereochemistry of receptor ***6*** *showing the three chiral centres, from left to right on the diagram, (S,R,S).*

The remaining receptors have their stereochemistry around the three chiral carbon centres defined as follows; **7** (R,R,S), **8** (R,R,R) and **9** (S,R,R).

3.2.1.3 Analytes

All of the analytes used in electrochemical experiments are listed in Table 3.2. They were used as received.

ANALYTE	SOURCE	PURITY
Lithium perchlorate	Aldrich	>99%
Sodium perchlorate	Aldrich	>99%
D-(-)-Mandelic acid	Lancaster	>99%
L-(+)-Mandelic acid	Lancaster	>99%
D-(-)-Lactic acid	Fluka	>99%
L-(+)-Lactic acid	Fluka	>99%
Propionic acid	Avocado	99%
Benzoic acid	Scientific Chemical Supplies	99%
p-toluenesulphonic acid	Lancaster	>98%
tetraethylammonium p-toluenesulfonate	Fluka	>99%

Table 3.2 Analytes used in this work.

3.2.1.4 Solvents

All of the solvents used in electrochemical experiments are listed in Table 3.3. They were used without further purification.

SOLVENT	SOURCE	PURITY
Acetonitrile	Fisher	>99.98%
Tetraethylammonium hydroxide	Lancaster	50-60% aqueous solution
Propylene Carbonate	Fisher	>99%

Table 3.3 Solvents used in this work.

3.2.2 Instrumentation

All electrochemical measurements were carried out using a PGSTAT 20 potentiostat (Ecochemie, Holland). The working electrode (WE) was a 10 μm diameter gold disc sealed in glass. The counter electrode (CE) was a Pt wire and the potentials were quoted versus a saturated $Ag/AgBF_4$ reference electrode (RE). All the cyclic voltammograms were obtained at 25°C under triple sweep conditions, between +0.3V and +1.5V at a scan rate of 10 mVs^{-1}.

3.2.2.1 Diagram of Cell

The experimental set-up, as outlined in Section 3.2.2, is shown diagrammatically in Figure 3.4. WE, RE and CE represent the working, reference and counter electrodes respectively.

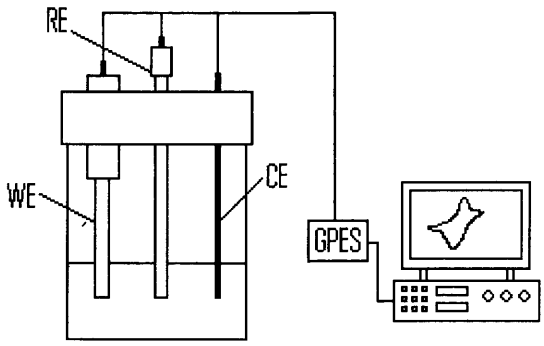

Figure 3.4 Diagram of cell.

3.2.2.2 Experimental Considerations

Quaternary ammonium binaphthyl compounds are normally incredibly stable species in solution with their respective anion or cation radical lifetimes in the order of minutes. However one main problem when dealing with the electrochemical reduction of binaphthyl compounds is their ability to react with any unwanted oxygen that may be present in the electrolyte solution or electrochemical cell. To discourage the binaphthyls from doing this and so to reduce the chance of any secondary reactions taking place, the solutions were purged with nitrogen gas for a period of 1 hour prior to taking electrochemical measurements.

3.2.3 Characterisation

In order to gain some insight into the interactions taking place between analyte and quaternary ammonium binaphthyl receptor, molecular modelling calculations were performed and ^{1}H-NMR spectra were recorded to enable the discussion of this phenomenon. These procedures are outlined below.

3.2.3.1 Molecular Modelling

Ab initio calculations were carried out using PC Spartan Pro[6]. The equilibrium geometry, including relevant bond angles of the binaphthyl receptors, were calculated using the Hartree-Fock Self Consistent Field (HF-SCF) method utilising a STO-3G basis set for each atom[7]. While this method may not produce exact minimum energy conformations the '3D cartoons' are useful for comparative analysis. Molecular modelling calculations were also able to highlight possible areas of analyte-receptor binding from electron density maps. These are discussed in further detail in Chapter 4.

3.2.3.2 ^{1}H-NMR Spectroscopy

All ^{1}H-NMR spectra were recorded on a Bruker DRX 400 spectrometer (400.13 MHz) using a 5 mm bore inverse probehead (TXI). Samples were dissolved in CD_3CN (Goss Scientific) and internally referenced to TMS (0 ppm). 1D spectra were

recorded with 32 K data points over a 5995 Hz (14.9 ppm) window using a 30-degree acquisition pulse (90 degree pulse 9.6 μs). 16 transients were collected using a 1.5 s recycle delay added to the 2.73 s acquisition time. Data were processed using exponential multiplication (line broadening factor of 0.2 Hz). 2D phase-sensitive NOESY spectra were recorded using the standard Bruker pulse program (noesytp). 256 blocks of 1 K data points covering a 4401 Hz (11 ppm) range in F2 were recorded with a recycle delay of 5 s, a mixing time of 850 ms and 16 transients per block. Data in F1 was zero-filled to 1K and both dimensions were processed using sine-bell squared window function shifted by $\pi/2$.

3.3 TSM Resonator Experimental Section

This section describes the instrumentation and methodologies used to record and interpret the crystal impedance spectra of the polymer wax films.

3.3.1 Equipment

3.3.1.1 Instrumentation

Crystal impedance spectra were recorded using a Hewlett-Packard HP-8751A network analyser, connected *via* a 50 Ω coaxial cable to a HP-87512A transmission/reflection unit. The frequency dependent ratio of the reflected to incident signal is denoted as the 'scattering parameter', S_{11}. S_{11} is a complex quantity that contains magnitude ratio and phase relation information between the incident and reflected signals. The input impedance is found from S_{11} using the following relationship:

$$Z_S(f) = Z_0\left(\frac{1+S_{11}(f)}{1-S_{11}(f)}\right) \tag{3.1}$$

Where Z_0 is the characteristic impedance of the system (typically around 50 Ω).

3.3.1.2 Cell Set Up

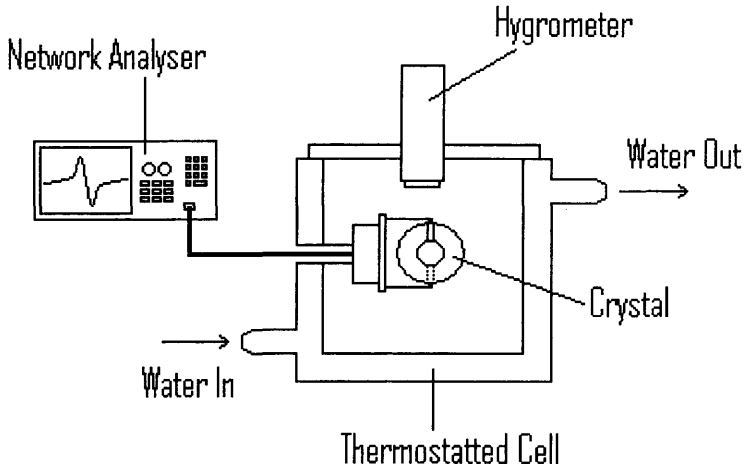

Figure 3.5 Schematic of experimental set up to record crystal impedance spectra.

3.3.1.3 Temperature Control

The thermostatted electrochemical cell was maintained at desired temperatures using a water jacket, through which water was pumped using a Techne Tempunit™ (TU-16D). In order to record lower temperatures, the bathing solution was changed to ethylene glycol. The temperature at the crystal surface was confirmed using an HI-8564 thermohygrometer (Hanna Instruments, UK) fitted to the PTFE roof of the cell and held as close to the crystal surface as possible.

3.3.2 Materials

3.3.2.1 Crystals

The crystals used were polished non-bonded 10 MHz AT-cut quartz crystals (International Crystal Manufacturing, USA) coated with Au electrodes with piezoelectrically and electrochemically active areas of 0.21 cm^2 and 0.23 cm^2, respectively. The use of the polished crystals minimized surface roughness effects. Crystals were mounted on external connections and connected to the Network Analyser in order for impedance measurements to be recorded.

3.3.2.2 Wax Sections

All of the waxes and components of waxes used in this study are listed in Table 3.4. They were all used as received. Wax sections were prepared in the manner as described below.

NAME	FORMULA	R.M.M	MP/^{O}C	DENSITY
Paraffin wax	$CH_3(CH_2)_{24}CH_3$	366.718	62-64	0.94
Behenic acid	$CH_3(CH_2)_{20}CO_2H$	340.60	79-80	0.82
Docosanol	$CH_3(CH_2)_{21}OH$	326.61	69-71	0.81
Octadecyl docosanoate	$CH_3(CH_2)_{20}CO_2(CH_2)_{17}CH_3$	592.998	66-74	0.86

Table 3.4 Waxes and components of waxes used in this study.

A suitable mould is prepared based on the size of the block of wax or wax component required. A rubber bung is typically used as the receptor and the inside of the lining of the bung is covered with aluminium foil. The wax is warmed and poured into the receptor where it is allowed to cool and set. The block can then be removed from the bung/receptor with ease allowing sections of the wax to be cut to the required thickness. A microtome is used to cut 6 μm sections of wax directly into a thermostatted water-bath. The water-bath is held at a temperature 1-2 degrees lower than the melting point of the wax allowing the samples to be kept in an environment where they remain malleable. The wax sections can then be "floated" onto a quartz crystal and removed from the water-bath, excess water can then be removed from the crystal surface with the use of a Pasteur pipette. This has the effect of drawing the wax section out across the crystal as water is removed and enables the wax section to adhere to the quartz crystal ready for use.

3.3.2.3 Chemicals

Table 3.5 provides a list of all the surfactants supplied by Dow Agrosciences for use within this study. They did not require any further purification and were all used as received.

SURFACTANT	TYPE	SOURCE	PURITY
Water	Neutral	n/a	>99%
Agnique	Anionic	Dow Agrosciences	>99%
Solvesso	Cationic	Dow Agrosciences	>99%

Table 3.5 Chemical surfactants used in this study.

Agnique is an alcohol ethoxylated surfactant that is used to combat mosquitoes. Once sprayed onto the surface of standing water habitats it interrupts the critical air/water interface in the mosquito's larval and pupal development cycle causing them to drown. Solvesso is a heavy aromatic fluid that plays many roles in agricultural formulations. The most widespread use is in emulsifiable concentrate formulations, where the fluid dissolves the active ingredient and acts as a carrier for it and other formulation components, taking them directly to the surface of plants and crops. Water meanwhile has been used as a useful comparison in each of the experiments.

3.3.3 Data Acquisition

In order to record spectra of higher temporal resolution, network analyser data acquisition was controlled using an IBM compatible personal computer, running HP-VEE, which was linked to the analyser using an HB-IB interface card (HP 82341C) and cable (HP 10833C). This program was capable of recording fundamental resonance spectra at specific time intervals, which permitted the investigation of the impedance spectra over a period of time.

3.3.3.1 Spectra Interpretation

A fitting program using the Solver function of Excel was run on a PC to interpret crystal impedance spectra. The program approximated the experimentally determined crystal impedance responses by comparing them to theoretical crystal impedance responses. A diagrammatical representation of the outline of the fitting program is shown below in Figure 3.6. By selecting initial input parameters (f_0, R, L and C_0) that are close estimates to the actual values, a theoretical impedance is obtained and the difference in experimental and theoretical data values then calculated. The difference between the two is expressed in terms of a root mean square (RMS) error. The fitting program can then be allowed to vary the selected input parameters until the RMS

error reaches an acceptable level. This can be shown qualitatively when the experimental and theoretical impedance plots appear almost identical to each other and the RMS error effectively reduces to zero. Upon reaching the agreed RMS error, the variable parameters are determined to an appropriate level of precision to allow the calculation of shear modulus parameters. The shear modulus values are determined by selecting an appropriate model from Table 2.1 that matches the physical state of the materials attached to the surface of the resonator.

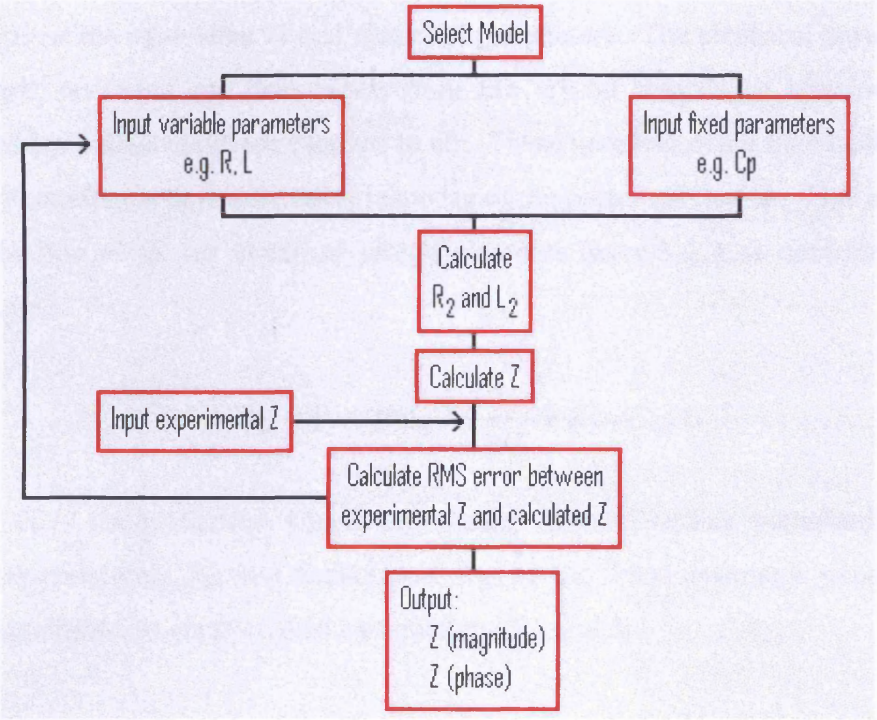

Figure 3.6 Flowchart for the fitting of data to obtain shear modulus parameters.

For example, if the flowchart in Figure 3.6 is followed for the case of a Finite Viscoelastic Film (Model 5 from section 2.3.4 in the Theory Chapter), then the shear modulus can be determined as follows. Values for the variable parameters (*e.g.* f_0, R, L and C_0), that are of similar magnitude to the experimentally obtained values are input into the working model along with any fixed parameters (*e.g.* C_P). In this case, typical values for the variable parameters already mentioned are 9.997 MHz, 8 kΩ, 7 mH, and 0.00553 nF respectively. The experimentally determined value of Z can now be obtained.

The solver function of Excel can now be used to minimize the RMS error between the experimentally and theoretically determined values of Z until the error

has reached zero. The extraction of the electrical parameters can now be achieved and this is discussed in detail below. In all cases, the correlation between the experimental and theoretical values was in excellent agreement, with the RMS error reducing to zero very quickly.

3.3.3.2 Extraction Of Electrical Parameters

The different surface perturbations of the TSM resonator can be compared by extraction of the equivalent circuit electrical parameters. The electrical parameters of the quartz resonator are determined from the crystal impedance response of the mounted but uncoated device exposed to air. These parameters are then held constant while attempting to fit the electrical response of the perturbed device. This allows the determination of all the electrical circuit elements (except Z_e) as described by the following:

$$Z_m = R_1 + j\omega L_1 + \frac{1}{j\omega C_1} + Z_e \tag{3.2}$$

Where Z_e is the additional impedance arising from a surface perturbation. The electrical resistance, R_2, and inductance, L_2, of the TSM resonator exposed to a surface perturbation are described by equations 3.3 and 3.4.

$$R_2 = \frac{N\pi}{4K^2\omega_s C_o}\frac{\mathrm{Re}(Z_s)}{Z_q} \tag{3.3}$$

$$L_2 = \frac{N\pi}{4K^2\omega_s C_o}\frac{\mathrm{Im}(Z_s)}{Z_q} \tag{3.4}$$

In a Butterworth Van-Dyke model[8], TSM resonators can be exposed to a combination of physical perturbations. In each of these cases it is desirable to distinguish between electrical impedances arising from each physical component.

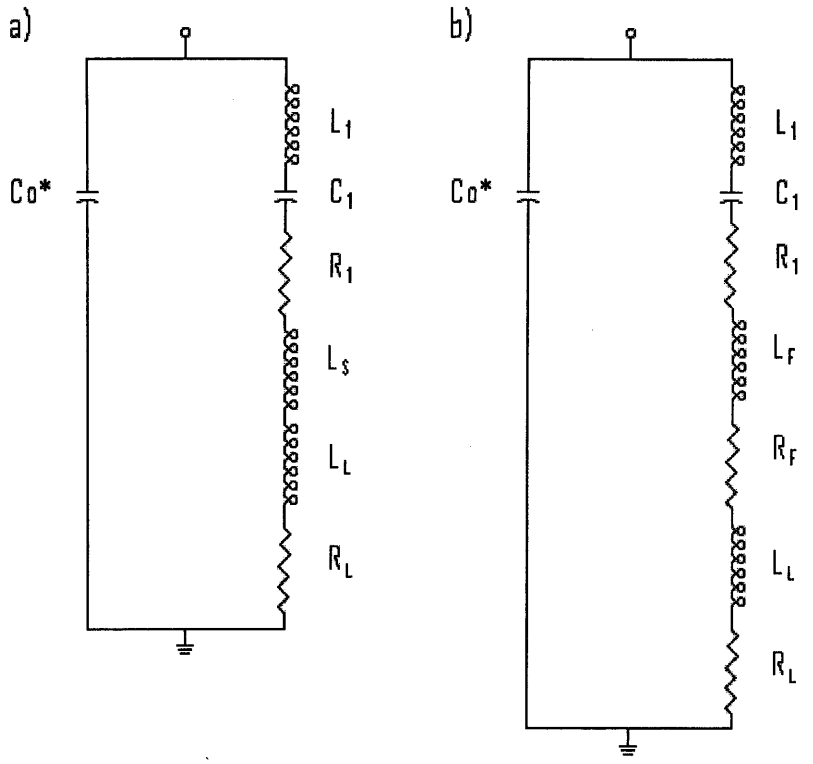

Figure 3.7 Modified Butterworth Van-Dyke model for a TSM resonator with the following surface perturbations; a) a rigid layer and contacting liquid and b) a non-rigid mass layer and contacting liquid.

A modified Butterworth-Van Dyke model[9] that approximates the electrical response of a TSM resonator coated with a rigid mass layer immersed in a liquid is shown in Figure 3.7.

The electrical parameters, R_L and L_L, arising from the presence of the liquid can be extracted by comparing the responses of the uncoated crystal in air to that of the crystal exposed to the liquid. The resonator can then be coated with a rigid layer and immersed in the liquid. Any additional responses arising this time are due solely to the rigid film and hence L_S can be extracted. L_f and R_f represent the electrical inductance and resistance arising from a contacting liquid and L_L and R_L are the electrical inductance and resistance arising from a viscoelastic layer. These electrical components for the film and solution are additive, *i.e.* $R_2 = R_f + R_L$ and $L_2 = L_f + L_L$ and they define the electrical impedance (Z_e). This is represented by Figure 3.6b. From the extracted electrical parameters it is useful to note that a change in ωL_2 is inversely proportional to a frequency shift and R_2 is proportional to the maximum impedance.

3.3.3.3 Extraction Of Physical Parameters

Physical parameters are extracted from crystal impedance spectra using the models described in section 2.3. The variable physical parameters for each model are listed in Table 2.1. Crystal parameters were obtained from the response of a blank, uncoated crystal in air. Shear modulus parameters can then be extracted from the crystal impedance spectra with accuracy.

3.3.3.4 Uniqueness Of Fit

In order to reduce the number of unknown physical parameters in a system, it is useful to have some idea of the physical/chemical properties of the system under investigation. For example, by knowing the thickness of the polymer film attached to the surface of the electrode, h_f, reduces the complexity of the equations used in the fitting procedure. As well as making the calculations easier to carry out, it also eliminates the number of mathematically feasible, yet physically impossible, solutions that may present themselves. This allows for unique mathematical solutions to be obtained with relative ease.

3.4 References

1) A.P.Abbott, C.S.M.Chung, I.G.Stara, I.Stary and P.Kocovsky, *Chem.Commun.*, (1999), 641.
2) A.P.Abbott, G.Barker, G.R.Lonergan, A.J.Walter and P.Kocovsky, *The Analyst,* **126**, (2001), 1892.
3) A.P.Abbott, G.W.Barker, D.L.Davies, G.A.Griffths, A.J.Walter and P.Kocovsky, *Anal.Chem.*, **74**, (2002), 4002.
4) N.Marigot and J.P.Mazaleyrat, *Synthesis*, (1985), 317.
5) A.P.Abbott, G.W.Barker, A.J.Walter and P.Kocovsky, *The Analyst,* **128**, (2003), 245.
6) Spartan Pro, Wavefunction Inc., Irvine, CA, USA.
7) T.Clark, *A Handbook of Computational Chemistry*, Wiley, New York, (1986).

8) H.L.Bandey, A.R.Hillman, M.J.Brown and S.J.Martin, *Faraday Discussions*, **107**, (1997), 105.

9) S.J.Martin, V.E.Granstaff and G.C.Frye, *Anal.Chem.*, **63**, (1991), 2272.

Chapter 4
Quaternary Ammonium Binaphthyl Salts As Receptors For Use In Amperometric Sensors

4.1 Introduction

The recent work of Abbott *et al*[1] highlights the use of azacrown ether salts as possible bulky macrocyclic receptors for alkali metal ions. The stability and hence the reversibility of the electrochemical response of the receptors is discussed in terms of their molecular structure, with the ability of the azacrown salts to detect Group 1 metal cations ascribed to the strain imparted in the cyclic ammonium ring. A common approach to electrochemical receptor design is to combine a binding group in close proximity to a redox active centre[2-3]. The subsequent binding of an analyte with a host receptor affects the electrochemical response of the redox process and hence an analytical signal can be obtained[4]. Two types of responses are possible; a potentiometric response where the thermodynamics of the redox process are changed upon analyte binding, or an amperometric response where analyte binding precludes or enhances electron transfer.

Discovered 25 years ago, crown ethers have found many applications[5-6]. It is well known that they can bind to Group 1 and Group 2 metal cations with the selectivity shown towards these cations based on the compatibility of the metal cation radius and the size of the crown ether macrocyclic cavity. This effect has been exploited in the construction of ion-selective electrodes[7-14]. The application of transition metal polypyridyl systems to chemical sensor technology is one that has received limited attention over the last few years[15-17], but has been investigated by Beer *et al*[18-24]and looks to be one of the more exciting prospects for the future in terms of sensor design. Beer *et al* looked at the cyclic voltammograms of benzo-15-crown-5-ether-vinyl-bipyridyl ligands and their ruthenium(II)complexes in acetonitrile. It was found that these receptors were sensitive to the supporting electrolyte, being more difficult to electrooxidize upon binding to Na^+ or Mg^{2+} cations. Following on from earlier work with complexes of the aryl containing 4,4'-distyrl-2,2'-bipyridine (DSB)[25], 4,4'-bis (p-methylstyryl)-2,2'-bipyridine (MeDSB) and 4'-methoxy-4-stilbazole ligands[26], it was anticipated that the sequential potential cycling of the

solutions of the ruthenium complexes mentioned above would activate the vinylic linkages and initiate electropolymerisation. Unfortunately, initial results for the recognition of Na^+ and Mg^{2+} cations by the benzo-15-crown-5-ether containing surface modified electrodes were disappointing. Although it was apparent that binding of Na^+ and Mg^{2+} cations produced shifts in the $Ru^{II/III}$ redox potentials for some of the ligands investigated, not all of the cyclic voltammograms produced gave the same magnitude in shift. With one example it was not possible to use the receptors as possible sensors for Group 1 and 2 cations due to the electroreduction of the metal cations at relatively positive potentials in acetonitrile.

One of the few papers found in the literature of which comparisons can be drawn to the current work under investigation, in terms of matching the macrocyclic receptor in appearance and the procedure in experimental protocol, is one written by Belloncle *et al*[27]. Although the binaphthyl crown ether is missing the azacrown linkage unit, the crown moiety is still joined to the binaphthyl molecules at the 2,2'-substituted positions. The significant difference however is that this monomeric unit is electropolymerized to produce a conducting polymer for the chiral recognition of analytes. The authors also managed to prove the formation of the perylene radical leading to the production of disubstituted perylenes, a process for which very few examples have been reported[28].

The binaphthyl salts used by Abbott *et al* give rise to an amperometric response. The azacrown ether was derivatised with a quaternary ammonium binaphthyl salt unit that proved to be electroactive, with the radical anion generated upon electroreduction being stable in the order of minutes. The binding of alkali metal cations to the crown ether group precludes the binaphthyl cation being reduced and so a decrease in reduction current was observed. It had been previously postulated that the presence of the quaternary ammonium group stabilized the radical intermediate during formation, however it now turns out that the group actually makes the formation of the radical intermediate thermodynamically more difficult. Evidence for this comes from several sources. First, a look at the bond angles around the naphthyl moieties of the neutral and radical species reveals that by constraining the movement of the groups *via* a quaternary ammonium group will result in a decrease of approximately 10° in the dihedral angle. This is enough to make the formation of the cation radical thermodynamically less favourable, in turn shifting the reduction potential to much more negative potentials. Secondly, from molecular modelling

calculations[29], a change in the conformation of the molecule when the binaphthyl salt is reduced is clearly evident which causes a change in the distance between the benzylic carbons from 3.74Å in the neutral molecule to 3.95Å in the radical species.

Work by Parker *et al*[30-32] on cyclodextrins incorporated into polymer membranes shows that although they act as chiral potentiometric devices, they are relatively insensitive to a range of analytes producing a potential shift of only 20-30mV when moving from a racemic mixture to an enantiomerically pure compound. The amperometric quaternary ammonium binaphthyl salts by comparison are much more sensitive to slight changes in concentration of lithium ions, this being one of the themes explored herein.

4.2 Results

4.2.1 Quaternary Ammonium Binaphthyl Salts

Quaternary ammonium binaphthyl salts (QABS) undergo a quasi-reversible one-electron reduction in acetonitrile. Unfortunately the reductive current is difficult to use as an analytical signal because of a chemical reaction of the radical with dissolved oxygen and the tendency for adsorption of the receptor onto the electrode surface. All binaphthyl compounds used in electrochemical experiments were receptors of the following general form (Figure 4.1).

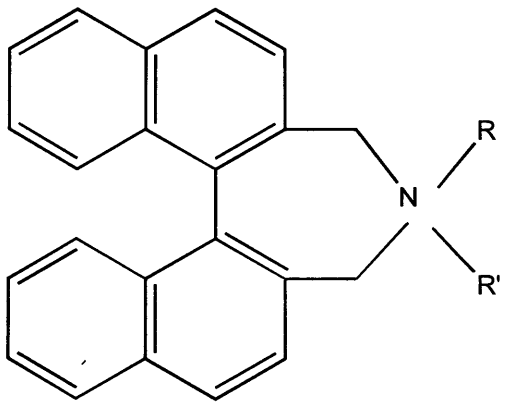

Figure 4.1 General form of receptors used in this work.

The various R and R' groups are listed in Table 4.1.

REFERENCE	R	R'
1	$-C_2H_4(OCH_2CH_2)_4$-R'	-
2	$-C_2H_4(OCH_2CH_2)_5$-R'	-
3	$-CH_3$	$-CH_3$
4	-^{i}pr	-^{i}pr
5	-cHex	-cHex
6	$-CH(CH_3)CH(C_6H_5)OH$	$-CH_3$
7	$-CH(CH_3)CH(C_6H_5)OH$	$-CH_3$
8	$-CH(CH_3)CH(C_6H_5)OH$	$-CH_3$
9	$-CH(CH_3)CH(C_6H_5)OH$	$-CH_3$
10	-^{i}pr	$-C_2H_4OH$
11	-Ph	$-C_2H_4OH$
12	$-CH_2Ph$	$-CH_3$
13	$-CH_2Ph$	$-C_2H_5$

Table 4.1 Receptors used in this work.

The stereochemistry of receptors **6, 7 8** and **9** is a little bit more complicated upon closer inspection of the binaphthyl receptors. As there are three chiral centres involved in these molecules, they are defined in terms of the chiral centres from left to right as indicated in Figure 4.2.

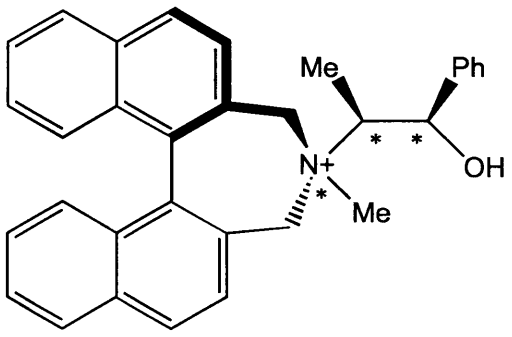

*Figure 4.2 Stereochemistry of receptor **6** showing the three chiral centres, from left to right on the diagram, (S,R,S).*

The remaining receptors have their stereochemistry around the three chiral carbon centres defined as follows; **7** (R,R,S), **8** (R,R,R) and **9** (S,R,R).

The $E_{1/2}$ for the reduction of the ammonium salt is negative which suggests that far from stabilizing the radical, the presence of the quaternary ammonium group actually makes the formation of the radical thermodynamically more difficult. This idea is explored in more detail in section 4.2.1.2 although essentially constraining the movement of the benzylic carbons by joining them *via* a quaternary ammonium group increases the electrochemical reversibility of the receptor and enhances its sensitivity towards a given analyte *e.g.* Li^+. The oxidation of the receptor circumvents these difficulties and yields an analytical signal, which is sensitive to a variety of analytes. Acetonitrile was used as the solvent in each of the experiments for several reasons. Firstly, all of the QABS dissolve readily into the acetonitrile and secondly, acetonitrile prevents unwanted oxidation of the receptors which would occur in other solvents *e.g.* water. A table detailing all of the binaphthyl receptors is shown in Table 4.1 for reference.

4.2.1.1 Oxidation Of Quaternary Ammonium Binaphthyl Salts

Figure 4.3 shows the electrochemical response of **1** in acetonitrile on a gold electrode.

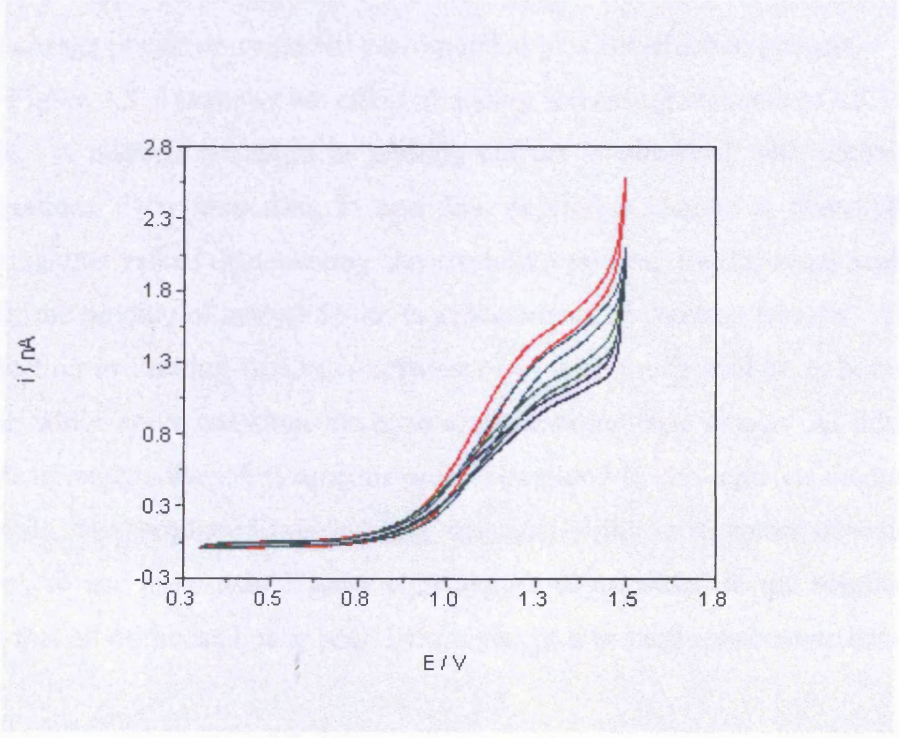

*Figure 4.3 Cyclic voltammograms for the oxidation of **1** at a gold electrode following the addition of 0 (---), 0.9 (---), 3.3 (---) and 5 (---) mole equivalents of $LiClO_4$. Potentials quoted vs. $Ag/AgBF_4$ reference electrode.*

A one-electron process is observed at $E_{1/2}$ = +1.02V. In contrast to the reduction process previously reported on graphite[33-34] where subsequent scans are totally irreproducible due to adsorption, the electrochemical response for the oxidation process does not change with repetitive cycling. The current at *c.a.* +1.5V is thought to originate from traces of residual water in the solution. There was also no change in the electrochemical response for the oxidative process when the solution was deoxygenated. The process is only quasi reversible and it is thought that the radical formed reacts slowly with traces of water to cleave the CH_2-N^+ bond. The electro-oxidation is most likely to be a one-electron process since the difference between the first and second oxidation process for 1,1'-binaphthyl was previously found to be in the order of 280 mV. Previous work[28] has also shown that the cyclisation of binaphthyls to form perylenes is also possible following a two-electron process. The species thus formed are redox active with redox peaks at *c.a.* +0.4 and +0.8 V and no such signals were observed in this work. The two-electron process is also highly unlikely for the QABS since the strain imparted by the CH_2-N^+-CH_2 bridge would make cyclisation sterically impossible without cleavage of the cyclic system. Exhaustive electrolysis using a gold electrode (area = 1.2 cm^2) at +1.35 V confirmed that the charge passed on oxidation corresponded to a one-electron process.

Figure 4.3 also shows the effect of adding increasing amounts of $LiClO_4$ to the solution. A marked reduction in limiting current is observed with increasing Li^+ concentration. It is interesting to note that negligible change is observed in $E_{1/2}$ suggesting that rather than making the oxidative process thermodynamically more difficult; the binding of analyte to the receptor precludes electron transfer. Therefore the reduction in limiting current is a measure of how much analyte is bound to the receptor, which could constitute the basis of an amperometric sensor. As lithium ions are more strongly solvated in aqueous media compared to non-aqueous media such as acetonitrile, they produce lower binding constants with the receptors in water. It is necessary to use more than 1 mole equivalent analyte added to the solution. This ensures that all of the analyte is bound to the receptor to produce accurate data.

4.2.1.2 Quaternary Ammonium Binaphthyl Salts As Amperometric Lithium Sensors

Figure 4.4 shows the limiting current ($I_p/I_{(lim)}$) as a function of the number of mole equivalents of lithium added to the solution. The current has been normalized to the current without the addition of analyte to eliminate any fluctuations caused by changes in concentration and also for ease of comparison. This method of presenting data is used consistently throughout this chapter. A roughly linear response is obtained showing that this guest-host interaction could form the basis of an electroanalytical device. The decrease in current with analyte concentration was less marked than that observed with the reduced QABS[1,35] suggesting that the binding constant is reduced. This would, however, be expected since the concentration of cations in the double layer close to a positively charged electrode will be less than that close to a highly negatively charged electrode.

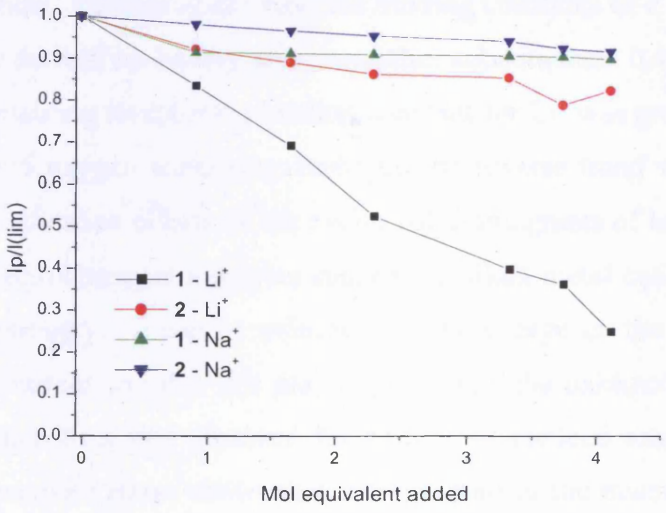

*Figure 4.4 Normalised limiting current data for receptors **1** and **2** following the addition of 0, 0.9, 1.7, 2.3, 3.3, 3.8 and 4.1 mole equivalents of $LiClO_4$ and $NaClO_4$.*

Furthermore the charge close to the binding site on the oxidized QABS will be more positive than that on the reduced species, decreasing the binding constant of the analyte with the host. If, as previously postulated, the receptor works by precluding the electron transfer when the analyte is bound, then Figure 4.4 suggests that the binding constant for the oxidized species is of the order of 0.2 which is a factor of 5

lower than that for the reduced QABS[1]. Earlier work has shown that the size of the azacrown ether moieties affects its selectivity towards cations in solution[36]. Figure 4.4 also shows the limiting current as a function of the number of mole equivalents of Li^+ added to a solution of the 5 oxygen containing receptor, **2**. Despite the cyclic voltammogram for **2** being practically identical to **1** the effect of Li^+ on the limiting current is less significant. Any competing effect from the presence of the bromide ion in the voltammetry experiments was ruled out on the basis of the greater binding affinity for Li over Br by the azacrown moiety. This was confirmed by looking at the background scan of binaphthyl receptor without any Li present.

This suggests that either the binding constant of Li^+ with **2** is less than with **1** and/or that the complex produced imparts less strain on the quaternary ammonium group and hence the radical intermediate. The same experiments were repeated using receptors **1** and **2** with $NaBF_4$. Figure 4.2 shows that the response for both receptors with Na^+ is similar. While no binding constant data exists for alkali metal ions with ammonium crown ethers it is logical to presume that the same trends will be observed as with azacrown ethers. Pearson *et al*[37] reported binding constants of *c.a.* 10^4 for two p-phenylenediamine derivatives having azacrown ether substituents. It was found that for the 4 oxygen containing receptor the binding constant for Li^+ was greater than that for Na^+, but for the 5 oxygen containing analogue the reverse trend was observed. Gokel *et al*[38-40] studied cation effects on the cyclic voltammograms of lariat ethers. It was reported that electrochemical reduction caused the alkali metal cation to bind up to 10^6 times more strongly. It can be inferred that the charge on the receptor will affect the binding constant and that this may explain why the oxidized cation has a lower binding constant than that observed for neutral or reduced azacrown ethers. The literature on azacrown ethers shows that the structure of the macrocycle affects cation binding and it is clear that irrespective of the charge on the receptor there should be markedly different binding constants for the two receptors studied here with Li^+ and Na^+. An explanation of the current trend observed could be that even though the ions bind to the receptor their effect on the geometry of the binaphthyl moiety and hence the electrochemistry of the receptor will differ.

4.2.1.3 Quaternary Ammonium Binaphthyl Salts as Alkali metal receptors

Molecular modelling calculations were carried out to observe the change in the dihedral angle between naphthyl moieties upon binding to alkali metal ions. Figure 4.5 shows that when Li^+ binds to **1** a conformational change occurs and the dihedral angle between the two naphthalene rings decreases.

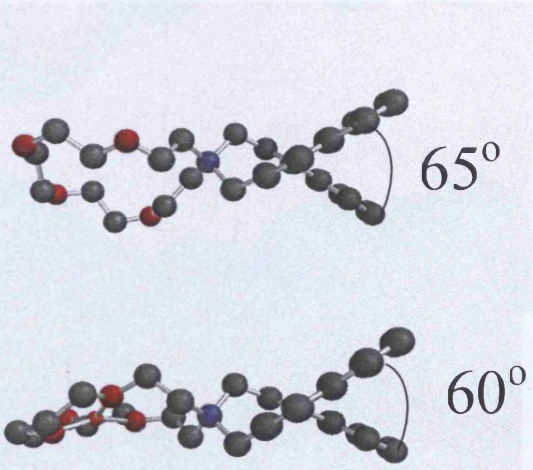

*Figure 4.5 Conformational change observed for receptor **1** upon binding with Li^+ (hydrogen's omitted for clarity).*

Table 4.2 shows the dihedral angles between the naphthyl moieties for receptors **1** and **2** with and without alkali metal cations bound. These results show that a significant change in the equilibrium geometry is only observed when Li^+ binds to **1** and that this correlates well with the data in Figure 4.5.

RECEPTOR	**DIHEDRAL ANGLE / °**		
	No analyte	Li^+	Na^+
1	65.0	59.7	66.3
2	64.6	65.2	66.2

*Table 4.2 Dihedral angles of receptors **1** and **2** with and without Li^+ and Na^+.*

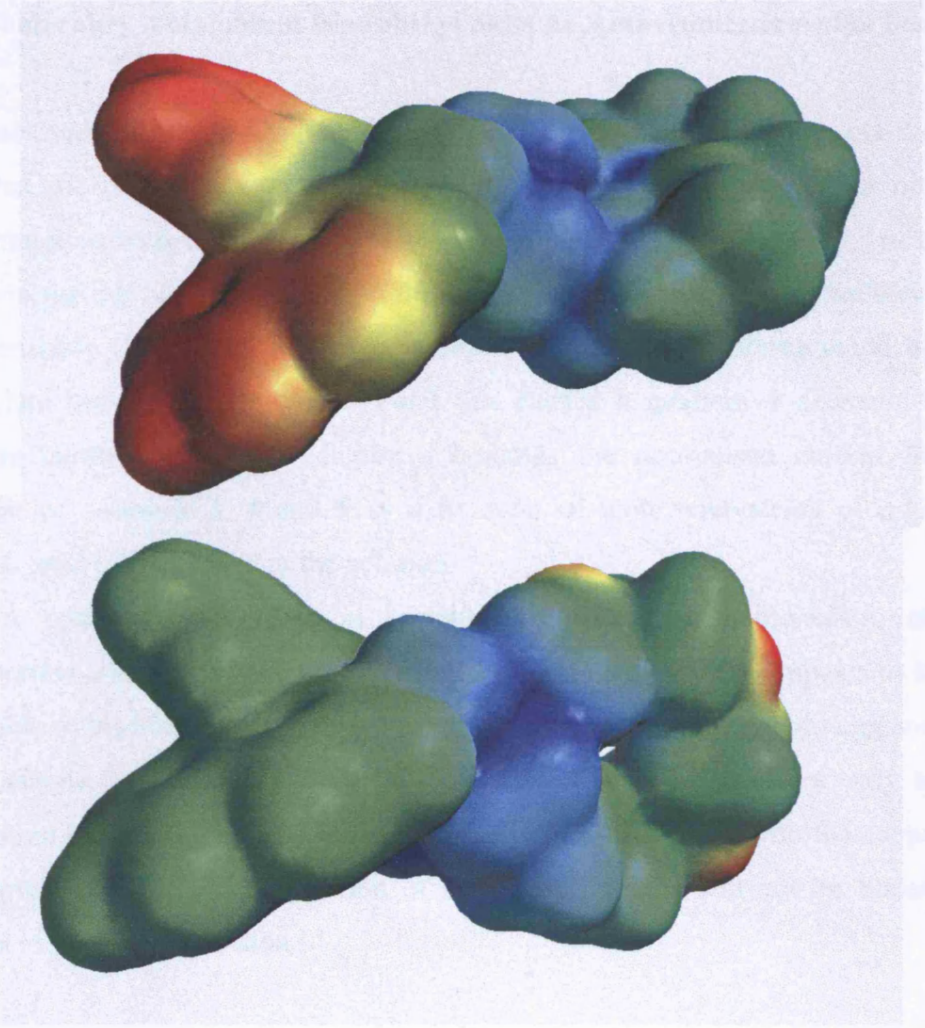

*Figure 4.6 Electron density models for receptor **1** with bound (top) and unbound (bottom) lithium.*

Similar geometry changes in the dihedral angle are not observed for the other receptor-cation combinations and could explain their lack of electrochemical sensitivity to cation binding. This suggests that the receptor only exhibits a significant change in electrochemical response when analyte binding results in a significant change in the structural conformation. The electron density models shown in Figure 4.4 confirm the idea that significant changes in the electrochemical response are observed only when analyte binding causes changes in structural conformation. The blue areas of the contour maps represent the electropositive regions of the surface. This could limit the applicability of this type of receptor, but increase its selectivity towards a given analyte.

4.2.2 Quaternary Ammonium Binaphthyl Salts As Amperometric Anion Sensors

It has been seen that the specific binding of an analyte to a receptor site is not the only factor that affects the redox properties of QABS. The quaternary ammonium nitrogen itself strongly affects the conformation of the reduced binaphthyl moiety. In theory strong ion pairing of a bulky anion to the cation could also preclude its reduction. It was previously shown that quaternary ammonium binaphthyl cations could bind to carboxylate and sulphonate anions[35] and this caused a qualitative decrease in the reduction current of QABS. Figure 4.7 shows the normalised current for the oxidation of receptors **3**, **4** and **5** as a function of mole equivalents of p-toluene sulphonic acid (pTos) added to the solution.

A quantitative decrease in current is observed with increasing analyte concentration although the response is not linear. The receptor also appears to be less susceptible to the binding of anions. This may be expected since the binding constant of the analyte (in the anionic form) with the receptor is affected not only by the dissociation of the acid but also by the association of the analyte with the supporting electrolyte. Hence the concentration of dissociated anions will not be linear as a function of pTos concentration.

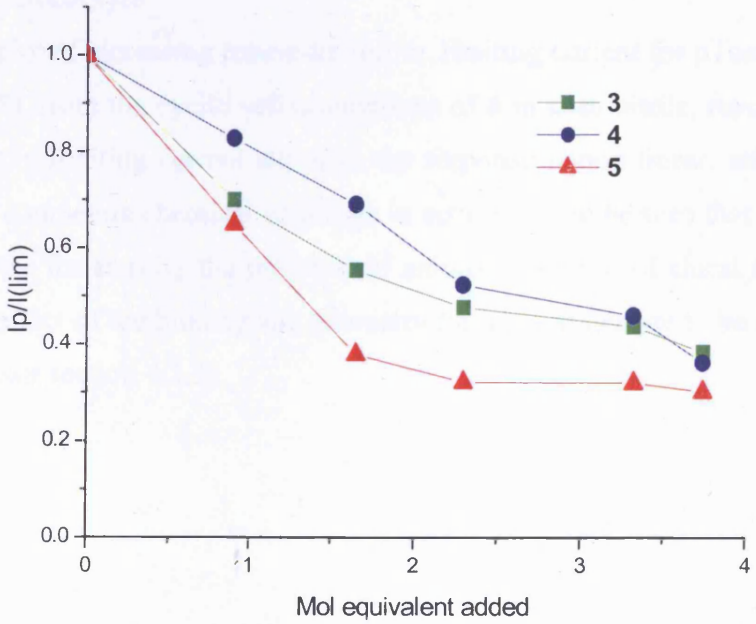

*Figure 4.7 Normalised limiting current data for receptors **3**, **4** and **5** following the addition of 0, 0.9, 1.7, 2.3, 3.3 and 3.8 mole equivalents of pTos.*

To determine if pTos binds to the azacrown ether or the ammonium moiety, the same experiment was carried out using receptor **4** in place of receptor **3**. The cyclic voltammogram for **4** is almost identical to that for **3** in the absence of analyte. Figure 4.5 also shows that these two receptors have a similar electrochemical response when the analyte is added to the solution and hence it can be concluded that for pTos charge-charge interactions must dominate binding.

The basic architecture of the quaternary ammonium salts is relatively easy to modify and the dicyclohexyl derivative, **5**, was made and tested to determine whether the size of the pendent groups on the quaternary ammonium group had any effect on the sensitivity of the receptor. Figure 4.7 shows that the electrochemical response for receptor **5** is more sensitive to the presence of pTos than either of the other two receptors. Given that the dihedral angles of the three receptors used in this work are **3** = 64.8°, **4** = 64.7° and **5** = 55.7° this would seem to suggest that the greater the strain imparted on the quaternary ammonium group the more the receptor is affected by the interaction with the analyte. It can then be concluded that the bulkier substituents will increase the sensitivity of the receptor for a given anionic analyte. pTos dissociates very well, a useful property since binding with the receptor depends on the dissociation of the acid in solution, and the association of the analyte with the supporting electrolyte.

A plot of increasing concentration *vs.* limiting current for pTos with receptor **6** (Figure 4.8), from the cyclic voltammograms of **6** in acetonitrile, reveals that there is a decrease in limiting current although the response is non-linear, attributed to there being two competing chemical equilibria in action. It can be seen that **6** could be used as a receptor for sensing the presence of anions. The use of chiral receptors would allow the effect of the binding site geometry for a given analyte to be determined (see Chiral Sensor section 4.2.3).

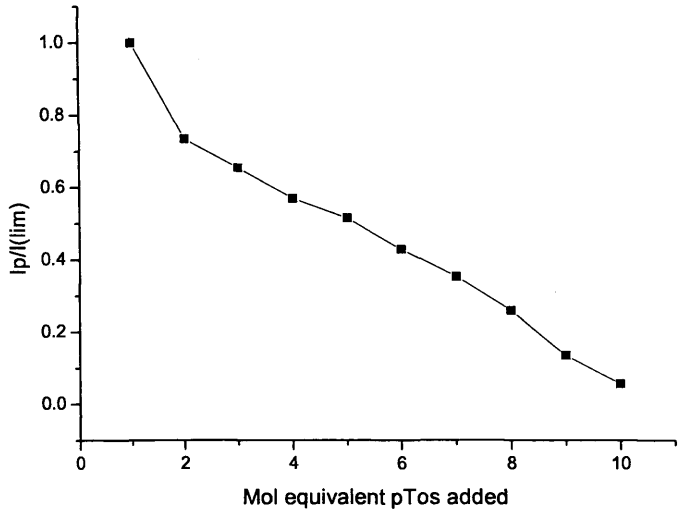

Figure 4.8 Normalised limiting current data for ***6*** *following the addition of 0, 0.9, 1.7, 2.3, 3.3, 3.8, 4.1, 4.4, 4.7 and 5.0 mole equivalents of pTos.*

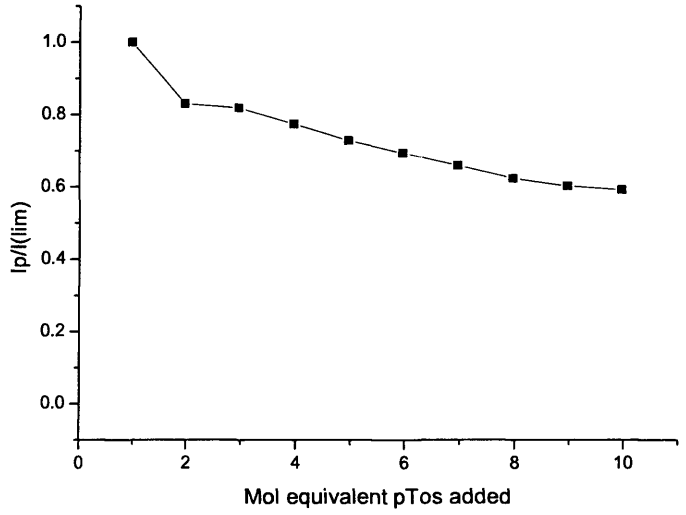

Figure 4.9 Normalised limiting current data for 7 following the addition of 0, 0.9, 1.7, 2.3, 3.3, 3.8, 4.1, 4.4, 4.7 and 5.0 mole equivalents of pTos.

A similar response was observed with receptor **7** for the addition of pTos although not an identical one. This shows that the geometry of the binding site has an effect upon the analyte/receptor interaction.

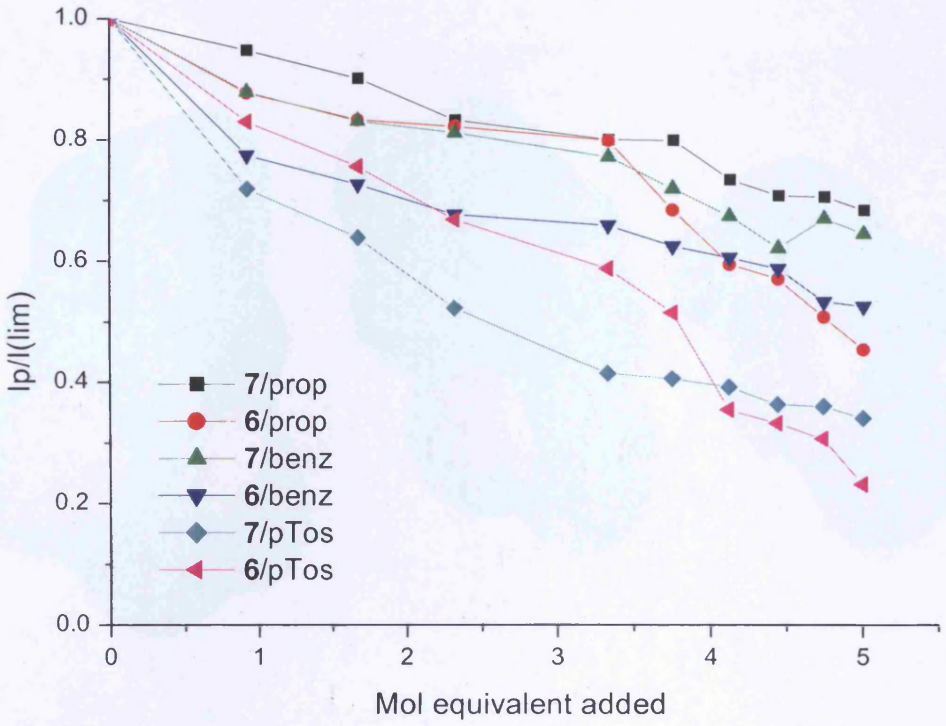

*Figure 4.10 Normalised limiting current data for receptors **6** and **7** following the addition of 0, 0.9, 1.7, 2.3, 3.3, 3.8, 4.1, 4.4, 4.7 and 5.0 mole equivalents of prop, benz and pTos.*

The same experiment was repeated with benzoic acid (benz) and propionic acid (prop) with a summary of the results presented in Figure 4.10. All of the analytes showed the same similar trend in current with increasing analyte concentration, although each analyte had a different effect on the electrochemical response of the receptor. It is evident that the effect of the analytes on the two enantiomers of the ephedrine-substituted binaphthyl salts is different. By looking at the electron density models of the analytes in Figure 4.11 it can be seen that the electronegative region of the $-SO_3H$ group in pTos is bulkier than that of the $-CO_2H$ group in benzoic acid and propionic acid.

p-Toluene sulphonic acid Benzoic acid Propionic acid

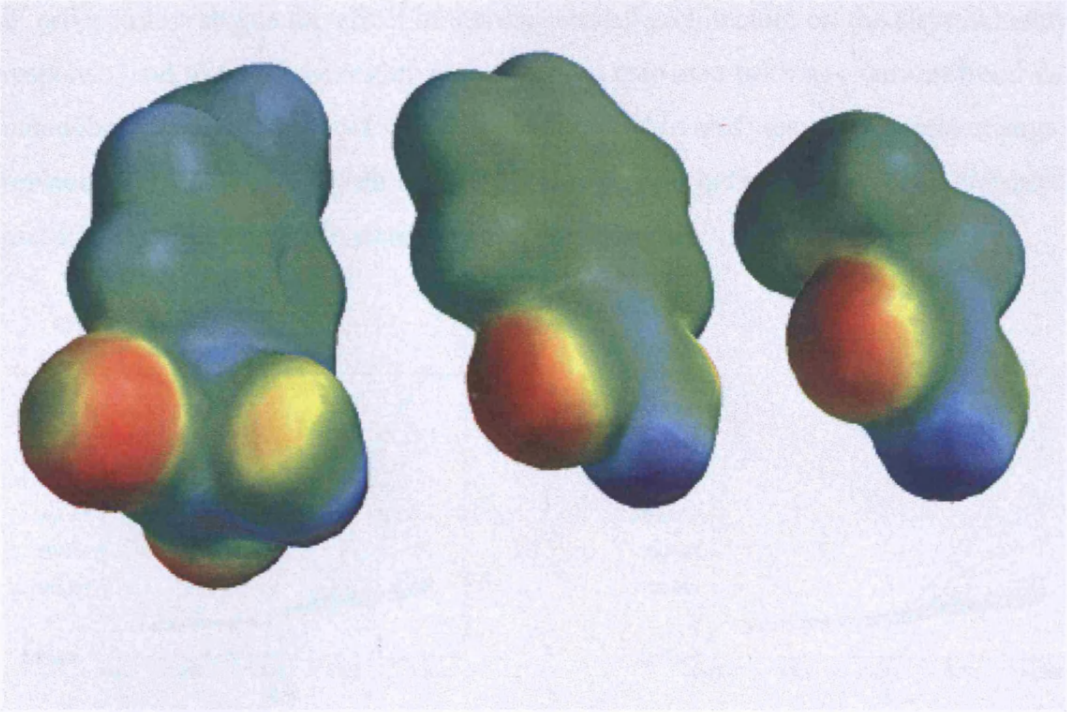

Figure 4.11 Electron density models for pTos, benz, prop

The largest change in electrochemical signal is observed with pTos as the analyte, although there appears to be no clear trends with size or receptor geometry. The difference in trends may be due to the significantly larger pK_a values of sulphonic acids compared to carboxylic acids. This leads to the conclusion that the analyte binds through charge-charge interactions and that the difference is caused by the higher activity of anions in the pTos solutions. Analyte binding and the effect that this has upon the electrochemical response of the receptor is understandably complex. It is clear from the results in Figures 4.10 and 4.11 that the geometry of the binding site and the size of the analyte affect the recognition of the analyte by the receptor. It would seem logical therefore that the receptors should be able to discriminate between enantiomers of a chiral analyte. To test this idea, the effect on the electrochemical response of receptors **6** and **7** by adding chiral analytes to them was determined.

4.2.3 Quaternary Ammonium Binaphthyl Salts As Amperometric Chiral Sensors

In order to investigate the effect of stereochemical architecture on the electrochemical response, and to try to determine a quantitative response from any current trend data, mandelic acid and lactic acid were chosen as suitable analytes. The subtle change of replacing a methyl group with a phenyl group should help to discern any differences associated with a change in stereochemical architecture.

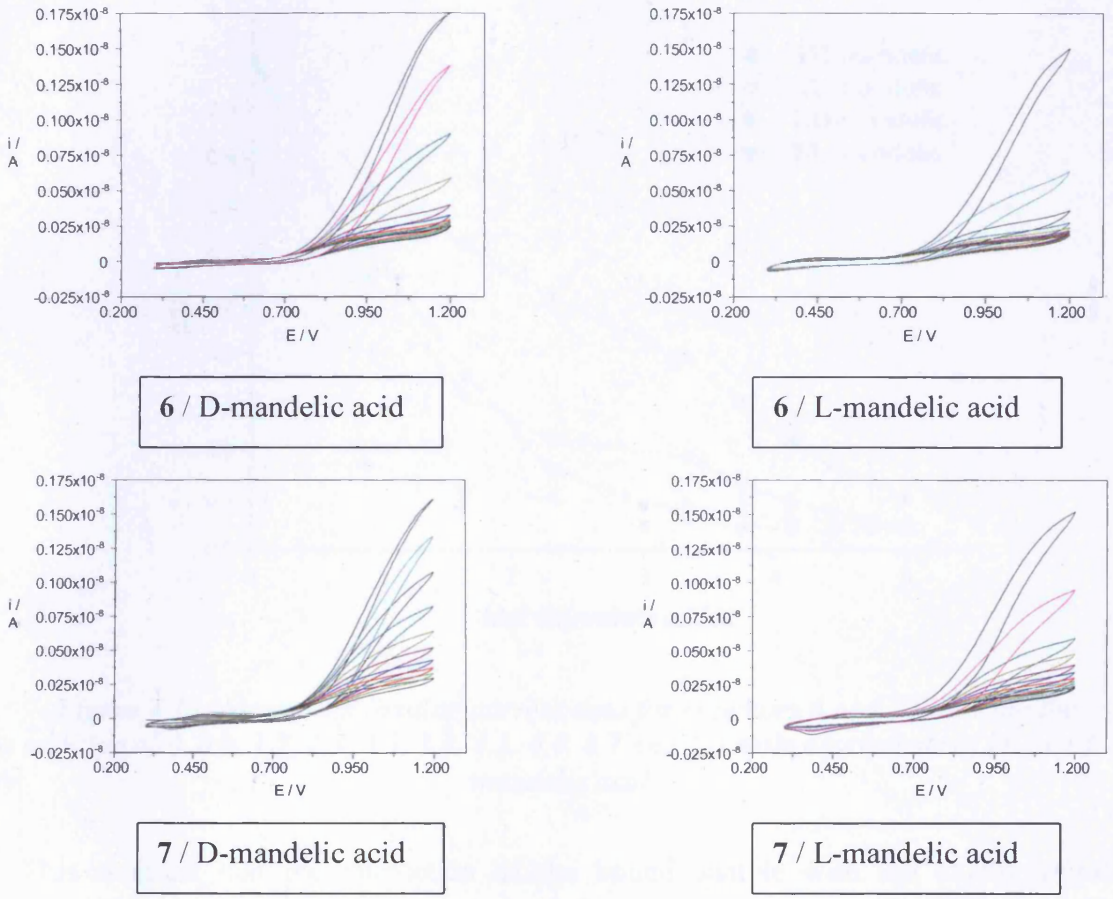

Figure 4.12 Cyclic voltammograms of **6** *and 7 following the addition of 0, 0.9, 1.7, 2.3, 3.3, 3.8, 4.1, 4.4, 4.7 and 5.0 mole equivalents of D- and L- mandelic acid. Potentials quoted vs. Ag/AgBF$_4$ reference electrode.*

The results are presented above for the binding of the two acids with receptors **6** and **7**. Figure 4.12 shows the voltammograms of receptors **6** and **7** with the D- and L-forms of mandelic acid. The two enantiomers of the receptor evidently interact differently with the two forms of the analyte, demonstrating chiral recognition. The

biggest change is observed for the pairing of receptor **6** with the L form of mandelic acid. Conversely the smallest change is observed with the pairing of receptor **7** with the D form of mandelic acid. What is interesting to note is that the other two combinations of analyte and receptor (**7** with L-mandelic acid and **6** with D-mandelic acid) give almost mirror image type responses, perhaps testament to the fact that they are, in real life, mirror images of each other. This is reflected in the normalised current data shown in Figure 4.13.

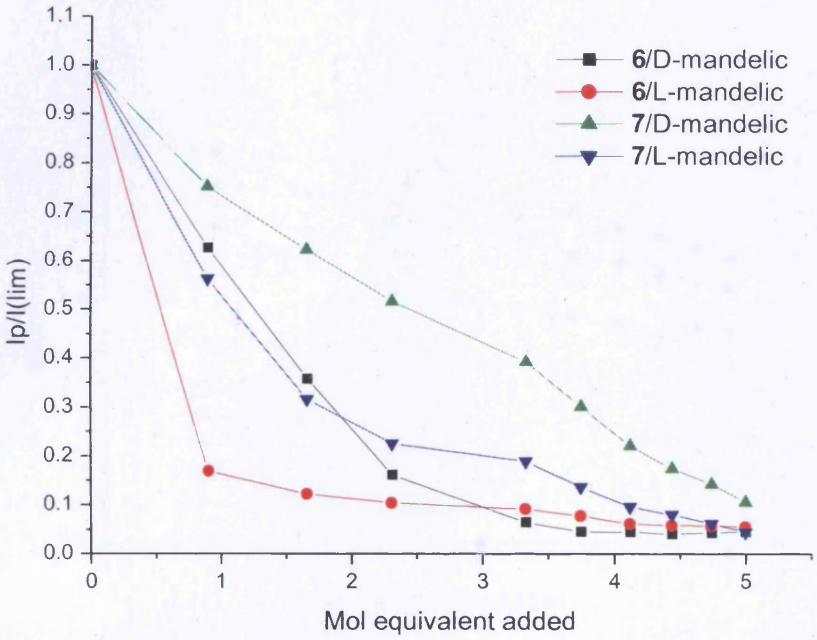

*Figure 4.13 Normalised limiting current data for receptors **6** and **7** following the addition of 0, 0.9, 1.7, 2.3, 3.3, 3.8, 4.1, 4.4, 4.7 and 5.0 mole equivalents of D- and L-mandelic acid.*

This suggests that the interaction of the bound analyte with the axially chiral binaphthyl moiety is constant and that the bound analyte has the same effect upon the stability of the oxidised binaphthyl radical. What we have here in this situation is an example of how the selectivity for the receptor is affected by the stereochemical nature of the analyte. It appears that for mandelic acid, one particular isomer of the ephedrine-substituted binaphthyl (receptor **6**) is more sensitive to a given conformation of an analyte compared to its mirror image. Since the only difference between the two isomers is a stereochemical one, some sort of molecular recognition is therefore taking place. The same analysis was repeated for lactic acid

[$CH_3CH(OH)CO_2H$]. This analyte was chosen since it replaces the phenyl by a methyl moiety and can be used to probe the effect of analyte size on the receptor response while keeping the stereochemistry around the binding site constant. These two acids also have similar pK_a values in water suggesting that anion activity should be similar. It can also be used as a direct comparator to propionic acid as it shows the effect of a polar substituent on the analyte. The OH group of the analyte could have two effects; it could either act as the binding position of the guest, or it could hydrogen bond to some other moiety on the ephedrine side chain. Both of these ideas are explored and discussed with the following sets of results.

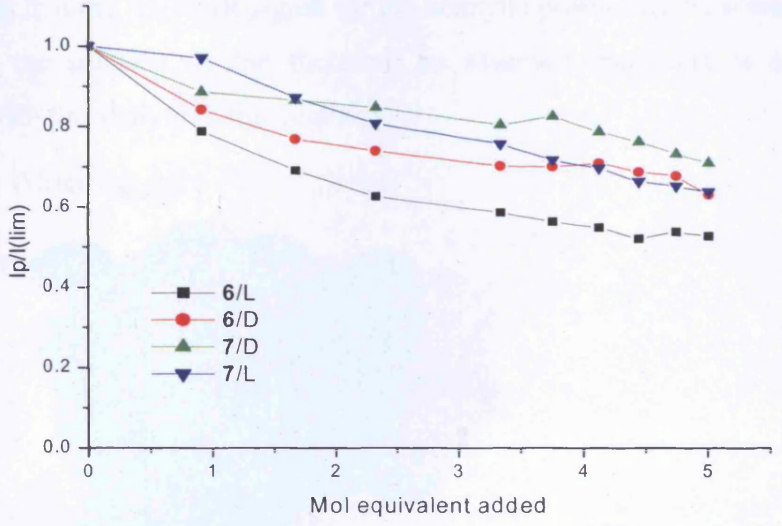

*Figure 4.14 Normalised limiting current data for receptors **6** and **7** following the addition of 0, 0.9, 1.7, 2.3, 3.3, 3.8, 4.1, 4.4, 4.7 and 5.0 mole equivalents of D- and L-lactic acid.*

Lactic acid displays the same trends compared to the data for mandelic acid, i.e. the greatest change in oxidation current was caused by the addition of the L-enantiomer with **6**, the smallest change in oxidation current was caused by the addition of the D-enantiomer with **7** and the remaining two combinations showing similar agreement in the change in reduction current with increasing analyte concentration, all of this information easily discernable from Figure 4.14. The decrease in the limiting current is less than that observed for the corresponding experiment using mandelic acid which shows that the sensitivity of the receptor to the analyte is governed not only by the stereochemical architecture of the binding moiety relative to the analyte's chiral

centre, but also to the overall size of the analyte. This will be due to steric factors, e.g. in the case of mandelic acid the phenyl group restricts movement in the binaphthyl moiety to stabilise the radical formed upon oxidation which would account for the stereospecific response of the receptor, although the stacking of the phenyl group with the binaphthyl moiety could also restrict the motion.

4.3 Discussion

4.3.1 Binding Site Geometry

It can be seen that the ^{1}H-NMR signal for the benzylic protons shifts when the analyte is added to the solution, it can therefore be assumed that there is a significant interaction with the analyte in this region.

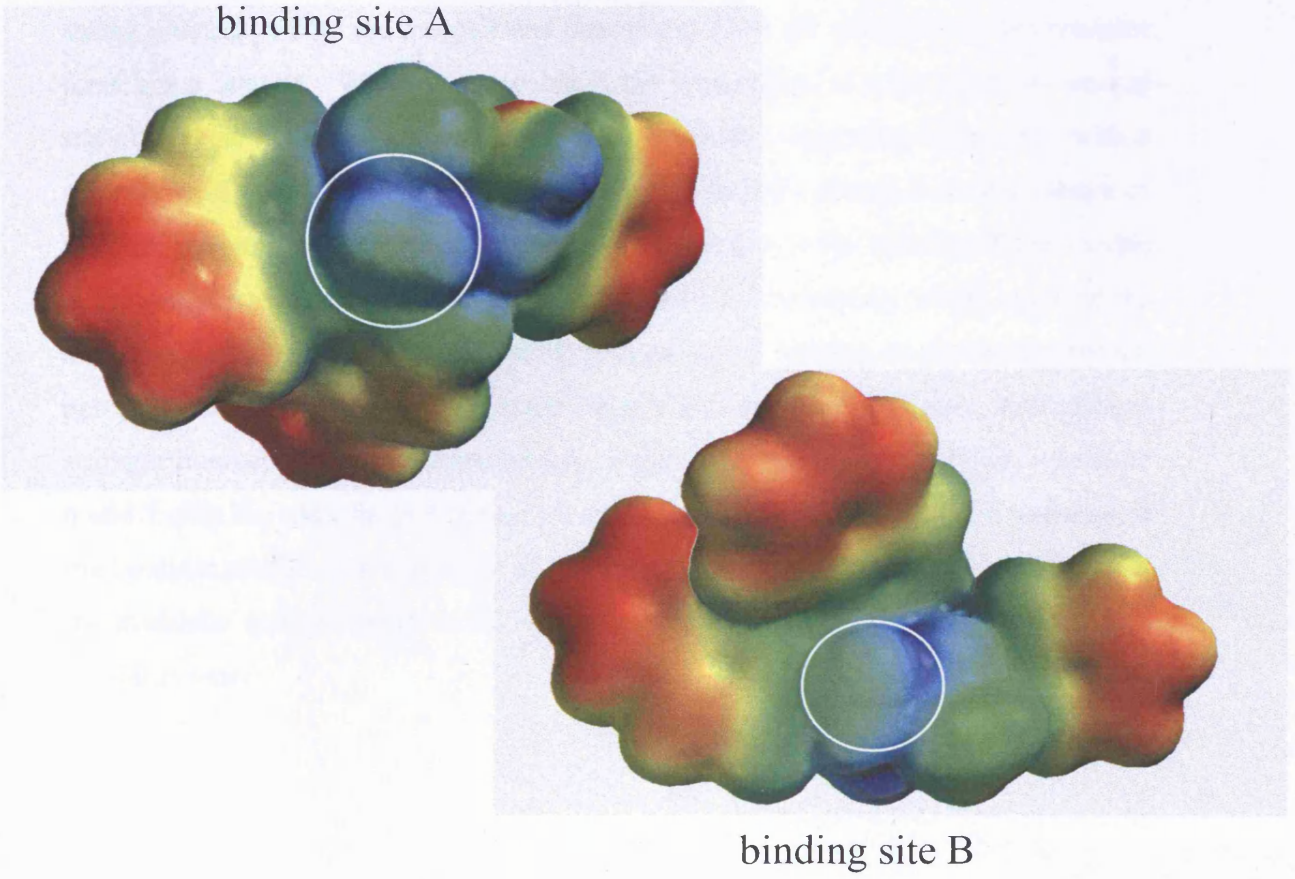

Figure 4.15 Surface Potential maps for possible binding sites on receptor ***6****.*

As can be seen from Figure 4.15, sites A and B are diastereotopic. This is useful to know since it is important to work out where the analyte is binding and which site is dominant in controlling the electrochemical response. Knowing this will help to tailor the selectivity of the receptor in the future since blocking the less sensitive side of the receptor should enhance analyte recognition.

The signals for the four benzylic protons (occurring between 3.7 and 5.5ppm) are shown for clarity in Figure 4.16 (their assignment was confirmed using 2D NMR). It is clear that the addition of mandelic acid to the solution caused negligible change to the position of the resonances of the ***a'***, ***b*** and ***b'*** protons (see below). The signal for proton ***a*** is deshielded for diastereoisomeric **6** and **7** by less than 0.2 ppm and a shift for **6** was only noticeable when a 5 times excess of mandelic acid was added. Of the two possible binding sites, it is suggested therefore that binding site A is the more likely to be affected by interaction with the analyte. This does not, however suggest a strong interaction with the receptor and does not explain the specificity of the receptor for a given analyte. What is noticeable is the appearance of a set of much weaker signals for the benzylic protons of **6** that are shielded, suggesting interaction with a strongly electron-withdrawing moiety. These signals were absent from the spectra of the pure receptor and analyte and must therefore be due to the binding of the analyte to the receptor. It is suggested[41] that these are due to the binding of the anion of the dissociated acid to the receptor. For **7**, a weak signal appears at approximately 6.0 ppm, whereas for **6** it is slightly more intense and occurs at 6.5 ppm, indicating a stronger interaction of the analyte with **6**. Figure 4.17 shows the ^{1}H-NMR spectra of **6** and **7** with the addition of 1 mole equivalent D- and L- lactic acid. The response of the benzylic protons to the addition of the analyte is practically identical to that shown for mandelic acid in Figure 4.16, which suggests that the two analytes bind in a similar manner.

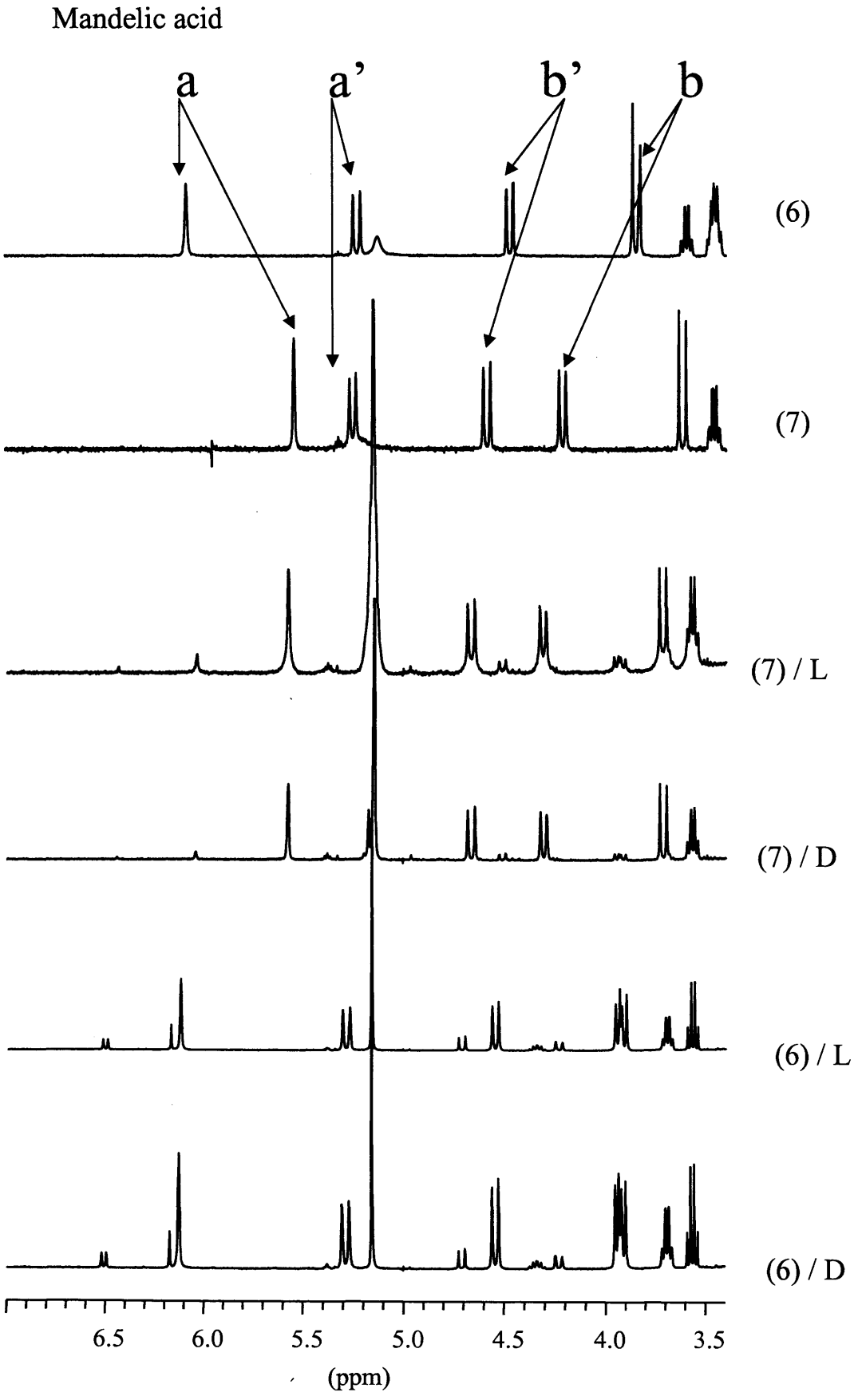

*Figure 4.16 ^{1}H-NMR spectra of **6** and 7 in D_3CCN and the effect of adding 1 mole equivalent of D- and L- mandelic acid.*

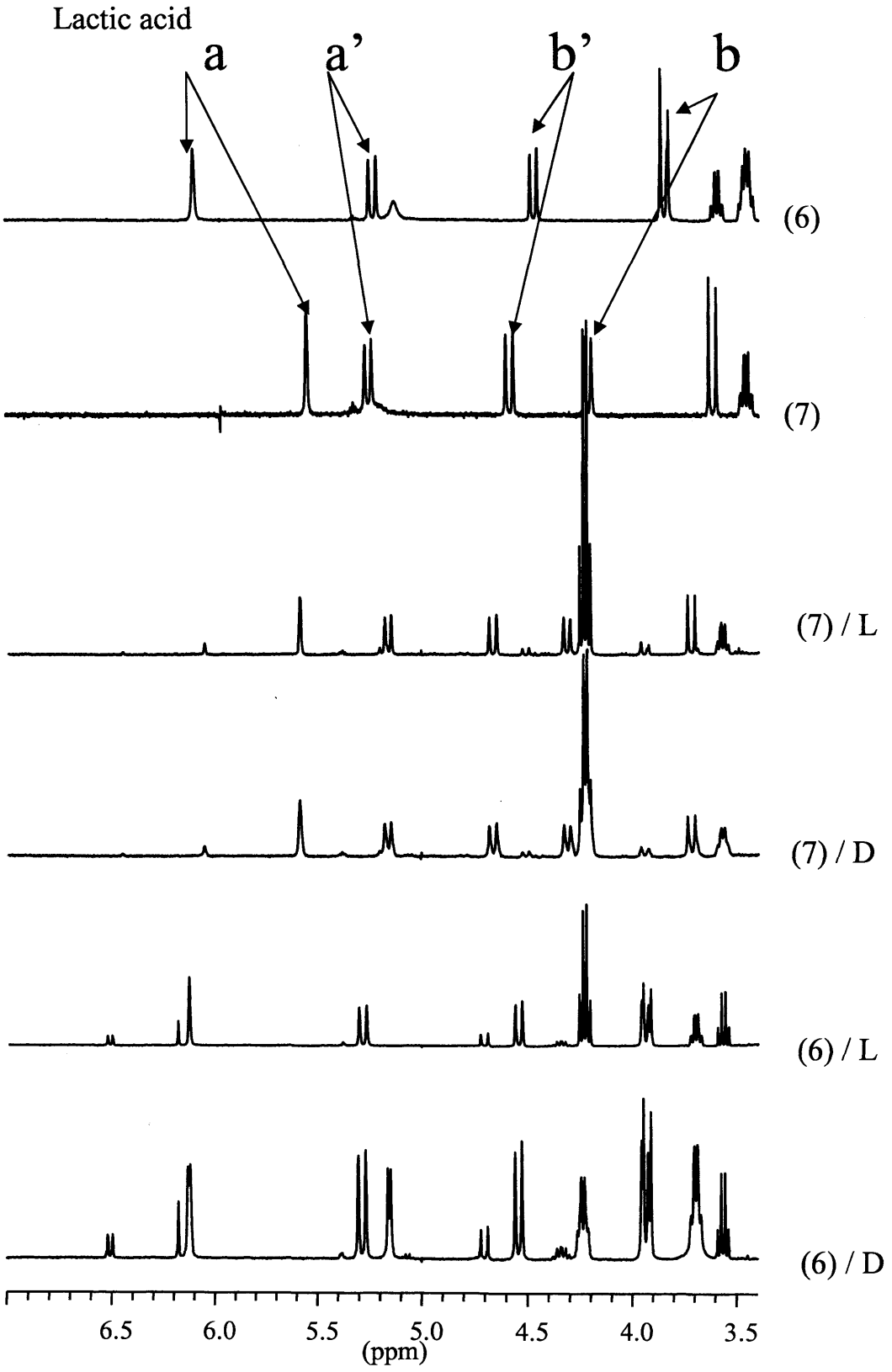

*Figure 4.17 ^{1}H-NMR spectra of **6** and **7** in D_3CCN and the effect of adding 1 mole equivalent of D- and L- lactic acid.*

Figure 4.18 compares the limiting current of D- mandelic, D- lactic and propionic acids with receptors **6** and **7**, which shows the effect of size, polar functional group and binding site conformation more clearly. The largest change is associated with D-mandelic acid confirming that analyte size is the most important factor in determining analyte sensitivity. A comparison of the effect of mandelic acid with lactic acid shows that the same trends are observed for the two receptors, i.e. there is a pronounced curvature to the response of **6** whereas **7** is more linear. At low analyte concentrations the response for **7** with lactic acid is similar to that with propionic acid, but both are less pronounced than the effect of **6** with lactic acid. This suggests that the polar functional group does have some effect but it depends upon the conformation of the binding site. It may involve an interaction with the OH group in the ephedrine side chain and the effect of the various polar substituents (receptors **10-13**) on ephedrine like side chains is discussed in section 4.3.3.

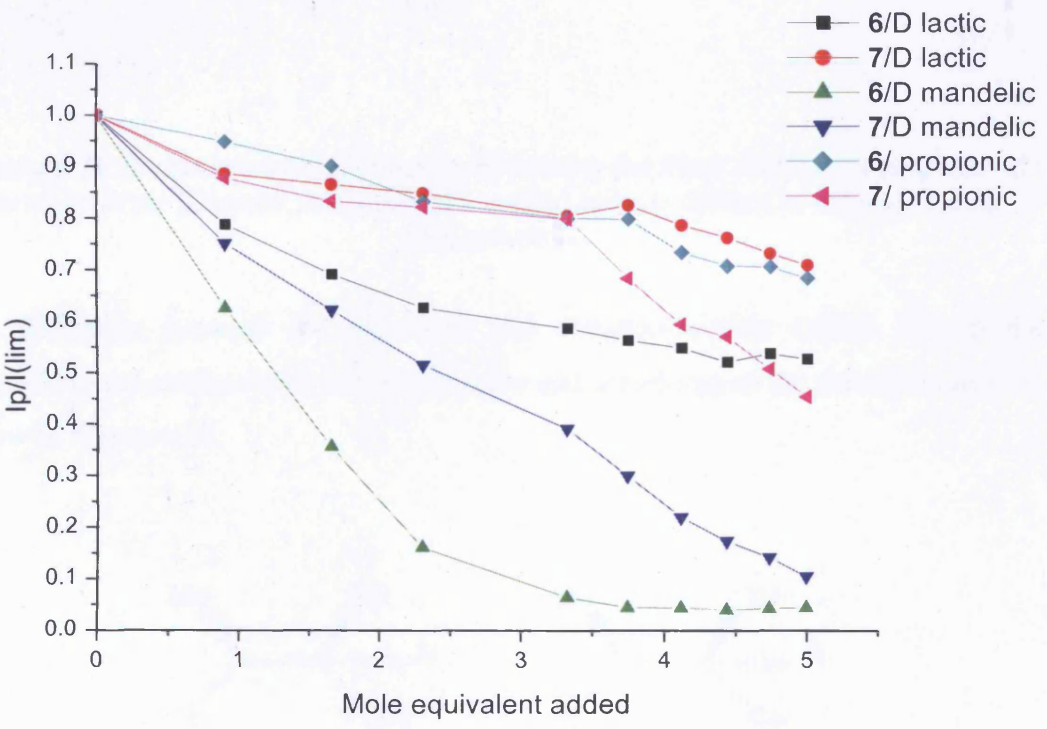

*Figure 4.18 Normalised limiting current data for receptors **6** and **7** following the addition of 0, 0.9, 1.7, 2.3, 3.3, 3.8, 4.1, 4.4, 4.7 and 5.0 mole equivalents of with D-mandelic, D- lactic and propionic acids.*

4.3.2 Pseudoephedrines

In order to illustrate the importance of chirality within the framework of the QABS as a function of analyte sensitivity, the pseudoephedrine binaphthyl salts (receptors **8** and **9**) were synthesized. As there are three chiral centres involved in these molecules, they are defined in terms of the chiral centres from left to right as indicated below in Figure 4.19.

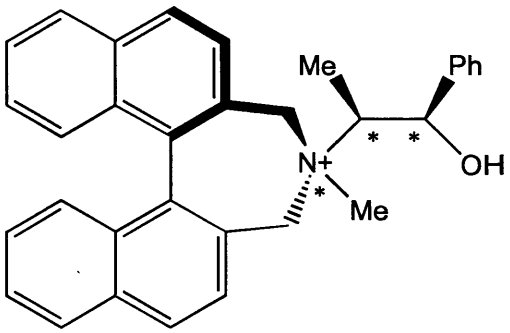

*Figure 4.19 Stereochemistry of receptor **6** showing the three chiral centres, from left to right on the diagram, and using the normal rules is defined as having (S,R,S) configuration.*

The difference between the ephedrine and pseudoephedrine QABS lies in the stereochemical configuration of the ephedrine and pseudoephedrine side-chain as seen below in Figure 4.20.

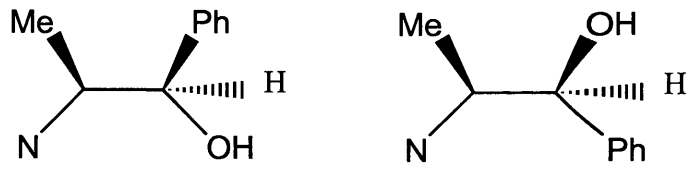

Ephedrine Pseudoephedrine

Figure 4.20 Diagram to show the differences in stereochemistry between the ephedrine and pseudoephedrine side-chains.

The remaining receptors have their stereochemistry around the three chiral carbon centres defined as follows; **7** (R,R,S), **8** (R,R,R) and **9** (S,R,R).

Electrochemical experiments were carried out on them, in a manner analogous to that already mentioned, with D- and L- mandelic acid, with the results presented in Figure 4.20. Negligible variation in the response of receptors **8** and **9** was observed with increasing amounts of D- and L- mandelic acid. The same experiment with the corresponding ephedrine receptors (**6** and **7**, Figure 4.13) produced substantially different limiting current data. There is clearly a significant change in electrochemical response by simply switching the chirality around the β-carbon of the ephedrine side-chain. With receptors **6** and **7** the stereochemistry of the ephedrine side-chain places the OH group (on the carbon atom showing the S configuration) pointing towards the binding site, and the phenyl group on the other side of the molecule pointing away from the binding site. For the pseudoephedrine receptors, **8** and **9**, the stereochemistry of the β-carbon is now in the R configuration and the OH and phenyl groups are reversed.

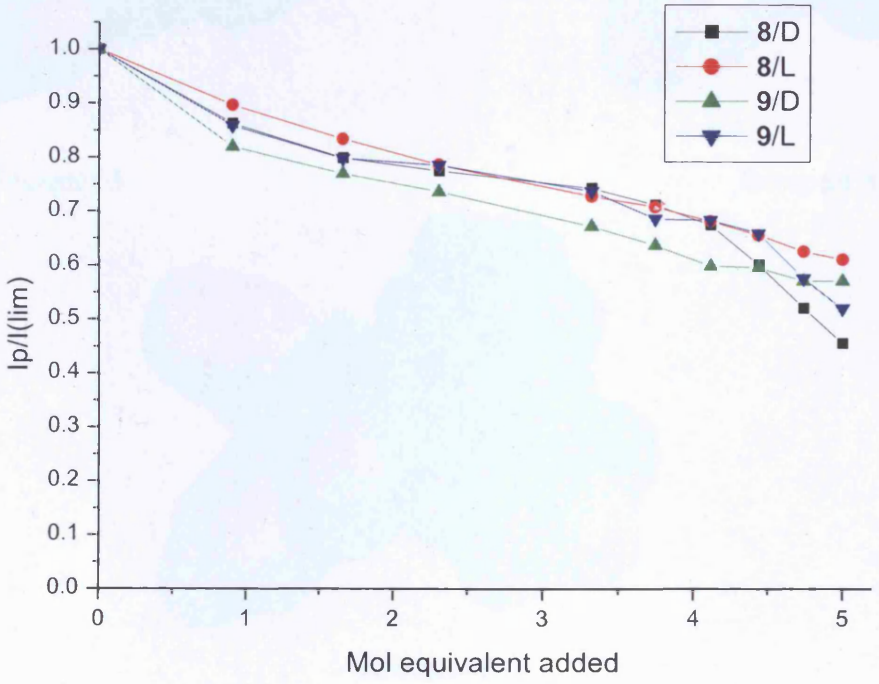

*Figure 4.21 Normalised limiting current data for receptors **8** and **9** following the addition of 0, 0.9, 1.7, 2.3, 3.3, 3.8, 4.1, 4.4, 4.7 and 5.0 mole equivalents of D- and L-mandelic acids.*

The effect that this has on the overall geometry of the binaphthyl receptor is that the phenyl group is now positioned over the quaternary ammonium nitrogen atom and surrounding benzylic protons preventing, or at least hindering, the approach of analyte molecules to the binding site. No selectivity is therefore shown towards a particular enantiomer of mandelic acid from either form of the QABS. This is either due to the phenyl group blocking the approach of the incoming analyte molecule to the binding site, or due to the OH group on the final carbon atom in the chain participating in some sort of enhanced analyte binding effect with the incoming analyte.

4.3.3 Stereochemical Architecture

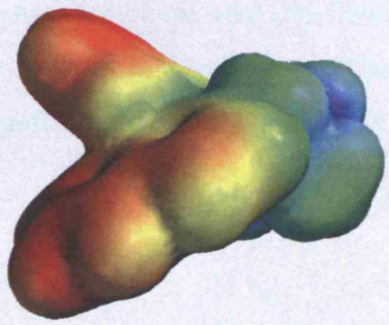

Receptor **3**

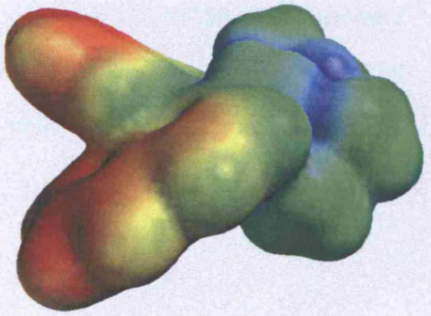

Receptor **4**

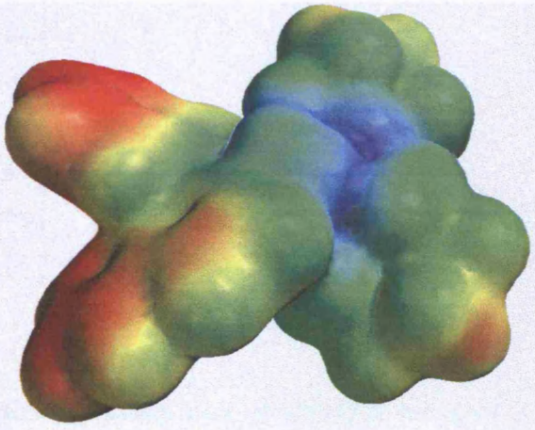

Receptor **5**

*Figure 4.22 Surface Potential maps for receptors **3**, **4** and **5** highlighting possible binding sites.*

From the analysis of the results concerning the anion and chiral sensor, the binding site of electronegative analytes to the binaphthyl receptors was shown to be located in

the vicinity of the electropositive ammonium group. This was confirmed using ^{1}H-NMR spectroscopy where a pronounced shift in the CH_2-N^+ protons was calculated (see Figures 4.16 and 4.17). Figure 4.22 shows the surface potential distributions for receptors **3-5**. The potential distributions around the supposed binding site are not significantly affected by the electron donating properties of the substituents R and R'. Receptors **3-5** differ only in the size of the pendent R groups. These molecules have a plane of symmetry and hence the binding energy of the analyte should be the same on both sides of the molecule. Decreasing the receptor symmetry (receptors **10-13**) may induce analyte binding at one specific site and improve selectivity. The introduction of an electronegative OH group in **10** and **11** could also significantly affect the binding of the analyte through non-charge-charge interactions. Figure 4.22 shows the limiting current for receptor **3** with p-toluene sulphonic acid (pTos), triphenylpropionic acid [$Ph_3CH_2CO_2H$] (tppa) and propionic acid (prop) as a function of analyte concentration. These analytes were chosen as they demonstrate a significant difference in both size and acid dissociation constant.

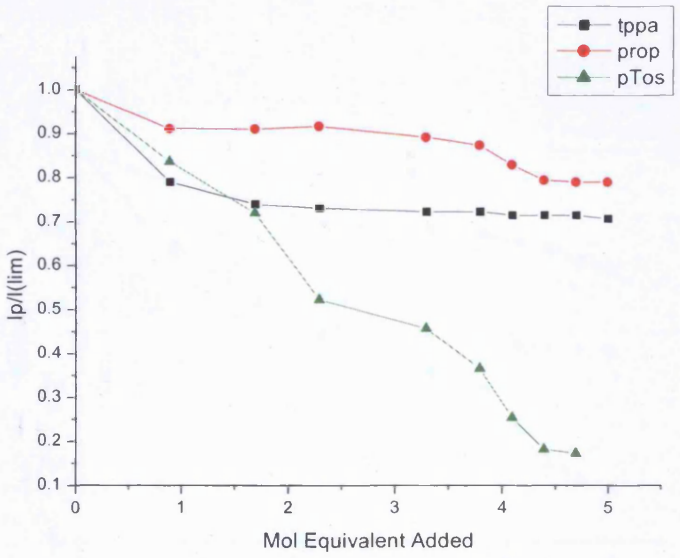

Figure 4.23 Normalised limiting current data for receptor 3 following the addition of 0, 0.9, 1.7, 2.3, 3.3, 3.8, 4.1, 4.4, 4.7 and 5.0 mole equivalents of pTos, tppa and prop.

Figure 4.23 shows that for receptor **3** (R and R' = CH_3) there is negligible steric hindrance to the analyte binding and the decrease in limiting current should just be indicative of the analyte-receptor binding constant. The electrochemical sensitivity of the receptor to the analytes is in the order pTos > tppa > prop. This is a surprising

result since it had been previously postulated[35] that the effect of the analyte was to sterically hinder the stabilisation of the cation radical. ^{1}H-NMR evidence, however, also suggested that the dissociated anion had a larger interaction with the receptor than the associated acid and since the pK_a for pTos is larger than the other two carboxylic acids, then the observed trend is to be expected. Hence it can be concluded that the receptors act as a sensor for anion activity rather than analyte concentration.

Figure 4.24 shows the corresponding data to Figure 4.23 using **4** as the receptor. On receptor **4** the methyl groups from **3** have been replaced with isopropyl groups and this has a small but significant effect upon the response of the receptor towards the three analytes, presumably due to steric hindrance. As the R groups become bulkier the strain imparted on the CH_2-N^+-CH_2 part of the receptor is increased. As it was previously shown, the geometry around the N^+ group is of paramount importance in determining the sensitivity of the receptor to the analyte, receptor **5**, in which the R and R' groups are cyclohexyl, was used as the receptor for comparison purposes.

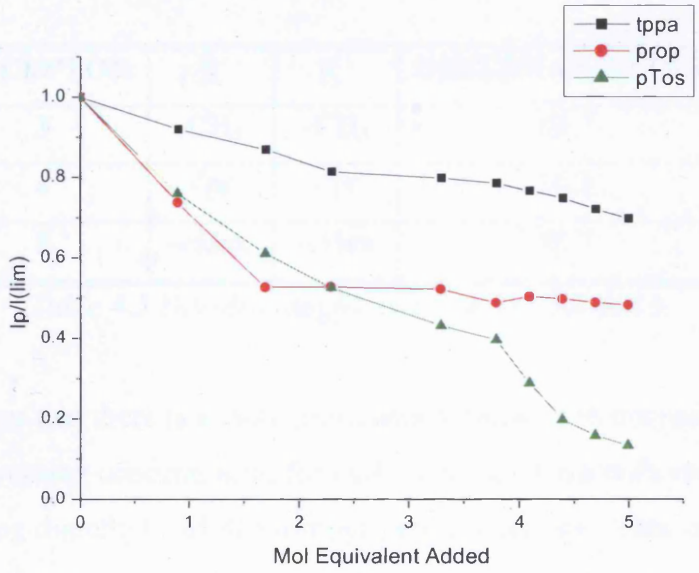

*Figure 4.24 Normalised limiting current data for receptor **4** following the addition of 0, 0.9, 1.7, 2.3, 3.3, 3.8, 4.1, 4.4, 4.7 and 5.0 mole equivalents of pTos, tppa and prop.*

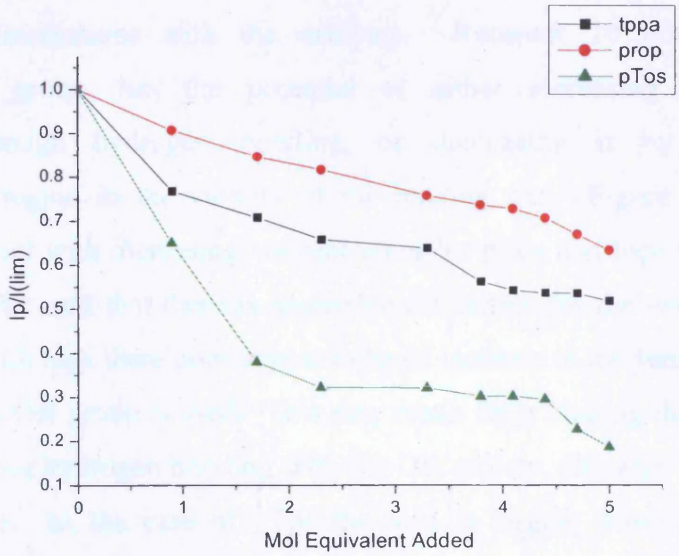

*Figure 4.25 Normalised limiting current data for receptor **5** following the addition of 0, 0.9, 1.7, 2.3, 3.3, 3.8, 4.1, 4.4, 4.7 and 5.0 mole equivalents of pTos, tppa and prop.*

Table 4.3 illustrates that the dihedral angle between the naphthyl moieties is affected by the size of the pendant groups R and R' on the receptor.

RECEPTOR	R	R'	DIHEDRAL ANGLE
3	$-CH_3$	$-CH_3$	64.7
4	$-^{i}pr$	$-^{i}pr$	56.1
5	-cHex	-cHex	55.7

*Table 4.3 Dihedral angles of receptors **3,4** and **5**.*

Figure 4.25 shows that there is a more pronounced decrease in the normalised limiting current with increasing concentration for each of the analytes with receptor **5** than for the corresponding dimethyl and diisopropyl pendant groups. This confirms the idea that bulkier substituents typically increase the sensitivity of the receptor to the analyte presumably due to the regio-conformation around the quaternary ammonium nitrogen atom. For the majority of receptors the change in current with analyte concentration is linear showing that these receptors could be used as the basis for an analytical sensor. Significant deviations from linearity are only really observed for pTos, which is highly dissociated in solution and hence anion activity may not vary linearly with concentration. This should, however be a minor effect since the analyte concentration

does not exceed 0.01 mol dm^{-3} in any of the solutions. Receptors **3-5** rely solely on charge-charge interactions with the analytes. Receptor **10** however, with an additional OH group, has the potential of either increasing receptor-analyte interactions through hydrogen bonding, or decreasing it by acting as an electronegative region in the vicinity of the binding site. Figure 4.26 shows the normalised current with increasing concentration for pTos and tppa with receptors **4** and **10**. It can be seen that there is negligible difference for the two receptors with pTos whereas with tppa there does appear to be an increase in the sensitivity when the receptor with an OH group is used. This may result from binding the receptor to the associated acid via hydrogen bonding with the OH moiety, although ^{1}H-NMR results are inconclusive. In the case of pTos the acid is largely dissociated and hence unaffected by alternative mechanisms.

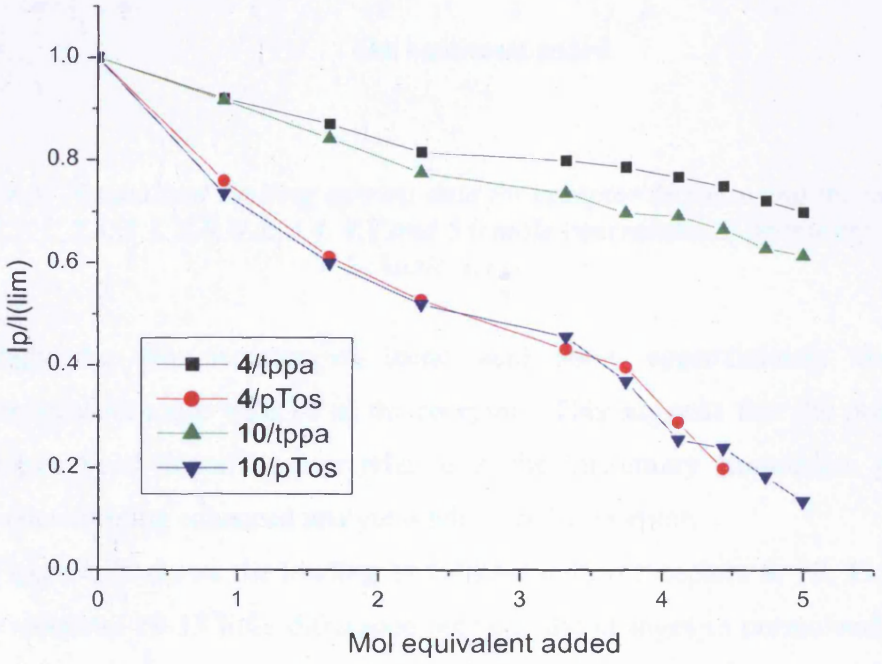

*Figure 4.26 Normalised limiting current data for receptors **4** and **10** following the addition of 0, 0.9, 1.7, 2.3, 3.3, 3.8, 4.1, 4.4, 4.7 and 5.0 mole equivalents of pTos and tppa.*

Figure 4.27 shows the effect of having an OH group on both the receptor and the analyte. The decrease in normalised current with increasing analyte concentration is more pronounced for propionic acid than for either isomer of lactic acid. This cannot

result from the difference in K_a of the two analytes since the value for lactic acid is larger than that for propionic acid (K_a in water; propionic acid = 1.34×10^{-5} and lactic acid = 1.4×10^{-4}).

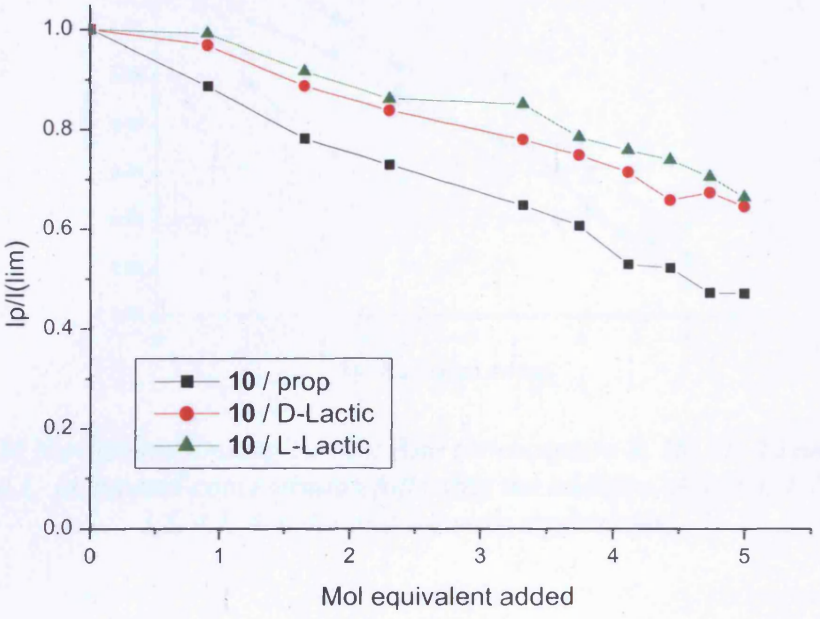

*Figure 4.27 Normalised limiting current data for receptor **10** following the addition of 0, 0.9, 1.7, 2.3, 3.3, 3.8, 4.1, 4.4, 4.7 and 5.0 mole equivalents of propionic, D-, and L- lactic acids.*

Interestingly the two isomers of lactic acid show approximately the same electrochemical response with **10** as the receptor. This suggests that the position of the hydrogen bond donor/acceptor relative to the quaternary ammonium group is crucial in determining enhanced analyte binding to the receptor.

Figure 4.28 shows the binding of L-lactic acid to receptors **8, 10, 11, 12** and **13**. For receptors **10-13** little difference between the changes in normalised current with analyte concentration is observed. Controlling the stereochemistry of the OH group has a small but significant effect on the binding of the analyte and the sensitivity of the receptor. This suggests that the regiochemistry of the OH group relative to the N^+ group is responsible for constructive binding interactions. The observation that axially chiral enantiomers of **8** bind the stereoisomers of lactic acid differently confirms that the receptor /analyte binding is enantioselective.

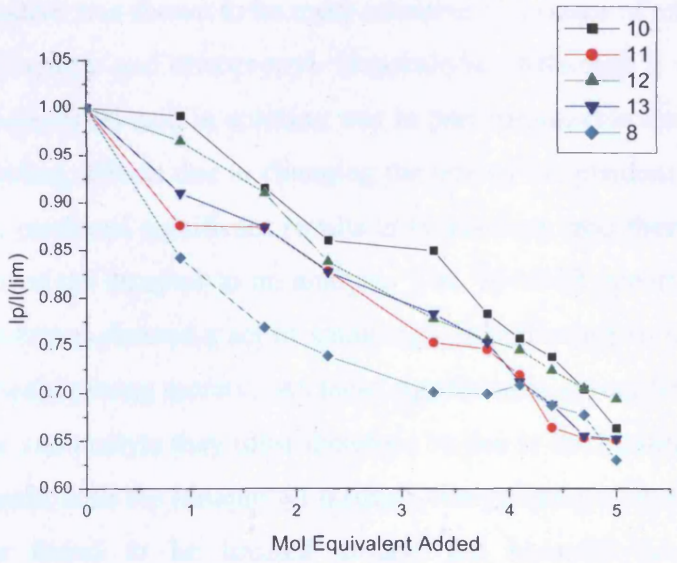

Figure 4.28 Normalised limiting current data for receptors ***8, 10, 11, 12*** *and* ***13*** *as a function of L- lactic acid concentration following the addition of 0, 0.9, 1.7, 2.3, 3.3, 3.8, 4.1, 4.4, 4.7 and 5.0 mole equivalents.*

4.4 Conclusions

The binding of a Group 1 metal cation (Li^+, Na^+) to the azacrown derivatized binaphthyl salt was shown to affect its electrochemical response in solution, causing a reduction in the limiting current of the QABS. The same was also found to be true for the ion pairing of bulky anions to the benzylic protons of some of the other binaphthyl salts. The concentration of analytes in solution was found to be related to the limiting current (an observable analytical signal) and so the QABS could therefore form the basis of an ameperometric sensor. Modifying the groups around the quaternary ammonium nitrogen allowed the enantioselective recognition of chiral analytes to be demonstrated with mandelic and lactic acid used as examples. The scope for tailoring the binaphthyl salts for a chosen analyte is therefore vast and requires further investigation. Bulkier substituents appear to increase the sensitivity of the receptor for a given anionic analyte. The larger the size of the pendant group attached to the quaternary ammonium nitrogen, the more sterically distorted the binaphthyl becomes upon electrooxidation. An increase in the strain around the molecule causes the dihedral angle between the two naphthalene groups to decrease making the formation of the radical cation thermodynamically more difficult to form. The dicyclohexyl-

substituted derivative was shown to be more sensitive to a range of analytes compared to the smaller dimethyl- and diisopropyl- binaphthyls. Although it was thought that the pK_a of the dissociated acid in solution was in part responsible for determining the selectivity of binding, effects due to changing the size of the pendent group cannot be ignored as these produced significant results in themselves, and therefore play a role in the sensitivity of the receptor to an analyte. The ^{1}H-NMR spectra of the receptor and analyte in solution showed a set of small signals indicating an interaction with a strong electron-withdrawing moiety. As these signals were absent from the spectra of the pure receptor and analyte they must therefore be due to the binding of the anion of the dissociated acid with the binaphthyl through charge-charge interactions. The set of signals was found to be located around the benzylic protons (the most electropositive region of the molecule, as confirmed by molecular modelling calculations), something that is clearly not a coincidence. As the benzylic protons are diastereotopic it is possible that one side of the molecule is dominant in controlling the electrochemical response of the receptor. Knowing this information will help when it comes to modifying the selectivity of the receptor. The geometry of the binding site combined with the size and functionality of the analyte affects the recognition of the analyte by the receptor. As has already been seen, blocking one of the diastereotopic binding sites on the binaphthyl enhances the sensitivity of analyte recognition. Increasing the size of the pendant group attached to the quaternary ammonium nitrogen has a similar effect. What is also apparent is that controlling the regiochemistry of the OH group relative to the N^+ group is responsible for constructive binding interactions. Building on this knowledge will allow the QABS to be tailored for a variety of specific analytes, enhancing their selectivity and sensitivity along the way.

4.5 References

1) A.P.Abbott, C.S.M.Chung, I.G.Stara, I.Stary and P.Kocovsky, *Chem.Commun.*, (1999), 641.
2) P.D.Beer, in *Advances in Inorganic Chemistry*, ed. A.G.Sykes, Academic Press, New York, (1992), vol.39, 79.
3) P.D.Beer, *Chem.Soc.Rev.*, **18**, (1989), 409.
4) R.J.Mortimer and J.S.Weightman, *J.Electroanal.Chem.*, **418**, (1996), 1.
5) F.Vögtle, *Supramolecular Chemistry*, Wiley, New York, 1991, Ch 2, pp. 27-83.
6) G.W.Gokel, *Crown Ethers and Cryptands*, The Royal Society of Chemistry, Cambridge, 1991.
7) A.K.Covington, H.Grey, P.M.Kelly, K.I.Kinnear and J.C.Lockhart, *Analyst* (London), **113**, (1988), 895.
8) G.J.Moody, B.B.Saad and J.D.R.Thomas, *Analyst* (London), **114**, (1989), 15.
9) E.Pergel, R.E.Gyurcsányi, K.Tóth and E.Lindner, *Anal.Chem.*, **73**, (2001), 4249.
10) J.D.R.Thomas, *Pure Appl.Chem.*, **73**(1), (2001), 31.
11) E.Bakker, E.Pretsch and P.Bühlmann, *Anal.Chem.*, **72**, (2000), 1127.
12) V.Peyre, S.Baillet and P.Letellier, *Anal.Chem.*, **72**, (2000), 2377.
13) A.Ceresa, E.Bakker, B.Hattendorf, D.Günther and E.Pretsch, *Anal.Chem.*, **73**, (2001), 343.
14) S.Jadhav and E.Bakker, *Anal.Chem.*, **73**, (2001), 80.
15) J.N.Demas and B.A.Degraff, *J.Macromol. Sci. Chem.*, **A25**, (1988), 1189.
16) S.Basak, Y.H.Ho, E.W.Tsai and K.Rajeshwar, *J.Chem.Soc.Chem.Commun.*, (1989), 462.
17) S.K.Cha and H.D.Abruña, *Anal.Chem.*, **62**, (1990), 274.
18) P.D.Beer, *Chem.Soc.Rev.*, **18**, (1989), 409.
19) P.D.Beer, *Adv. Inorg. Chem.*, **39**, (1992), 79.
20) P.D.Beer, O.Kocian, R.J.Mortimer and C.Ridgeway, *J.Chem.Soc.Faraday Trans.*, **89**(2), (1993), 333.
21) P.D.Beer, N.C.Fletcher, A.Grieve, J.W.Wheeler, C.P.Moore and T.Wear, *J.Chem.Soc.Perkin Trans.*, **2**, (1996), 1545.
22) P.D.Beer, Z.Chen and P.A.Gale, *Tetrahedron*, **50**(3), (1994), 931.

23) P.D.Beer, D.Hesek, J.Hodacova, and S.E.Stokes, , *J.Chem.Soc.Chem.Commun.*, (1992), 270.

24) P.D.Beer, M.G.B.Drew, C.Hazelwood, D.Hesek and S.E.Stokes, *J.Chem.Soc.Chem.Commun.*, (1993), 828.

25) C.R.Leidner, B.P.Sullivan, R.A.Reed, B.A.White, M.T.Crimmins, R.W.Murray and T.J.Meyer, *Inorg.Chem.*, **26**, (1987), 882.

26) J.M.Calvert, R.H.Schmehl, B.P.Sullivan, J.S.Facci, T.J.Meyer and R.W.Murray, *Inorg.Chem.*, **22**, (1983), 2151.

27) C.Belloncle, P.Cauliez and J.Simonet, *J.Electroanal.Chem.*, **444**, (1998), 101.

28) U.Anton, M.Adam, M.Wagner, Z.Qi-Lin and K.Müllen, *Chem.Ber.*, **126**, (1993), 517.

29) M.J.S.Dewar, E.J.Zoebisch, E.F.Healy and J.J.P.Stewart, *J.Am.Chem.Soc*, **107**, (1985), 3902.

30) P.S.Bates, R.Kataky and D.Parker, *J.Chem.Soc.,Perkin Trans.2*, (1994), 669.

31) R.Kataky and D.Parker, *Analyst*, **121**, (1996), 1829.

32) A.Gafni, Y.Cohen, R.Kataky, S.Palmer and D.Parker, *J.Chem.Soc.,Perkin Trans.2*, (1998), 19.

33) K.Kroger, A.Jung, S.Reder and G.Gauglitz, *Analytica Chimica Acta*, **469**, (2002), 37.

34) A.A.Ensafi and A.Kazemzadeh, *Microchemical Journal*, **72**, (2002), 193.

35) A.P.Abbott, G.Barker, G.R.Lonergan, A.J.Walter and P.Kocovsky, *The Analyst,* **126**, (2001), 1892.

36) A.P.Abbott, G.W.Barker, A.J.Walter and P.Kocovsky, *The Analyst,* **128**, (2003), 245.

37) A.J.Pearson, J-J Hwang and M.E.Ignatov, *Tetrahedron Letters*, **42**, (2001), 3537.

38) D.A.Gustowski, V.J.Gatto, A.Kaifer, L.Echegoyen, R.E.Godt and G.W.Gokel, *Chem. Commun.*, (1984), 923.

39) A.Kaifer, D.A.Gustowski, L.Echegoyen, V.J.Gatto, R.A Schultz, T.P Cleary, C.R Morgan, D.M.Goli, A.M.Rios and G.W.Gokel, *J.Am.Chem.Soc*, **107**, (1985), 1958.

40) G.W.Gokel, *Crown Ethers and Cryptands*, The Royal Society of Chemistry, Cambridge, 1991.

41) A.P.Abbott, G.W.Barker, D.L.Davies, G.A.Griffths, A.J.Walter and P.Kocovsky, *Anal.Chem.*, **74**, (2002), 4002.

Chapter 5
Mechanical Resonance Effects In Polymer Wax Films

5.1 Introduction

The mechanical resonance effects of many different types of polymer films, notably the readily synthesised polymers such as poly(vinylferrocene), poly(propylene) or poly(vinylchloride), affected by changes in temperature, frequency, chemical constituent or potential have been studied in detail[1-2]. One group of polymers that appear to have been left out are wax films, typically found on the surfaces of plant leaves.

Exploiting the fundamental harmonic resonance of a polymer film allows the user to extract a large amount of information on the structure and nature of the polymer film under investigation. In the simplest case, TSM resonators can be employed as basic gravimetric sensors for the detection of gaseous molecules or simple aqueous metal ions by adsorption onto the surface of the resonator. Probing further into the data obtained for polymer films at or near resonance, it is possible to extract information on the properties and characteristics of the films used in impedance analysis. This is conveniently achieved using shear modulus parameters.

The aim of this study is the manipulation of shear moduli (G) of polymer wax films. An intermediate goal in reaching this aim is the rationalisation of G in terms of frequency and temperature. In general terms, there has been a large volume of literature (discussed in the Introduction) on the viscoelastic characteristics and properties of many polymeric materials. There has been almost no progress on polymer wax films to date, with regards to the methodology or analysis as presented in this thesis.

The results presented within this chapter aim to characterise a generic paraffin wax film and to highlight the structural changes taking place within the film due to the effect of temperature. The ability of simple Maxwell and Voigt models to characterise polymer wax films is examined, which have been widely used for the analysis of *bulk* material properties, to explain variations in G' and G''. An attempt is made to discuss the data presented in terms of shear modulus contributions and in general, provides an interesting and pivotal introduction to the manipulation of

polymer wax films and plant wax components that are explored and discussed in greater depth in Chapter 6.

5.2 Experimental

The uncoated TSM resonator was fully characterised before each experiment using crystal impedance measurements of the blank crystal exposed to air. Paraffin wax films were then deposited onto 10 MHz quartz crystals in the manner described in the Experimental Chapter, section 3.3.2.2. Surfactants were added drop-wise to the surface of the crystal as required until the piezoelectrically active area of the wax component/wax film under investigation was completely covered with both film and surfactant in the vertical axis. Crystal impedance measurements were then recorded at the fundamental harmonic over a suitable temperature range in order to obtain shear modulus values.

5.3 Results

The results in this chapter introduce the concept of resonance in a polymer wax film. In order for any crystal impedance measurements to be taken it is essential to record several key spectra to start with, notably the blank crystal exposed to air, the crystal with film attached/adhered to the surface and a series of spectra of the film during an experiment. The following section explores the spectra of a polymer wax film attached to the surface of a quartz crystal and goes on to examine the effect of having a liquid loaded on top of the polymer wax film.

5.3.1 Resonance In A Paraffin Wax Film

A comparison of the spectra of a blank crystal and a crystal with a film attached is presented in Figure 5.1.

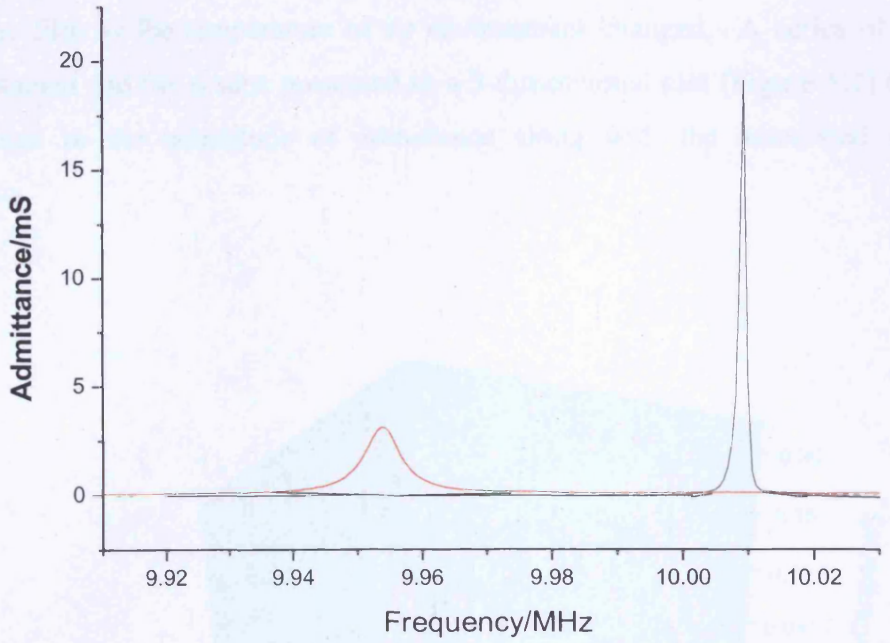

Figure 5.1 Comparison of the spectra of a blank crystal exposed to air (—) and the same crystal with a paraffin wax film attached (—). An increase in mass attached to the surface of the crystal causes a simultaneous decrease in admittance and shift to lower frequencies due to damping caused by the attached material.

It can be seen that there is a significant change in appearance of the two peaks. A polymer wax film adhered to the surface of the quartz crystal causes a damping in the magnitude of admittance as well as a downward shift in frequency. This is easily explained. For lossless films, $G'' = 0$ and Z_e is imaginary. Z_e then represents energy stored in the film, becoming infinite at film resonance. For lossy films, $G'' > 0$ and Z_e becomes complex with the real part (R_2) representing power dissipation in the film and the imaginary part (L_2) representing energy storage. A condition of film resonance occurs when the acoustic phase shift φ across the film reaches an odd multiple of $\pi/2$. This enhances the coupling of acoustic energy within the film. This can lead to changes in the resonant frequency, Δ_f, and damping, R_2, for the coated TSM resonator that can be extracted from Z_e.

The resonance of this polymer wax film can be explored by adjusting either the frequency at which the data is recorded (*i.e.* by recording the spectra at higher harmonics) or by simply increasing the temperature. An experiment was conducted where a paraffin wax coated crystal was heated in an attempt to establish the change in resonance of the paraffin wax film at various temperatures. Water was also added

to the surface of the paraffin wax in a bid to provide a layer that would homogenously warm the film as the temperature of its environment changed. A series of spectra were obtained and the results presented in a 3-dimensional plot (Figure 5.2) to show the change in the magnitude of admittance along with the associated shift in frequency.

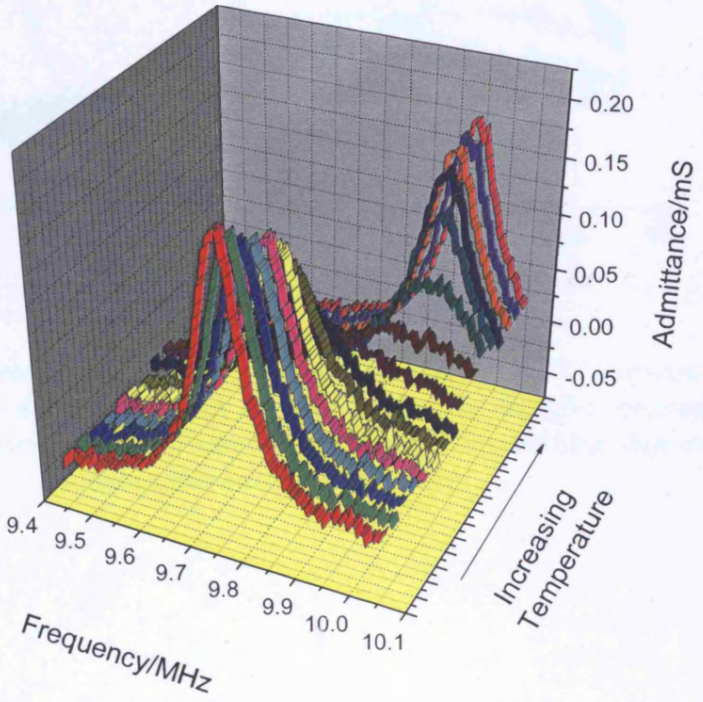

Figure 5.2 A 3-D plot to show the change in admittance with increasing temperature on a paraffin wax sample; spectra front to back represent a 1°C rise in temperature from 27-42°C.

The data from Figure 5.2 are repeated in a 2-dimensional plot in Figure 5.3. Although the 3-dimensional plot in Figure 5.2 is an elegant method to present the data qualitatively, Figure 5.3 is more useful for quantitative purposes. The really interesting part to this experiment is the treatment of the data to obtain the shear modulus parameters for the paraffin wax film over a series of increasing temperatures. Using the appropriate model and the fitting program outlined already in Table 2.1 and Figure 3.6 respectively, the storage and loss moduli (G' and G'') were obtained for a paraffin wax film (h_f and ρ_f for the film were 6 μm and 0.90 g cm^{-3}, respectively). The results from the experiment outlined above are shown in Figure 5.4.

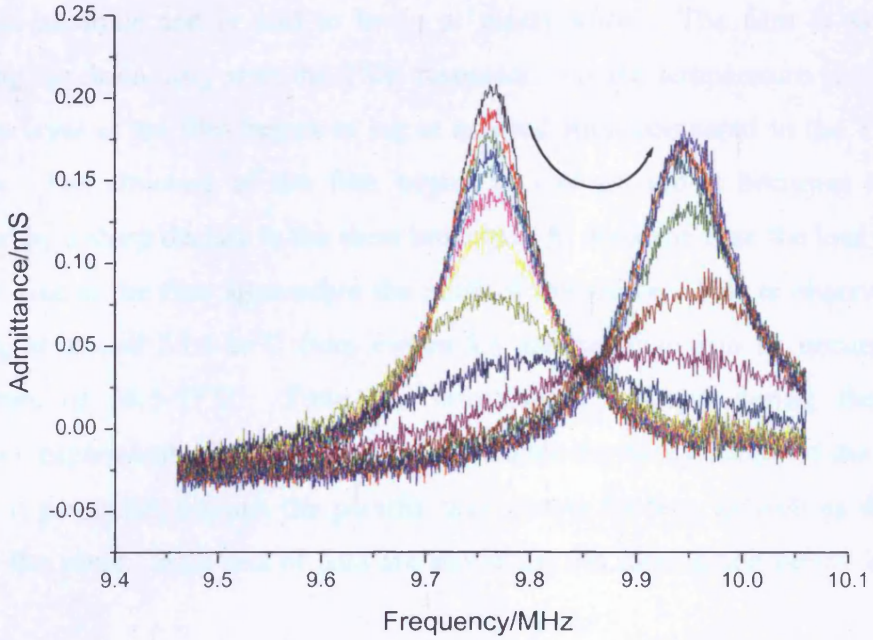

Figure 5.3 Data from Figure 5.2 in a 2-D plot for clarity; a 1°C increase in temperature from 27- 42°C is shown by successive spectra; the effect of gradually increasing temperature causes a decrease in admittance followed by a shift to higher frequency/increase in admittance.

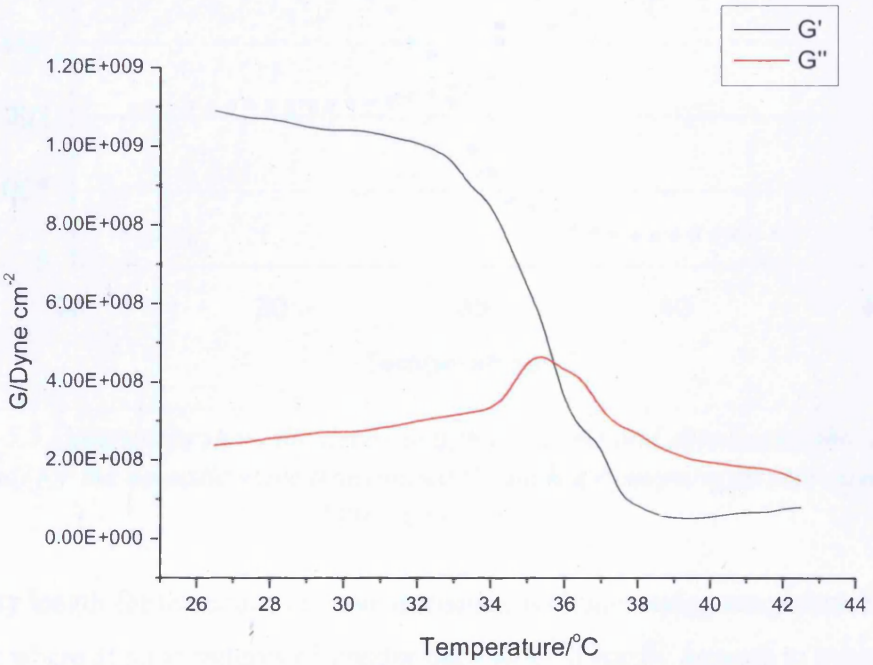

Figure 5.4 Calculated shear modulus values for a 6μm thick paraffin wax film as a function of increasing temperature.

At low temperatures the paraffin wax has a high shear storage modulus and a low shear loss modulus and is said to be in a 'glassy state'. The film is said to be resonating synchronously with the TSM resonator. As the temperature is increased, the upper layer of the film begins to lag in its oscillation compared to the TSM/film interface. The structure of the film begins to change and it becomes softer as illustrated by a sharp decline in the shear modulus. At the same time the loss modulus begins to rise as the film approaches the point of resonance. This is observed to be occurring at around 35.5-36°C from Figure 5.4 and calculated to be occurring at a temperature of 36.5-37°C. From the information obtained during the crystal impedance experiment, it is also possible to calculate the decay length of the acoustic wave as it permeates through the paraffin wax during heating, as well as the phase angle of the wave. Both sets of data are shown on the same graph below in Figure 5.5.

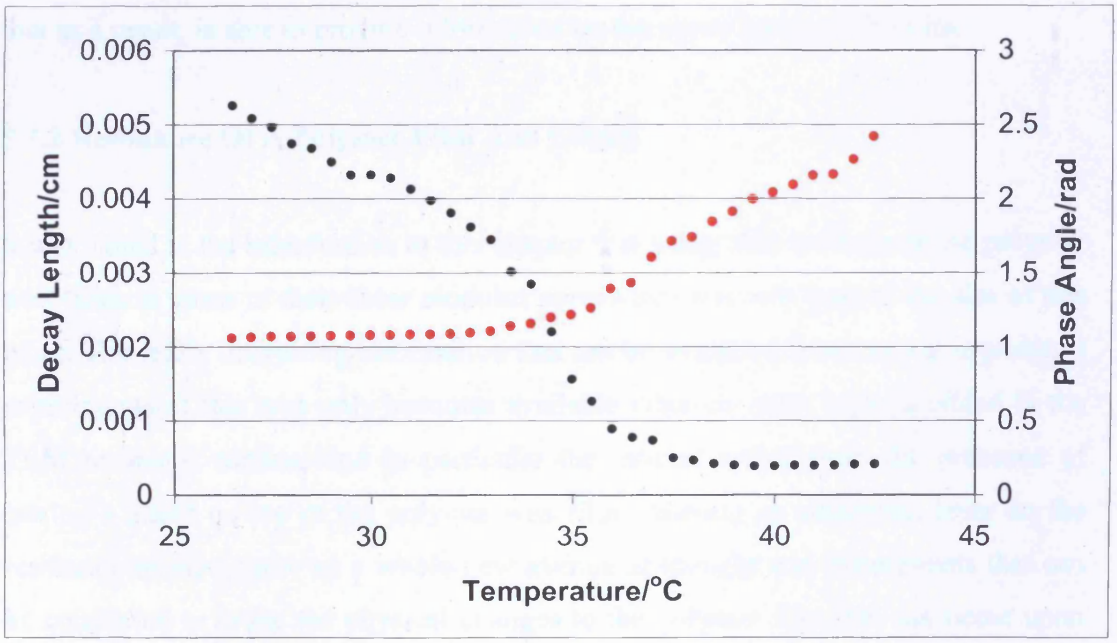

Figure 5.5 Diagram to show the decay length (—, cm) and associated phase angle (—, rad) for the acoustic wave transmitted through a 6μm paraffin wax covered by bulk liquid water.

The decay length for the acoustic wave decreases with increasing temperature up until the point where at temperatures of greater than 40°C, it hardly appears to penetrate the thickness of the 6 μm film. The phase angle of the acoustic wave increases but only after the film has reached the point of resonance. Interestingly at the point on the

graph where we can observe film resonance, we can calculate the phase angle of the film to be approximately $\pi/2$, the condition of resonance being satisfied by an odd multiple of $\pi/2$ as outlined earlier. The decay length (δ) for the paraffin wax film can be calculated using the following formula.

$$\delta = \left(\frac{1}{\omega\sqrt{\rho_f}}\right)\left(\frac{2|G|}{1-\frac{G'}{|G|}}\right) \tag{5.1}$$

At the point when the phase angle indicates that resonance is occurring, the decay length equates to a value of 0.00074 cm. This is a value that is equivalent in magnitude to that of the thickness of the paraffin wax film. It can be concluded that the acoustic wave is able to penetrate through the surface of the paraffin wax film and that as a result, is able to provide information on the upper layers of the film.

5.3.2 Resonance Of A Polymer Film And Liquid

It was stated in the introduction to this chapter that being able to characterise polymer wax films in terms of their shear modulus parameters was only part of the aim of this work. The really interesting information that can be extracted from crystal impedance experiments of this type only becomes available when an extra layer is added to the TSM resonator surface, and in particular the interest stems from the presence of having a liquid on top of the polymer wax film. Having an additional layer on the resonator surface opens up a whole new avenue of thought and experiments that can be conducted to probe the physical changes to the polymer film that can occur upon manipulation of a variable such as frequency or in this case temperature.

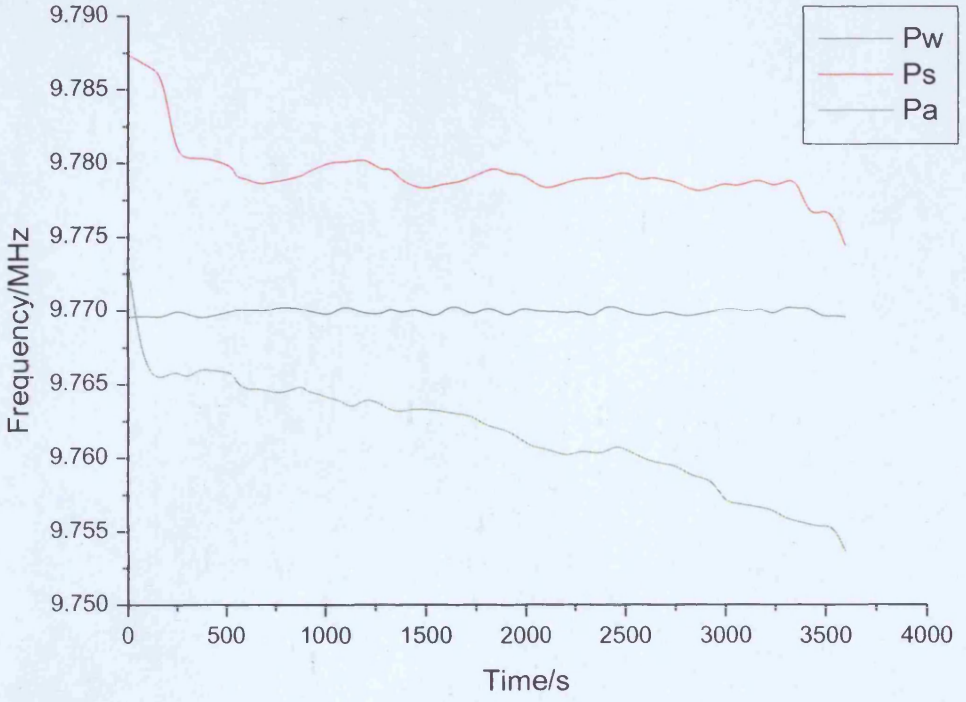

Figure 5.6 Plot to show the change in frequency over time of a Paraffin wax film held at 25°C; data is for a 6μm Paraffin wax film with added water (Pw), solvesso (Ps) and agnique (Pa).

Agnique and solvesso, two surfactants that were primarily used in the next chapter concerning the effect of surfactant on plant wax constituents, were used to explore the extent to which they affect the properties of the polymer wax film. Agnique is an alcohol ethoxylated surfactant that is used to combat mosquitoes. Once sprayed onto the surface of standing water habitats it interrupts the critical air/water interface in the mosquito's larval and pupal development cycle causing them to drown. Solvesso is a heavy aromatic fluid that plays many roles in agricultural formulations. The most widespread use is in emulsifiable concentrate formulations, where the fluid dissolves the active ingredient and acts as a carrier for it and other formulation components, taking them directly to the surface of plants and crops. Water has been used as a useful comparison for the two surfactants in each of the experiments.

The change in resonant frequency as a function of time was determined for paraffin wax films in the presence of each of the three surfactants, with the results plotted on the preceding page. The data shows that both the surfactants have a pronounced effect on the resonant frequency over time while the effect from water

unsurprisingly shows little change. Calculated shear modulus parameters for the paraffin wax films with each of the surfactants are shown below.

In general, multiple layers on the surface of a TSM resonator combine in a linear fashion if all the layers are thin and rigid. It is not possible to add algebraically the contributions from the individual components to get an overall surface mechanical impedance. The simplest and perhaps the most commonly used example of a non-linear system is that of a viscoelastic layer with a Newtonian fluid on top of it. Owing to the phase shift across the viscoelastic layer, the total impedance is not equal to the sum of the characteristic impedances of the individual layers. This is representative of a non-rigid, surface-bound film exposed to a solution such as the paraffin wax films exposed to the various surfactants.

From Table 2.1, it can be seen that the surface mechanical impedance, Z_m, for this particular scenario is represented by:

$$Z_s = Z_s^{film}\left[\frac{Z_s^{fluid}\cosh(\gamma h_f) + Z_s^{film}\sinh(\gamma h_f)}{Z_s^{film}\cosh(\gamma h_f) + Z_s^{fluid}\sinh(\gamma h_f)}\right] \tag{5.2}$$

The surface mechanical impedance given by equation 5.2 can be used to represent viscoelastic films with homogenous moduli or density. This is especially useful when dealing with a polymer film into which a solvent slowly diffuses over a period of time. The outer portion of the film is more plastic than polymer and so behaves differently to layers of the polymer closer to the surface of the resonator, hence it can be modelled as a bilayer of solvated and unsolvated materials.

The surface mechanical impedance is dependent upon the modulus, G, density, ρ_f, and thickness, h_f, of the viscoelastic film; and the density, ρ_l, and viscosity, η_l, of the Newtonian liquid. Being able to substitute in the known parameters for the paraffin wax film (ρ_f, h_f), the Newtonian liquid (ρ_l, η_l) as well as the calculated value of Z_m, allows the shear modulus for the paraffin wax film to be determined with a significant degree of accuracy.

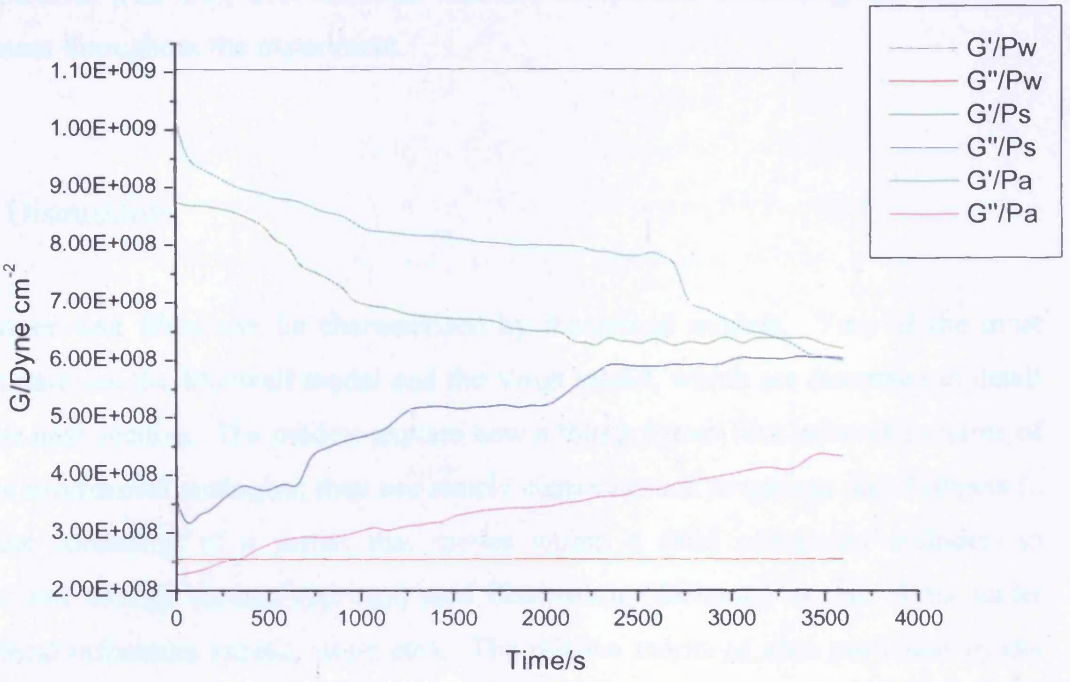

Figure 5.7 Calculated shear modulus values for 6μm paraffin wax films with the addition of the various surfactants as a function of time. Water appears to have little effect over time while the films treated with surfactant show considerable softening.

With the case of the paraffin wax film and surfactant loaded onto a TSM resonator, the ideal mass layer accounts for any trapped material within the surface roughness features of the quartz crystal (entrapped material moves synchronously with the resonator surface and so can be treated as an ideal mass layer), the Newtonian liquid represents the surfactant and the paraffin wax is represented by the viscoelastic layer. This has been shown pictorially in the Theory chapter and the reader is referred back to section 2.3 for reference. Upon leaving the surfactant on the surface of the wax film over a period of time of up to one hour, the resonator moves to lower frequency and the peak admittance decreases. This is consistent with the presence of a film in which there is substantial energy loss *i.e.* a viscoelastic film.

Figure 5.7 shows the calculated G values obtained as a function of time for this system of wax/surfactant. The extracted moduli are much as expected, starting as values which are characteristic of a glassy polymer with $G' >> G''$ (and $G'' = \omega\eta$) and approaching a rubbery or elastic polymer ($G' \sim G''$) with prolonged exposure to the surfactant. It should be noted that water does not appear to have any effect at all on

the paraffin wax film, with the shear modulus components remaining approximately constant throughout the experiment.

5.4 Discussion

Polymer wax films can be characterised by theoretical models. Two of the most important are the Maxwell model and the Voigt model, which are discussed in detail in the next section. The models explain how a thin polymer film behaves in terms of basic mechanical analogies; they use simple elements such as springs and dashpots (a device consisting of a piston that moves within a fluid containing cylinder) to represent energy storage (springs) and dissipation (dashpots) within films under physical influences (stress, strain etc). The relative merits of each particular model are discussed, along with their applicability to the results produced from the experiments within this chapter.

5.4.1 Film Shear Modulus Responses

Crystal impedance spectra have been analysed to investigate polymer viscoelastic properties as functions of excitation frequency and temperature. The frequency dependence of shear modulus is modelled by suggesting a constitutive relationship *i.e.* a relationship between stress and strain for a material. When a stress is applied to a polymer, it results in a combination of elastic deformation (a reversible energy storage) and dissipation (an irreversible energy loss). Purely elastic deformation results in a constitutive relationship that is obeyed by Hooke's Law:

$$T = \mu S \tag{5.3}$$

Where μ is the stiffness of the material. This relationship is commonly represented diagrammatically and theoretically by a spring. Purely viscous dissipation arises in a Newtonian fluid, as described by the relationship:

$$T = \eta \frac{\delta S}{\delta t} \tag{5.4}$$

with η denoting the viscosity. This behaviour is represented by a dashpot, a plunger in a fluid. Polymers however, are complicated materials as they consist of regions of both types of element as just discussed, *i.e.* they are described as being viscoelastic.

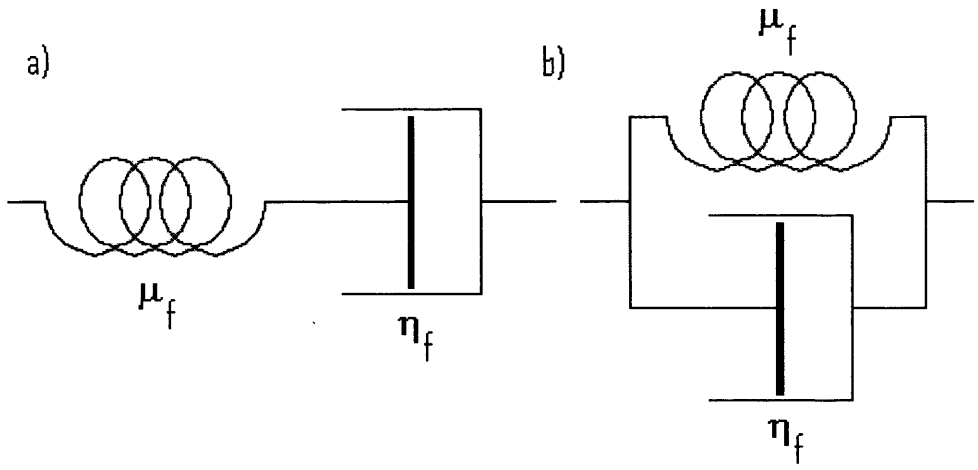

Diagram 5.8 Two-element models leading to relationships for polymer viscoelasticity; a) the Maxwell model and b) the Voigt model.

In general, the behaviour of a viscoelastic polymer can be approximated using several combinations of springs and dashpots. The way in which they are connected gives rise to a unique frequency dependence that can be tested experimentally. In the simplest possible case that accounts for both the energy storage and dissipation, there are two possibilities: an element of each of the types of behaviour arranged in series or in parallel (as seen in Figure 5.8 above).

The Maxwell model consists of a spring and a dashpot arranged in series. This implies equal strains across the two elements although the stresses are additive and gives rise to the following relationship:

$$G = \frac{T}{S} = \left(\frac{1}{\mu_f} + \frac{1}{j\omega\eta_f} \right)^{-1} \tag{5.5}$$

This can also be expressed in the form

$$G = \mu_f \left(\frac{(\omega\tau)^2}{1+(\omega\tau)^2} + j\frac{\omega\tau}{1+(\omega\tau)^2} \right) \tag{5.6}$$

where $\tau = \eta_f/\mu_f$ is a characteristic relaxation time.

The Voigt model consists of a spring and a dashpot arranged in parallel. This implies equal strains across the two elements although the stresses are additive. This gives rise to the following relationship:

$$G = \frac{T}{S} = \mu_f + j\omega\eta_f \tag{5.7}$$

This can also be expressed with a little manipulation in the form:

$$G = \mu_f(1 + j\omega\tau) \tag{5.8}$$

For each model, G' and G'' are identified with their respective real and imaginary parts of expressions 5.6 and 5.8.

5.4.2 Frequency Dependence Of Shear Modulus

The Voigt model predicts a very simple frequency dependence. The storage modulus is independent of frequency ($G' = \mu_f$) while the loss modulus is proportional to the frequency ($G'' = \omega\eta_f$). The Maxwell model is a little bit more complicated in terms of frequency dependence. G' increases monotonically with frequency, saturating at μ_f, while G'' goes through a maximum at $\omega\tau = 1$. The low frequency ($\omega\tau << 1$) limiting characteristics are quadratic and linear respectively for G' and G''. It should be pointed out that τ is a temperature dependent variable ($\tau = \tau_0 \exp[\Delta H/RT]$ and is therefore an activated process) *i.e.* it runs in the opposite direction to temperature. An increase in temperature corresponds to a low value of τ and a decrease in temperature corresponds to a high τ.

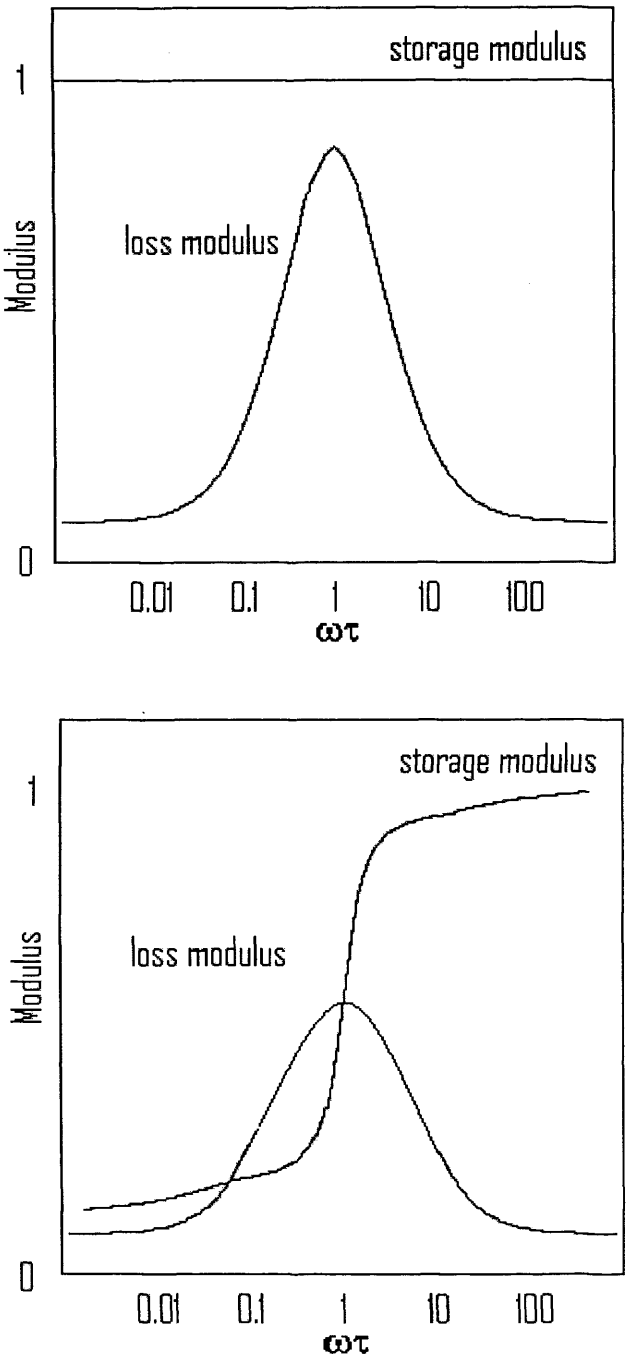

Figure 5.9 Diagrammatical representations of the Voigt (top) and Maxwell (bottom) models.

The Maxwell model at first sight is a better model for the behaviour characteristics of a polymer. When a polymer is deformed slowly (compared to the time for segmental motion), the applied stress is taken up by inter-chain movements, *i.e.* chains are able to move freely past one another. This results in viscous dissipation predominating. When the polymer is deformed rapidly, the chains do not have time to move past one another and instead the strain is taken up by deformation of the individual polymer

chains. This results in elastic storage predominating. The Maxwell model illustrates both of these extremes. At low frequencies (when $\omega\tau << 1$) viscous dissipation predominates, while at high frequencies (when $\omega\tau >> 1$) elastic storage predominates. The frequency dependence of the Maxwell model illustrates a *glass-to-rubber transition*. A low $\omega\tau$ gives rise to a low storage modulus that corresponds to a rubbery polymer. Similarly, a high $\omega\tau$ results in a high storage modulus and corresponds to a glassy polymer. Between these extremes, the elastic and viscous components match so that G'' is a maximum.

Figure 5.10 below, is a graph to show the experimentally determined shear modulus parameters for paraffin wax films with each of the surfactants as a function of temperature. The individual components of the shear modulus have been calculated and shown individually on the diagram.

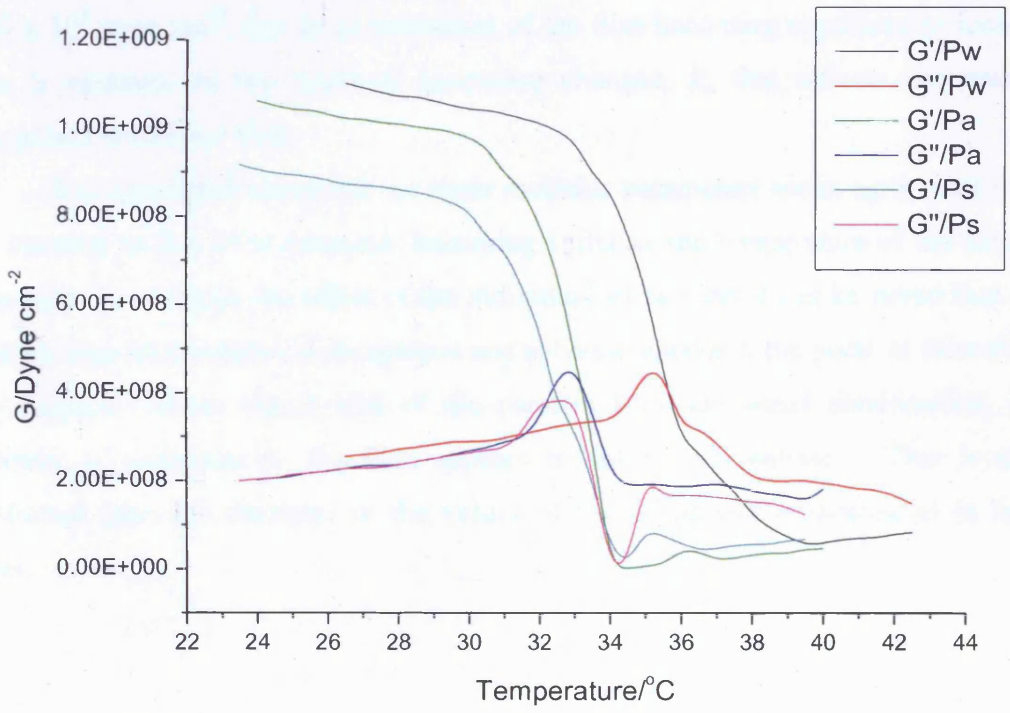

Figure 5.10 Plot to show the experimentally determined shear modulus values for 6μm paraffin wax films and each of the surfactants: water (Pw), agnique (Pa) and solvesso (Ps).

What is immediately observable from the diagram is the classic Maxwell shape to the shear moduli response as a function of temperature (high temperature values correspond to a low value of $\omega\tau$ and vice versa). The starting values of G' for each of

the different surfactants used is in the range 9.18 x 10^8-1.10 x 10^9 dyne cm^{-2}, which reflect those of a glassy polymer. A polymer film in its glassy state has a high shear storage modulus, G' , and low shear loss modulus, G''. G'' has a starting value of around 2.00 x 10^8 dyne cm^{-2} for each of the surfactants used. In this case the film resonates synchronously with the TSM resonator and the TSM acts in its gravimetric regime, that is, as a microbalance. As the polymer film swells due to thermal expansion/an increase in free volume as a result of a rise in temperature, the viscoelastic properties begin to influence its behaviour and the upper film surface lags in its oscillation when compared to the TSM/film interface. At this point the general trend is for G' to decrease sharply and level off to a value of 6.60 x 10^7 dyne cm^{-2}. The dramatic decrease in G' indicates that the material has become softer. The value of G'' on the other hand doubles to around 4.00 x 10^8 dyne cm^{-2} for each case as the films approach the point of relaxation and then tails off to somewhere in the region of 1.40 x 10^8 dyne cm^{-2}, this is an indication of the film becoming significantly lossier. This is mirrored in the motional resistance changes, R, that reflects the energy dissipation within the film.

The calculated values for the shear modulus parameters are in agreement with the material on the TSM resonator becoming softer as the temperature of the film is increased. Looking at the effect of the individual surfactants it can be noted that the paraffin wax films treated with agnique and solvesso approach the point of relaxation two degrees Celsius before that of the paraffin film and water combination, the addition of surfactant to the film appears to soften the material. This is also confirmed from the decrease in the values of the G' parameter calculated in both cases.

5.5 Conclusions

The final response of a modified quartz crystal can be greatly affected by the way in which the film is deposited onto the surface of the electrode. In this work, a polymer wax film was deposited onto a quartz crystal and the resulting impedance/frequency plots analysed. The aim of the work was to characterise the films in terms of their viscoelastic properties.

The viscoelastic properties of the wax films were determined by using the crystal impedance technique. From a qualitative viewpoint, by simply looking at the spectra it is possible to determine the departure from rigidity of the film. Quantitative information can be obtained by 'fitting' the data to an electrical equivalent circuit in order to extract the impedance parameters, ωL and R, where ωL represents the inertial mass changes (energy storage) and R represents the viscoelastic changes (energy loss). It should be noted that it is very difficult to separate out the resistive and inductive components of the impedance due to the film and bathing solution.

The characterisation of polymer films by their storage (G') and loss (G'') moduli is an ideal method for comparison of data. A modelling procedure has been set up to fully characterise the electrical properties of modified quartz crystals in terms of their physical parameters. There are many such models described in this work (section 2.3) varying from the simple case of an ideal mass layer on the surface of a quartz crystal, to the more complicated case of a three layer system consisting of an ideal mass layer + a finite viscoelastic layer + a semi-infinite Newtonian fluid. This particular three-component model is an excellent method to characterise films on the surface of a TSM resonator as it can account for all perturbations on the QCM.

It is clear that with such a complicated model, employing multiple variables, that there could be many possible solutions. Obtaining a unique solution for the shear modulus parameters, G' and G'', of the polymer wax film is therefore of high importance. This can be achieved by breaking the model down into simple, more manageable components and characterising these individually. Although this creates a series of calculations that need to be solved to determine the viscoelastic response of polymers under investigation, the accuracy of the results obtained far outweighs the effort employed in completing the calculations.

The information that can be obtained from a unique and reliable set of values for the individual components of the shear modulus allows a greater understanding of the way in which polymeric like materials (such as long hydrocarbon chain paraffin waxes) behave under the influence of applied stress. In the next chapter, the effect of manipulating the viscosity of polymer waxes is explored with the application of a range of surfactants upon several typical plant wax constituents. The methods and interpretation of the information obtained in this chapter are used to explain structural

changes within the films occurring from the incorporation of surfactant within the upper layers of the materials.

5.6 References

1) C.Barbero, E.J.Calvo, R.Etchenique, G.M.Morales and M.Otero, *Electrochimica Acta*, **45**, (2000), 3895.
2) J.Hossenlopp, R.Jiang, R.Cernosek and F.Josse, *Journal of Polymer Science: Polymer Physics*, **42**, (2004), 2373.

Chapter 6
Manipulation Of Wax Film Viscoelasticity

6.1 Introduction

Having already characterised typical paraffin wax samples in the previous chapter it was decided to probe the various functionalities of components that comprise a typical plant wax, and to ascertain the effects that surfactants have on plant wax components from shear modulus values. It is known that the quantity and composition of plant waxes vary considerably in complexity[1] due to a combination of genetic and environmental factors. They range from simple substances comprising of only a couple of components to highly complex ones made up from a variety of heavily functionalised molecules. As a result plant waxes will often have a distinct appearance and texture. The hydrophobicity of plant waxes makes them good solvents for organic pollutants and impedes the uptake of aqueous sprays without the addition of surfactants.

Research into plant waxes and plant wax constituents has been heavily weighted towards the identification of individual components of the plant waxes using a variety of methods. It is not surprising that physical[2], spectroscopic[3-4] and imaging techniques[5] have been employed to gain an overview into the chemical composition of leaf surfaces. The mechanisms involved in the transfer of solutes across cuticle membranes and the effect of surfactants and other adjuvants on the rates of uptake of organic compounds have also been studied[6] but the effect on physical characteristics has been less extensively studied. No attempt to date has been made to provide an insight into the change in structural properties associated with solute or solvent penetration into the surface of a leaf, so the novelty of this subject is of great interest.

The results presented in this section are from a series of experiments designed to investigate the effect of surfactants on plant wax components and interpret the results in terms of shear modulus parameters. A variety of typical plant wax components (notably long chain acids, alcohols and esters) was chosen from the many types of compounds found on the surfaces of leaves including amongst others alkenes, ketones, fatty acids and lipids. The individual components used were behenic acid, docosanol and octadecyl docosanoate, though will be referred to as B, D and O

respectively throughout this Chapter. Paraffin wax (P) was also used for comparison purposes.

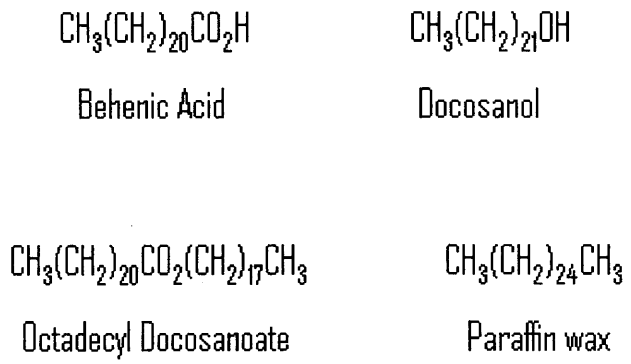

Figure 6.1 A diagram to show the structural differences between the various types of plant wax constituents used in this study; acid, alcohol, ester and alkane functionality are represented by behenic acid (B), docosanol (D), octadecyl docosanoate (O) and paraffin wax (P) respectively.

The surfactants used were water (w), agnique (a) and solvesso (s). Surfactants aid absorption (by manipulating hydrophobicity/hydrophilicity) causing a more uniform spreading of the spray solution across the plant leaf; they help spray droplets stick to the surface of the plant resulting in less run off and also prevent crystallization of the active ingredient on the leaf's surface. Further information on the wax components and surfactants used in this study, including physical properties, can be found in section 3.3.2.3 of the Experimental Chapter.

6.2 Experimental

The uncoated TSM resonator was fully characterised before each experiment using crystal impedance measurements of the blank crystal exposed to air. Polymer wax films and plant wax components were then deposited onto 10 MHz quartz crystals in the manner described in the Experimental Chapter, section 3.3.2.2. Solutions were then added drop-wise to the surface of the crystal until the piezoelectrically active area of the wax component/wax film under investigation was completely covered with both film and surfactant in the vertical axis. Crystal impedance measurements were

then recorded at the fundamental harmonic over a suitable temperature range in order to obtain shear modulus parameters for the various resonator coatings.

6.3 Results

The aim of this chapter is the manipulation of polymer wax films, and in particular those polymer wax films that are typically found on the surfaces of plant leaves. The ideas used in exploring and characterising the resonance effects of viscoelastic polymer films from the previous chapter, are used to the same extent with the different surface coatings employed as typical plant wax constituents in this chapter. The following section explores the spectra and subsequent shear modulus values obtained for the plant wax films in the presence of several surfactants. An attempt is made to characterise the findings in terms of the functionality of the material on the TSM resonator and also the calculated energy of activation for the diffusion of the surfactants into the polymer films.

6.3.1 Effect Of Surfactant On Paraffin wax

Figure 6.2 below shows the experimentally determined shear modulus parameters for paraffin waxes in the presence of surfactants from the previous results chapter. The individual components of the shear modulus (shear modulus and loss modulus, G' and G'' respectively) have been calculated and shown individually on the diagram. The values obtained for the shear modulus parameters show that the material on the TSM resonator becomes softer as the temperature of the film is increased. Looking at the effect of the individual surfactants it can be noted that the paraffin wax films treated with agnique and solvesso resonate at a point 2^{o} C before that of the paraffin wax film and water combination, the addition of surfactant to the surface of the film appears to soften the material. This is also confirmed from the decrease in the values of the G' parameter calculated in both cases. As an explanation of the calculated shear modulus parameters has already been given in the preceding chapter, it is perhaps more important to focus on the differences in the shear modulus parameters attributed to the

surfactants rather than to the polymer material itself. A discussion concerning the effect of the surfactant on the shear modulus values follows herein.

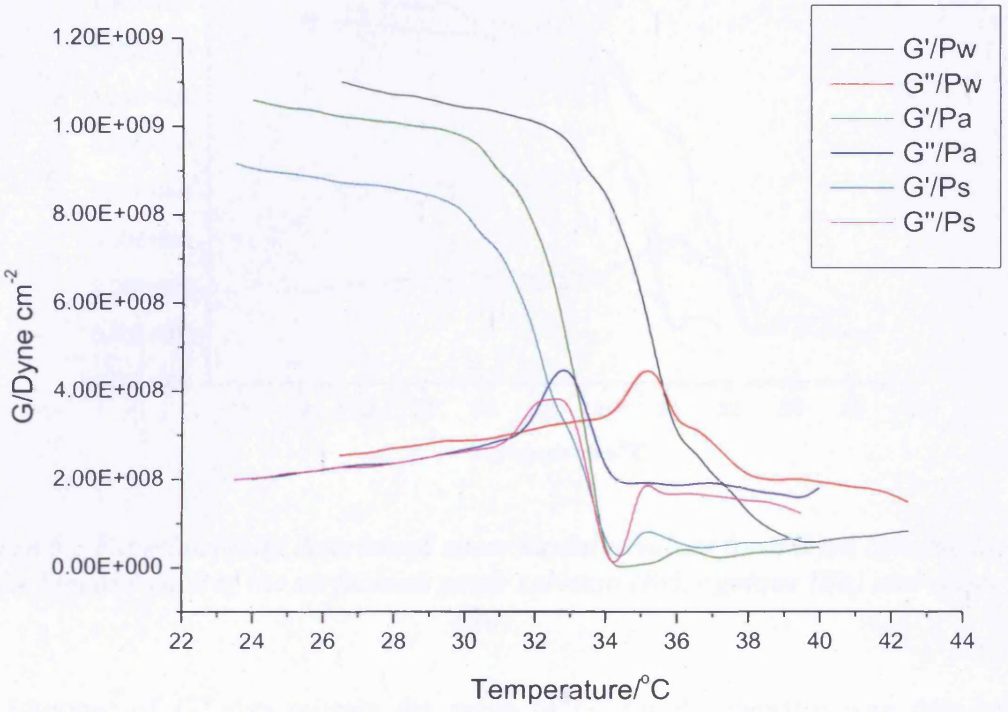

Figure 6.2 Experimentally determined shear modulus values for a 6 μm paraffin wax film sample and each of the surfactants used: water (Pw), agnique (Pa) and solvesso (Ps).

6.3.2 Plant Wax Constituent Data

The relevant graphs summarising the shear modulus parameters for the other types of wax component and various surfactants used in this study, are shown below for comparison. At first glance it is easy to see that all the experimentally determined shear moduli data for wax component/surfactant do appear to follow the same pattern as the paraffin wax/surfactant combinations. That is to say that upon moving from lower temperatures to higher ones, the general trend is for G' to decrease sharply; the dramatic decrease in G' reflecting the fact that the material has become softer and more viscoelastic.

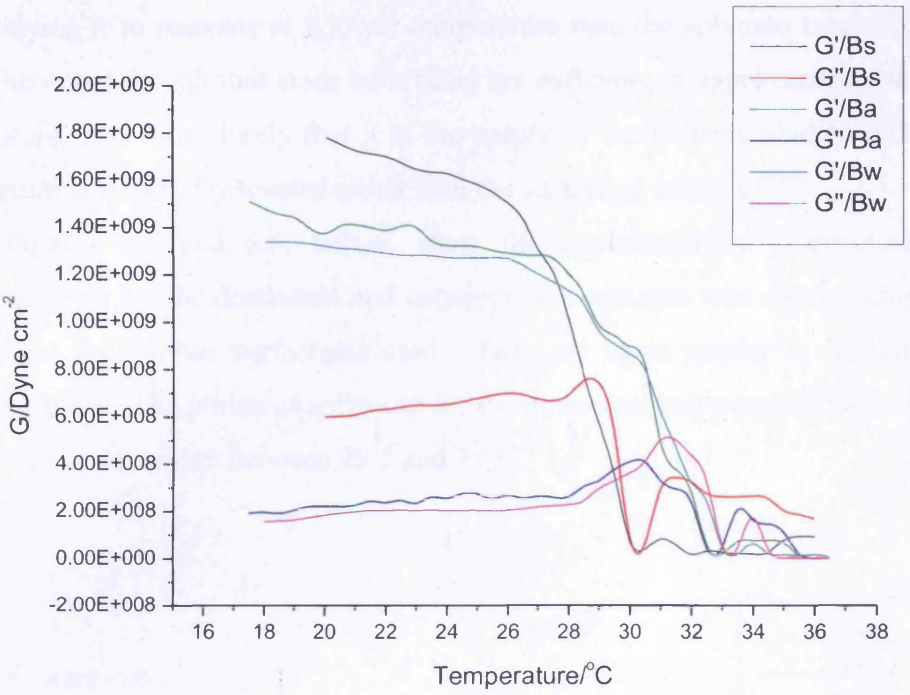

Figure 6.3 Experimentally determined shear modulus values for a 6 μm behenic acid wax film and each of the surfactants used: solvesso (Bs), agnique (Ba) and water (Bw).

The response of G'' also mirrors the value of G'' for the paraffin wax data with increasing temperature; it reflects the changes in motional resistance within the film as energy is dissipated from it. Figure 6.3 on the previous page shows the calculated shear modulus parameters for the behenic acid wax component in the presence of the various surfactants used. The point of softening for each wax/surfactant combination occurs around 3° C lower than for the corresponding relaxation peak seen in the paraffin wax film experiments. A cursory look at the literature melting temperatures for paraffin wax and behenic acid reveal that behenic acid melts at a significantly higher temperature than paraffin wax. This is an interesting fact to note, as the effect of adding surfactant to a behenic acid film appears to soften it more than that of the paraffin wax film (see Table 6.1 for supporting data). This is due to the fact that the effect of adding surfactant softens the behenic acid film by becoming incorporated into the polymer film itself. There also appears to be very little difference between the shear modulus values as a result of using a surfactant as compared to water. The behenic acid wax treated with agnique relaxes at a temperature lower than the corresponding behenic acid and solvesso combination (approximately 1° C lower).

The anionic nature of the agnique could aid the surfactant to soften the behenic acid film enabling it to resonate at a lower temperature than the solvesso treated film. It should be noted though that since both films are softening at approximately the same temperature, it is more likely that it is the nature of the behenic acid to dictate the temperature at which it resonates rather than the surfactant added to it.

Figures 6.4 and 6.5, below, show the experimentally determined shear modulus values for the docosanol and octadecyl docosanoate wax components in the presence of the various surfactants used. They are again similar in format to the preceding plots. The points of softening for the docosanol and octadecyl docosanoate films occur in the region between 29.5 and 31°C.

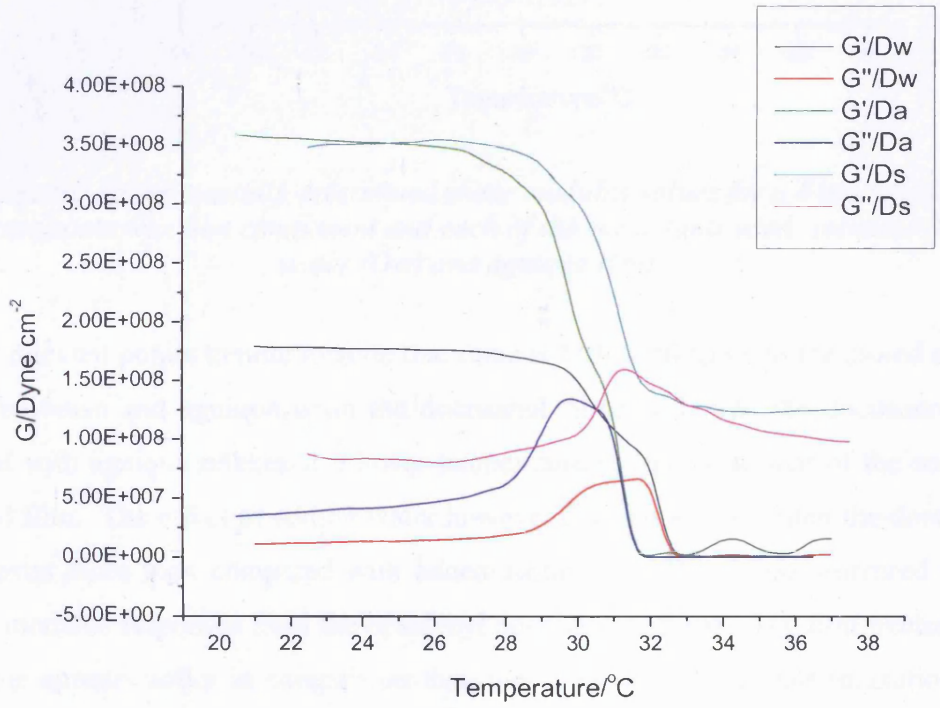

Figure 6.4 Experimentally determined shear modulus values for a 6 μm docosanol wax film component and each of the surfactants used: water (Dw), agnique (Da) and solvesso (Ds).

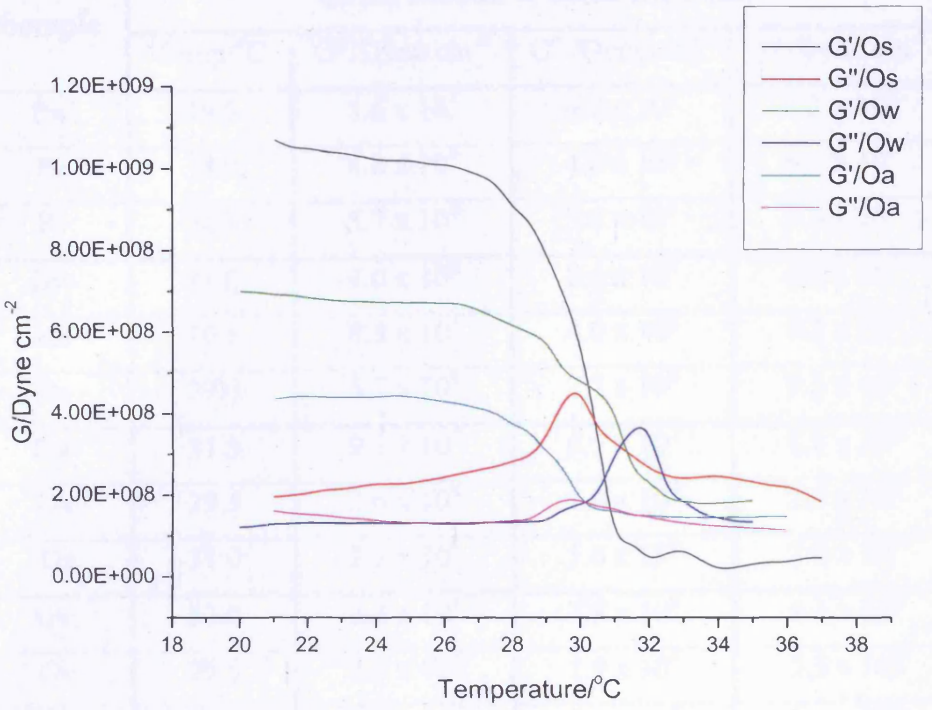

Figure 6.5 Experimentally determined shear modulus values for a 6 μm octadecyl docosanoate wax film component and each of the surfactants used: solvesso (Os), water (Ow) and agnique (Oa).

Other relevant points to note include that there is little difference in the stored energy from solvesso and agnique upon the docosanol films, although the docosanol film treated with agnique relaxes at a lower temperature compared to that of the solvesso treated film. The effect of adding water however does appear to soften the docosanol film even more than compared with added surfactant. This is not mirrored in the shear modulus responses from the octadecyl docosanoate films. The film treated with agnique appears softer in comparison than the other two. It reaches relaxation first and also appears to be lossier than the other two films from the outset. The effect of water on the octadecyl docosanoate film shows neither a pronounced effect on the loss/storage modulus in terms of an increase or a decrease in the values obtained.

The following table is a summary of the relevant data for each experiment of plant wax constituent and chemical surfactant used. Selected values are shown for the temperature at which the resonance peak occurs, and the corresponding experimentally determined shear modulus parameters at the resonance peak for each individual combination of wax component and surfactant.

Sample	Shear Moduli at Softening Point			
	Temp/°C	G' /Dyne cm^{-2}	G'' /Dyne cm^{-2}	|G|/Dyne cm^{-2}
Pw	35.5	5.4×10^8	4.7×10^8	7.2×10^8
Pa	33.0	4.8×10^8	4.6×10^8	6.7×10^8
Ps	32.5	3.7×10^8	3.8×10^8	5.3×10^8
Bw	31.0	4.0×10^8	2.6×10^8	4.8×10^8
Ba	30.5	8.3×10^8	4.0×10^8	9.2×10^8
Bs	29.0	5.7×10^8	7.7×10^8	9.5×10^8
Dw	31.5	9.3×10^7	6.5×10^7	1.1×10^8
Da	29.5	2.6×10^8	1.4×10^8	2.9×10^8
Ds	31.0	2.3×10^8	1.6×10^8	2.8×10^8
Ow	32.0	2.4×10^8	3.8×10^8	4.4×10^8
Oa	29.5	2.7×10^8	1.9×10^8	3.3×10^8
Os	31.0	7.9×10^7	3.3×10^8	3.4×10^8

Table 6.1 Table to show the relevant experimentally determined shear modulus parameters at the resonance peak for each combination of wax film component and surfactant used.

The data in the table has been recorded so the effect on the individual plant wax constituents can be determined. Experimentally determined shear modulus values shown are an average of five separate experiments carried out using wax film sections from the same parent block of material. The values shown for the storage and loss moduli are quoted in dyne cm^{-2} and consistently fall within $\pm 10^6$ dyne cm^{-2} of the average. They are also in good agreement with each other for the majority of the samples examined, *i.e.* $G' = G''$. This is what would be predicted from a simple model of the structure of a polymer upon softening.

The other side to this discussion is what effect the surfactant has on the shear modulus values obtained. In order to be able to do this, Table 6.1 is rewritten below to take into account the effect that the surfactants have on the experimentally determined shear modulus parameters. The values of the storage, loss and shear modulus are now grouped together to give an indication of this effect. One thing is clear from the tabulated data and that is that the effect of the surfactant on the different film constituents appears to soften the films and shifts the point of relaxation in the films to approximately the same temperature.

Sample	Shear Moduli at Softening Point			
	Temp/°C	G' /Dyne cm^{-2}	G'' /Dyne cm^{-2}	|G|/Dyne cm^{-2}
Pa	33.0	4.8×10^8	4.6×10^8	6.7×10^8
Ba	30.5	8.3×10^8	4.0×10^8	9.12×10^8
Da	29.5	2.6×10^8	1.4×10^8	2.9×10^8
Oa	29.5	2.7×10^8	1.9×10^8	3.3×10^8
Ps	32.5	3.7×10^8	3.8×10^8	5.3×10^8
Bs	29.0	5.7×10^8	7.7×10^8	9.5×10^8
Ds	31.0	2.3×10^8	1.6×10^8	2.8×10^8
Os	31.0	7.9×10^7	3.3×10^8	3.4×10^8
Pw	35.5	5.4×10^8	4.7×10^8	7.2×10^8
Bw	31.0	4.0×10^8	2.6×10^8	4.8×10^8
Dw	31.5	9.3×10^7	6.5×10^7	1.2×10^8
Ow	32.0	2.4×10^8	3.8×10^8	4.4×10^8

Table 6.2 A revised version of Table 6.1 to show the effect of the surfactant on the plant wax constituent data.

It could be suggested that looking at the data from Table 6.1 that the stiffness of the materials on the TSM resonator surface is in the order:

docosanol < octadecyl docosanoate < paraffin wax < behenic acid

And that is to say that from the experimentally determined |G| values, either the behenic acid or paraffin wax samples are in general tougher, more rigid materials than the other two constituents, or that the effect of surfactant on the docosanol or octadecyl docosanoate films has a more pronounced effect than as seen with the behenic acid or paraffin wax films. Another point that could be made in terms of how much effect the surfactants have on the films is that they appear to be in the order:

water < solvesso < agnique

The experimentally determined shear modulus values from the effect of added surfactant on the films shows a small but discernable difference. The films treated with surfactant have a noticeably higher |G| than compared to a film with just water

added to the surface. It should be remembered that the values of |G| quoted are only shown for the calculated point of resonance in the films. A similar pattern can however be seen for each set of data as a whole but it is the value of the loss and storage moduli at the point of relaxation which are of interest. Overall it can be said that this is not a reliable way to conduct speculation on the properties and change in structural nature of the polymer wax films. It cannot be concluded from a single point of data how soft, strong or viscous these materials are on their own, or indeed any changes induced from the effect of added surfactant.

6.4 Discussion

In order to put the results into some sort of perspective in terms of the effect that a particular surfactant may have on a given type of plant wax material, it is a good idea to determine a specific measurable property. This can be done by calculating a parameter common to all the plant wax constituent/surfactant examples and comparing the results. An elegant way to do this is to calculate the energy of activation for the diffusion of the surfactant into the upper layers (and beyond) of the polymer films. This parameter will identify the ease at which the various surfactants are able to diffuse into the surfaces of the films, and also provide a legitimate standard in order to compare data from different films to each other.

6.4.1 Activation Energy Of Diffusion

When plotting the data to represent the shear modulus components for each experiment, it is easy to treat the data to determine the energy of activation for the process of the surfactant diffusing into the polymer wax film.

We know that the relaxation time, τ, is temperature dependent, it is an activated process and runs in the opposite direction to temperature, T, *i.e.* we can write $\tau = f(T)$. We can also assume that the shear and loss modulus are a function of temperature (G' and $G'' = f(T)$) and therefore write;

$$\tau = \frac{1}{k} = \tau_0 \exp\left[\frac{\Delta E}{RT}\right] \qquad (6.1)$$

As a result we can determine ΔE for the process of surfactant diffusing into the upper layers of polymer film. A simple Arrhenius plot of the natural log of the characteristic relaxation time for the polymers (τ) against a reciprocal temperature scale (in Kelvins, K), is required to extract the activation energy of diffusion. From the experimentally determined values of G' and G'', the value of τ (and hence the activation energy of diffusion) can be calculated using the models explained in Chapter 5 (sections 5.4.1 and 5.4.2). With a little manipulation, the relaxation time for any polymer can therefore be extracted for use in Equation 6.1. Figure 6.6 is an example of how the activation energy of diffusion is calculated for the paraffin wax film in the presence of water.

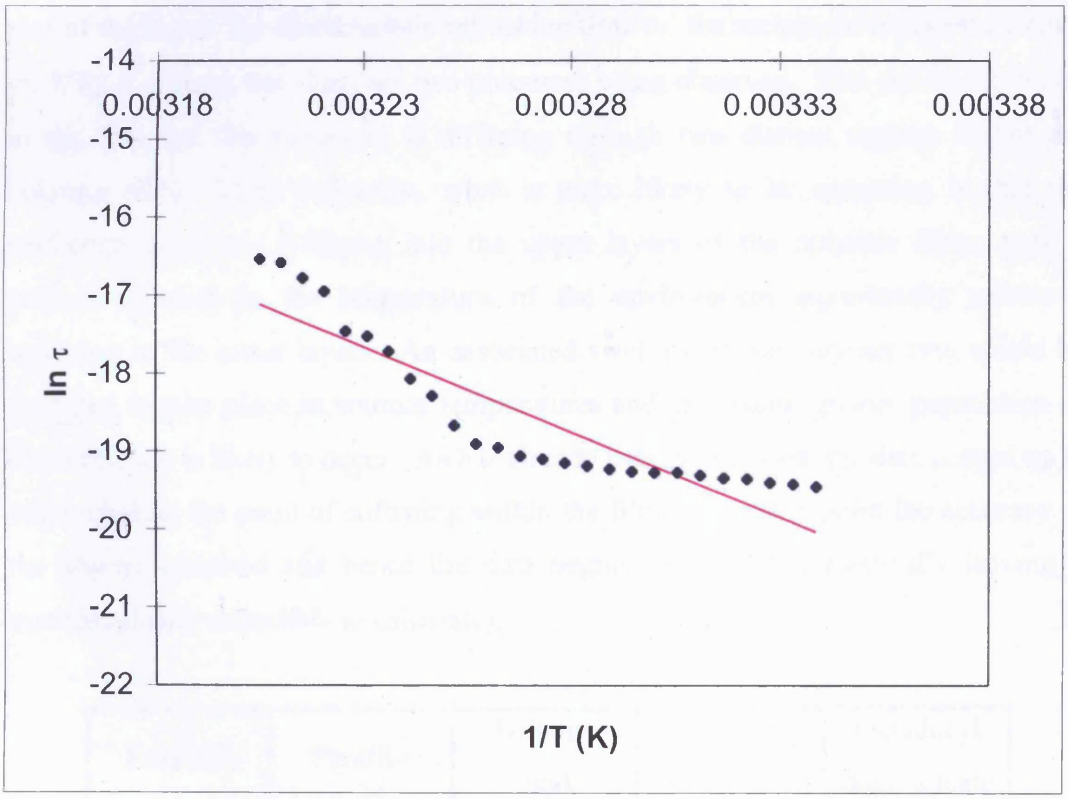

Figure 6.6 An Arrhenius plot to calculate the energy of activation for a paraffin wax film in the presence of water.

The slope of the line is determined mathematically from equation 6.1 above, using the data up to and including the point of softening within the films (after this point the accuracy of the spectra obtained and hence the data begins to tail off dramatically leaving it mathematically unfeasible to calculate). This gives a calculated activation energy for the paraffin wax in the presence of water to be 180 kJ mol^{-1}. A similar sort

of experiment was conducted to investigate the diffusion properties of organic solutes across the waxy layers that guard the membranes of plants. Baur *et al*[7] examined the mechanistic aspects of temperature effects on cuticles and cuticular waxes. They measured the mobilities of various organic solutes across the cuticular membranes of a range of species in order to calculate the activation energy of diffusion for the process. The temperature range over which the data was recorded was between 15 °C and 78°C. No distinct phase transitions were observed in the cuticular membrane, although rearrangement of some of the wax constituents was evident at higher temperatures. They found that depending on the species, the activation energies of diffusion for the different solutes ranged from between 75 and 189 kJ mol^{-1}. Getting back to Figure 6.6, it can be seen that instead of having a single straight line from the plot of the log of the characteristic relaxation time *vs.* the reciprocal temperature (In τ *vs.* 1/T), it appears that there are two processes being observed. This can be attributed to the fact that the surfactant is diffusing through two distinct regions within the polymer film. Upon reflection, what is more likely to be occurring is that the surfactant is slowly diffusing into the upper layers of the polymer films, until a gradual increase in the temperature of the environment significantly allows a softening of the lower layers. An associated swelling of the polymer film would be expected to take place in warmer temperatures and as a result greater penetration of the surfactant is likely to occur. As has already been mentioned, the data is used up to and including the point of softening within the films (after this point the accuracy of the spectra obtained and hence the data begins to tail off dramatically leaving it mathematically unfeasible to calculate).

Example	Paraffin	Behenic acid	Docosanol	Octadecyl docosanoate
Agnique	2331	675	403	318
Solvesso	3239	1017	370	766
Water	378	373	360	370

Table 6.3 Table to summarise the energy of activation (ΔE) for the diffusion of surfactant into the upper layers of polymer film for each of the combinations of wax component and surfactant used, values quoted are in kJ mol^{-1}.

In a similar manner, the energy of activation for diffusion of surfactant into the surface film was calculated for each of the remaining wax component/surfactant combinations. Activation energy diffusion data was calculated for each separate process within the films and is presented in Tables 6.3 and 6.4.

Example	Paraffin	Behenic acid	Docosanol	Octadecyl docosanoate
Agnique	108	41	63	16
Solvesso	93	62	24	58
Water	75	42	51	24

Table 6.4 Table to summarise the energy of activation (ΔE) for the diffusion of surfactant into the lower layers of polymer film for each of the combinations of wax component and surfactant used, values quoted are in kJ mol^{-1}.

The activation energies calculated are in an approximate range between 300 and 3300 kJ mol^{-1} for the upper layers and 20 and 100 kJ mol^{-1} for the lower layers. Values of the calculated activation energies for the lower layers of the polymer films are quoted ± 2 kJ mol^{-1}. The values for the upper layers of the polymer films are quoted ± 5 kJ mol^{-1} for octadecyl docosanoate and docosanol, and ± 10 kJ mol^{-1} for paraffin wax and behenic acid respectively.

From Tables 6.3 and 6.4, the same conclusion regarding the effect of the surfactant can be reached. The order of:

$$\text{water} < \text{solvesso} < \text{agnique}$$

is exactly the same as found for the shear modulus. Parallels can also be drawn with regards to the data on the individual plant wax constituents in terms of their shear modulus values and activation energies. The order from the tables of average activation energies,

$$\text{octadecyl docosanoate} \sim \text{docosanol} < \text{behenic acid} < \text{paraffin wax}$$

also reflects that of the shear modulus data. It can be concluded that the surfactants do appear to find it easier to diffuse into materials such as docosanol and octadecyl

docosanoate whereas behenic acid and paraffin wax may in general be tougher, less viscous materials for surfactants to diffuse into.

This could either be due to i) the mobility of smaller molecules penetrating the upper surface layers of the plant wax components, or ii) the temperature variation of *G*. Although the latter will be related to the former, they are not necessarily the same thing. In this case it seems unlikely that size matters, as water is rather a small molecule in comparison with the bulky surfactants being used. A more reasonable explanation would be that the structural differences between surfactant and plant wax component are playing a leading role. The comparatively high value for the diffusion of agnique into a paraffin wax film is just such an example. The value of the activation energy may seem a little high in comparison with the rest of the data but it should not be too surprising. The idea of a polar liquid trying to diffuse through the surface of a very non-polar waxy coating should indeed generate such a high value for its activation energy. These conclusions can be drawn from the supporting evidence in Tables 6.1 and 6.2.

6.5 Conclusions

This chapter has shown how materials, typical of those found as constituents in plant waxes, behave in the presence of surfactants when deposited onto a quartz crystal. The aim of the work was to characterise the films in terms of their shear modulus parameters and corresponding values for the energies of activation for the diffusion of surfactants into the upper layers of the different plant wax constituents.

The viscoelastic properties of the wax films were determined by using the crystal impedance technique. Plots of the calculated shear modulus parameters were gathered and interpreted in two ways, firstly the effect on the plant wax constituent and secondly the effect of the surfactant on the shear modulus was determined. The plots of calculated shear modulus parameters against increasing temperature were in good agreement with the theoretical models of polymer viscoelasticity already described in the previous chapter. However, it was shown that it proved very difficult to quantify the effects in terms of structural changes as the plant wax constituents approached the point of softening. Values for the activation energy of diffusion were

calculated from the shear modulus data using a simple relationship. This enabled a quantifiable standard to be set up in order to compare and contrast the data.

An evaluation of all the results obtained indicates that the surfactants appear to follow the same trend with regards to the effect on the shear modulus parameters and activation energies when changing from one plant wax constituent to another. Both chemical surfactants used appear to have a noticeable but significant effect compared to the experiments when water is used as the surfactant. This is of no great surprise. Although the plant wax constituents used were chosen because of the differing functional groups that they bear, it should be remembered that they are all still long chain hydrocarbon molecules. All of the constituents used have typically more than 20 carbon atoms present in their composition that, regardless of the functional groups which they possess, means that they are predominantly non-polar and as a result will find it very difficult for water to have a significant chance of becoming incorporated into the upper layers of the polymer structure.

It is clear that calculating the energy of activation for the diffusion of surfactant into the polymer films is a useful method to extract information in order to clarify the data already produced from the calculated shear modulus parameters. The values for the energy of activation were shown to be of similar magnitude to those from a similar study concentrating on the rate of adsorption of solutes penetrating the waxy cuticles of leaves. Although the information obtained is in good agreement, it would be a useful idea to explore the effect of varying the concentration to obtain the critical micelle concentration (C_{mc}) of the surfactants. This may produce interesting data as far as working out which components of pesticides play a dominant role in crop protection.

Another useful comparison to make would be to see the effect of surfactants on actual plant wax materials. It had been thought that this would make an ideal comparison to make as original plant waxes had been supplied for the purpose of this study. Unfortunately it proved very difficult to produce samples for investigation due to the crystalline nature of the waxes.

6.6 References

1) D. Post-Beittenmiller, *Annu.Rev.Plant Physiol.Plant Mol.Biol.*, **47**, (1996), 405.
2) A.J.Matas, J.M.Sanz and A.Heredia, *International Journal of Biological Macromolecules*, **33**, (2003), 31.
3) R.D.Belding, S.M.Blankenship, E.Young and R.B.Leidy, *Journal of the American Society for Horticultural Science*, **123**, (1998), 348.
4) K.Quenea, S.Derenne, C.Largeau, C.Rumpel and A.Mariotti, *Organic Geochemistry*, **36**, (2005), 349.
5) K.Koch, C.Neinhuis, H-J.Ensikat and W.Barthlott, *Journal of Experimental Botany*, **55**, (2004), 711.
6) M.Riederer and L.Schreiber, *Waxes: Chemistry, Molecular Biology and Functions*, The Oily Press, Dundee, (1995), 131-156.
7) P.Baur, H.Marzouk and L.Schonherr, *Planta.*, **199:404**, (1996), 412.

Chapter 7
General Conclusions And Scope For Future Work

7.1 General Conclusions

The general conclusions from the chapters presented in this thesis will now be discussed with the key points summarised.

7.1.1 Amperometric Sensor Conclusions

The design and modification of a chiral amperometric sensor for the detection of Group 1 metal ions and small carboxylic acids has been demonstrated. Cyclic voltammetry has shown qualitatively the response to the addition of substrate to quaternary ammonium binaphthyl salts, the variations in response of limiting current being attributed to several factors (structural architecture of the receptor, size and polarity of the analyte etc) as outlined in the relevant chapter. It has been postulated that the ability to reduce the binaphthyl salts is directly related to the conformation of the radical intermediate and the strain imparted upon it by the quaternary ammonium group. Molecular modelling has helped to identify regions of the quaternary ammonium binaphthyl salts most likely to play a part in the 'recognition' of substrates, with NMR spectroscopic data identifying significant binding interactions between host and substrate.

Electrochemical investigations have shown that the current for the oxidation of the receptor decreases with increasing concentration for a variety of small carboxylic acids. The relative decrease in current is dependent upon the shape and size of the analyte and the stereoconformation of the receptor's binding site. The architecture of the binaphthyl salts was been modified to produce several stereochemical isomers. The effect of manipulating the configuration of the chiral centres within the salts has shown that the overall geometry of the quaternary ammonium group and attached pendant groups changes dramatically upon electrooxidation. Extending the size of the pendant groups confirmed the idea that bulky side chains were prohibiting the substrate from binding to the ammonium salts. In addition, the presence of a polar

functional group on the analyte has a significant effect on the sensitivity of the receptor, which was attributed to hydrogen bond interactions.

7.1.2 Gravimetric Sensor Conclusions

The final response of a modified quartz crystal was shown to be greatly affected by the way in which the film is deposited onto the surface of the electrode. In this work, a polymer wax film was deposited onto a quartz crystal and the resulting impedance/frequency plots analysed. The aim of this work was to characterise the films in terms of their viscoelastic properties.

The viscoelastic properties of the polymer wax films were determined by using the crystal impedance technique. From a qualitative point of view, by simply looking at the spectra it is possible to observe the departure from rigidity of the film. Quantitative information can be obtained by 'fitting' the data to an electrical equivalent circuit in order to extract the impedance parameters, ωL and R, where ωL represents the inertial mass changes (energy storage) and R represents the viscoelastic changes (energy loss).

The experimental results obtained allowed the determination of the shear modulus for the paraffin wax film at a variety of different temperatures and in a variety of environments. This allowed the film to be characterised in terms of structural changes associated with heating and cooling. The characterisation of polymer wax films was extended further by using several plant wax components for analysis. The films were adhered to the surface of quartz crystals and the samples were heated and cooled in the presence of surfactants/adjuvants commonly used in crop protection. From the calculated shear modulus values, the energy of activation for the diffusion of surfactant into the surface of the 'plant leaves' was calculated. The order of penetration of the surfactants was deduced from the data, with the differing rates of diffusion ascribed to the functionality of the plant wax components and surfactants/adjuvants.

In general it was shown that the more polar surfactants diffused at a quicker rate than the less polar surfactants. The plant wax constituents also appeared to play a role in the way that the surfactants diffused into the films. Combinations of polar and

non-polar surfactants/films lessened the effect of the diffusing surfactant while similar combinations increased the rate of diffusion.

7.2 Future Work

The scope for future work from the chapters presented in this thesis will now be discussed with the main ideas addressed.

7.2.1 Amperometric Sensors

The quantitative determination of lithium ions in any area of chemistry would be beneficial simply due to the large number of roles in Chemistry that it plays a part in. In particular the detection of ions in very small concentrations allows chemical and physiological processes to be studied with greater understanding. The obvious choice for further research in this area is not only the detection of ions, but also the simultaneous determination of the actual concentration of ions present. It should not be difficult to produce tables (or a scale) relating to the limiting current produced for the detection and determination of several ions at varying concentrations. The increases in sensor research should allow the eventual detection of ions to sub ppb levels with a high degree of accuracy.

7.2.2 Gravimetric Sensors

We have seen in this work that a suitable method for the determination of shear modulus parameters, with regards to the changes in a polymers structure from applied stresses and strains has been developed. Of obvious interest to the reader would be the continuation of some of the ideas presented in Chapter 6. Exploring different types of plant wax component along with the many possible surfactants and adjuvants that make up modern day fertilisers and pesticides would be a fascinating avenue of research. The types of wax that could be explored are limited merely to the ability to derive enough of a suitable quantity of wax for the preparation of films for investigation. Another avenue of interest would be to determine the rates of diffusion

for a surfactant in a variety of climates. By controlling physical conditions to produce differing environments, it would be possible to produce diffusion/penetration data for a particular wax film (or crop species) in any climatic region.

Appendix A: Symbols used within this thesis

A	area of electrode
C_0	static capacitance
C_1	capacitance
C_p	parasitic capacitance
Δ_f	change in frequency
E	applied potential
E_p^{ox}	oxidized potential
E_p^{red}	reduced potential
ε_{22}	dielectric permittivity
F	Faraday constant
f_0	fundamental resonant frequency
f_p	parallel resonant frequency
f_s	series resonant frequency
G	shear modulus
G'	loss modulus
G''	storage modulus
G_f	film shear modulus
h_q	thickness of quartz
η_q	quartz effective viscosity
$Im(Z_s)$	imaginary surface mechanical impedance
i_p	peak current
j	$\sqrt{-1}$
K^2	quartz electromechanical coupling coefficient
L_1	inductance
L_2	motional inductance
λ_q	wavelength of quartz
M_q	mass of quartz
μ_q	quartz shear stiffness
N	harmonic number
n	number of electrons
π	pi
ρ_f	film density
ρ_q	density of quartz
ρ_s	areal mass density
R	gas constant
R_1	resistance
R_2	motional resistance
$Re(Z_s)$	real surface mechanical impedance
T	stress
T	temperature
t	time
T_{XY}	sinusoidally steady-state shear stress
υ_x	surface shear particle velocity in x-direction
V_q	wavespeed of quartz
ω_s	angular frequency
Y	admittance
Z_e	electrical impedance

Z_m	motional impedance
Z_m^0	motional impedance unperturbed resonator
Z_q	characteristic shear wave impedance of quartz
Z_s	surface mechanical impedance